LASER REFLECTANCE MODULATION IN SILICON INTEGRATED CIRCUITS

TEO KIAN JIN JASON

A THESIS SUBMITTED

FOR THE DEGREE OF
DOCTOR OF PHILOSOPHY

DEPARTMENT OF ELECTRICAL AND COMPUTER ENGINEERING

NATIONAL UNIVERSITY OF SINGAPORE

2011

ACKNOWLEDGEMENTS

There are many people who have helped or supported me during my graduate years, and I am deeply grateful for these gestures. There is a list of people that I wish to explicitly express my appreciation as follows:

- Prof Jacob Phang, my academic supervisor and role model, for his guidance. In all our interactions, he has been very meticulous and inquisitive, maintaining a very high standard which occasionally caused anguish, but often resulted in new breakthroughs. He has kept me honest and thorough during my academic journey.

- Mr Chua Choon Meng, CEO of SEMICAPS, for being a great industrial mentor through my graduate years. He has provided invaluable insights into the needs of the FA industry with lengthy technical discussions that often stretched into the nights.

- The staff of SEMICAPS for supporting my research efforts with world-class equipment and facilities. Special thanks go to Lian Ser, Wah Peng, Soon Huat, Wei Kok, Nelson, Carlson, Rane, Daniel, Michelle, Lina, Edwards and Jennifer.

- Mrs Ho Chiow Mooi, the principal laboratory officer and the staff of the Centre for Integrated Circuit Failure Analysis (CICFAR) for providing excellent administration and logistics support throughout my PhD candidature.

- My fellow peers at CICFAR who have provided samples, encouragement and moral support. These include Soon Leng, Alfred, Szu Huat, Heng Wah, Dmitry and Cong Tinh.

- My grandmother, parents and sister for their ceaseless support.

- And most of all to my wife, Maria for her support in my whole graduate program and providing me with the greatest joy of my life by giving birth to Sarah.

TABLE OF CONTENTS

ABSTRACT

This research aims to understand the physics governing laser reflectance modulation and to develop novel backside characterization techniques based on these parameters. The reflected laser intensity modulations due to changes in the absorption coefficient and refractive index as a result of variation in the temperature, electric field and free-carrier density have been reported. These results are used in the modeling of the laser beam propagation.

Backside and frontside reflectance modulations at different applied electrical bias were compared. Investigations were also carried out on backside-prepared resistive structures at different applied electrical bias, dimensions and substrate thicknesses. The backside reflectance intensities are observed to modulate negatively with temperature increase. A backside reflectance model is developed and is found to agree well with the experimental data. Subsequently, reflectance modulation experiments were carried out on backside prepared NMOS and PMOS transistors from the 0.18 µm process technology node with substrate thickness of 350 µm. The MOS channel at different modes of operation is successfully characterized for variations in gate bias, channel lengths and MOS device types.

The results further the understanding of laser reflectance modulation of silicon integrated circuits, and present a novel application of a sensitive, non-invasive

thermal probe, as well as a novel technique to characterize the functionality of an MOS device.

LIST OF ABBREVIATIONS

AC	Alternating Current
AM	Amplitude Modulation
BGA	Ball Grid Array
BJT	Bipolar Junction Transistor
CCD	Charge Coupled Device
CMOS	Complementary Metal-Oxide-Semiconductor
CW	Continuous Wave
DC	Direct Current
DPE	Data Processing Engines
DRAM	Dynamic Random Access Memory
DReM	Differential Resistance Measurement
DUT	Device Under Test
FA	Failure Analysis
FFT	Fast Fourier Transform
FR	Faraday Rotator
FWHM	Full Width Half Maximum
IC	Integrated Circuits
InGaAs	Indium Gallium Arsenide
InSb	Indium Antimonide
IR	Infrared
ITRS	International Technology Roadmap for Semiconductors
LED	Light Emitting Diode
LIVA	Light Induced Voltage Alteration
LTP	Laser Timing Probe
LVP	Laser Voltage Probing
MOSFET	Metal-Oxide-Semiconductor Field Effect Transistor
MPU	Microprocessor Unit
NA	Numerical Aperture
NIR	Near Infrared
NMOS	N-channel Metal-Oxide-Semiconductor

OBIC	Optical Beam Induced Current
OBIRCH	Optical Beam Induced Resistance Change
PBS	Polarizing Beam Splitter
PDP	Polarization Difference Probing
PEM	Photon Emission Microscopy
PICA	Picosecond Imaging Circuit Analysis
PM	Phase Modulation
PMOS	P-channel Metal-Oxide-Semiconductor
PPM	Parts Per Million
RSIL	Refractive Solid Immersion Lens
SCOBIC	Single Contact Optical Beam Induced Current
SEM	Scanning Electron Microscope
Si	Silicon
SIL	Solid Immersion Lens
SNR	Signal-to-Noise Ratio
SOI	Silicon-on-Insulator
SOM	Scanning Optical Microscopy
TBIP	Thermal Beam Induced Phenomena
TIVA	Thermally Induced Voltage Alteration
TRE	Time-Resolved Emission
VLSI	Very Large Scale Integration
VR	Variable Retarder
VSR	Velocity Saturation Region

LIST OF SYMBOLS

α	Absorption coefficient
α_{fc}	Absorption coefficient for free-carrier absorption
α_{p}	Absorption coefficient for phonon-assisted absorption
N_A	Acceptor charge density
ω_p	Angular phonon frequency
ω	Angular photon frequency
k	Boltzmann constant
$\Delta\alpha_{Si}$	Change in absorption coefficient of silicon
ΔN_e	Change in free electron density
ΔN_h	Change in free hole density
Δn_{Si}	Change in refractive index of silicon
L	Channel length
W	Channel width
A	Constant which depends on density-of-states, effective mass and temperature
B	Constant which depends on the free carrier effective mass and mobility
ΔL	Depletion layer width
ΔL_{Ko}	Depletion layer width for pseudo-two-dimensional model by Ko
ΔL_{saj}	Depletion layer width for single-sided single abrupt junction
ΔL_{taj}	Depletion layer width for two-sided single abrupt junction
N_D	Donor charge density
V_{DS}	Drain voltage
I_{DS}	Drain current
m_e^*	Effective mass of electrons
m_h^*	Effective mass of holes
L_{eff}	Electrical channel length

q	Electronic charge
f_L	Focal length
N	Free carrier density
V_{GS}	Gate voltage
γ	High temperature absorption coefficient
N_{doped}	Impurity doping concentration
I_0	Incident laser intensity
E_g	Indirect bandgap energy
I_4	Intensity of light incident at the Material-Air interface
I_2	Intensity of light incident at the Material-Al interface
I_3	Intensity of light reflected at the Material-Al interface
I_1	Intensity of light transmitted at the Air-Material interface
I_5	Intensity of light transmitted at the Material-Air interface
x_j	Junction depth
L_{mask}	Mask channel length
E_m	Maximum electric field
$E_{m,saj}$	Maximum electric field calculated using single abrupt junction model
R	Minimum resolvable spatial resolution
N_m	Mobile charge density
λ	Optical wavelength
t_{ox}	Oxide thickness
V_l	Output of lock-in amplifier for experimental setup
V_a	Output of low noise amplifier for experimental setup
I_0	Peak irradiance of the laser in $MW.cm^{-2}$
ε_0	Permittivity of free space
ε_{ox}	Permittivity of silicon oxide
ε_{Si}	Permittivity of silicon

ΔL_{peak}	Position of dominant peak from the drain-end in the channel
D	Pupil diameter of the objective lens
$\hbar$	Reduced Planck constant
V_{ref}	Reference frequency input of lock-in amplifier
R	Reflectance
r	Reflectance coefficient
R_1	Reflectance of the Air-Material interface
n	Refractive index of crystalline silicon
n_i	Refractive index of incident medium
n_t	Refractive index of transmitting medium
T_0	Room temperature
E_S	Saturated electric field
I_{DSAT}	Saturation drain current
V_{DSAT}	Saturation drain voltage
T	Temperature
k	Thermoreflectance coefficient
t_m	Thickness of material
t_s	Thickness of silicon substrate
V_T	Threshold voltage
I_t	Total reflected light intensity measured by the photon detector
I_b	Total reflected light intensity measured by the photon detector for the backside reflectance model
I_f	Total reflected light intensity measured by the photon detector for the frontside reflectance model
T_r	Transmittance
T_1	Transmittance of the Air-Material interface
β_{2P}	Two-photon absorption coupling coefficient

LIST OF TABLES

LIST OF FIGURES

Chapter 1: Introduction

This introduction provides an overview of the failure analysis (FA) that is typically used for microelectronic devices. Distinction is made between frontside and backside FA. This is followed by a discussion on the International Technology Roadmap for Semiconductors (ITRS) reference for 2009 to highlight the major challenges. Brief introductions are provided for existing FA techniques in fault localization, timing and temperature measurements to illustrate the inadequacies of these techniques in addressing the challenges highlighted by the ITRS roadmap. The chapter concludes with the main motivations for undertaking this research.

1.1 Failure Analysis

Failure analysis (FA) is an integral step for the development and manufacturing of semiconductor integrated circuits. It occurs at all stages of the manufacturing process from design and wafer fabrication to integrated circuits (IC) packaging and applications. Failure analysis tools are critical to the key functions of design, product and process development, wafer production, packaging, testing and customer returns. The microelectronic failure analysis is a sequential process that consists of five main steps, namely, failure validation, fault localization, sample preparation and defect tracing, defect characterization and root cause determination [1]. It involves a thorough understanding of the failing mechanisms and determination of its root cause.

1.2 Fault Localization Techniques

Fault localization is a challenge in FA [2] and is the most critical step as it sharply reduces the area for subsequent analyses [3]. The main fault localization techniques are based on two categories of far-field techniques, namely passive and active techniques. The main passive technique is Photon Emission Microscopy (PEM) [4, 5] which is based on electroluminescence and detection is achieved with a photon-sensitive camera. The main active technique is based on scanning optical microscopy (SOM) [6] in which a near-infrared (NIR) laser at 1.064 or 1.34 µm wavelength is used to stimulate failures that are sensitive to carrier or thermal stimulation respectively. PEM and SOM are typically used as complementary techniques in fault localization.

1.2.1 Photon Emission Microscopy

PEM requires the sample to be biased in normal operating mode, so that failure sites can emit photons and then be localized. Emission of photons result from three main radiative transition processes: (i) Inter-band electron-hole pair recombinations, (ii) Transitions involving chemical impurities, physical defects or deep traps, and (iii) Intra-band transitions involving hot electrons and hot holes [4]. The emitted photons can be observed from frontside or backside prepared samples using photon detectors [7]. Photon emissions from defective sites occur due to leaky junctions, contact spiking, oxide leakages and silicon mechanical damages. Given that it is relatively easy to use PEM for defect localizations, it is widely used in industry. It should be added that photon emissions are also

observed from normal MOSFET in saturation mode. Hence, photon emission sites may not necessarily correlate to fault locations [5]. Besides, not all faults emit photons. For example, metallization failures are ohmic and do not result in radiative recombinations.

1.2.2 Scanning Optical Microscopy

SOM uses a scanned NIR laser beam to stimulate failures which are sensitive to thermal or carrier stimulation. At NIR 1.34 µm wavelength, the incident photons induced localized heating as the photon energies are lower than the device bandgap energy. The temperature variation causes a change in resistivity and induces power alteration which can be detected by various detection techniques. These include Optical Beam Induced Resistance Change (OBIRCH) [6, 8], Thermally Induced Voltage Alteration (TIVA) [6, 9], Thermal Beam Induced Phenomena (TBIP) [10], and Differential Resistance Measurement (DReM) [11]. At 1064 nm wavelength, the incident photons generate electron-hole pairs through carrier stimulation. Techniques using this phenomenon include Optical Beam Induced Current (OBIC) [12], Single Contact Optical Beam Induced Current (SCOBIC) [13] and Light Induced Voltage Alteration (LIVA) [14].

1.3 Frontside and Backside Failure Analyses

In the late nineties, the frontside failure analysis became increasingly difficult due to an increasing number of multi-level metals which prevent emitted photons at the faults from reaching the detector and laser stimulation from reaching the

faulty areas. Figure 1.1 illustrates this difficulty with Scanning Electron Microscope (SEM) cross-sectional images of ICs with 2 and 6 metallization layers. Furthermore, the use of array input-output connection pads across the die for higher speed devices such as ball grid array (BGA) and flip-chip packages does not allow frontside access with full electrical functionality. These constraints have led to the development of a new suite of backside failure analysis techniques [15].

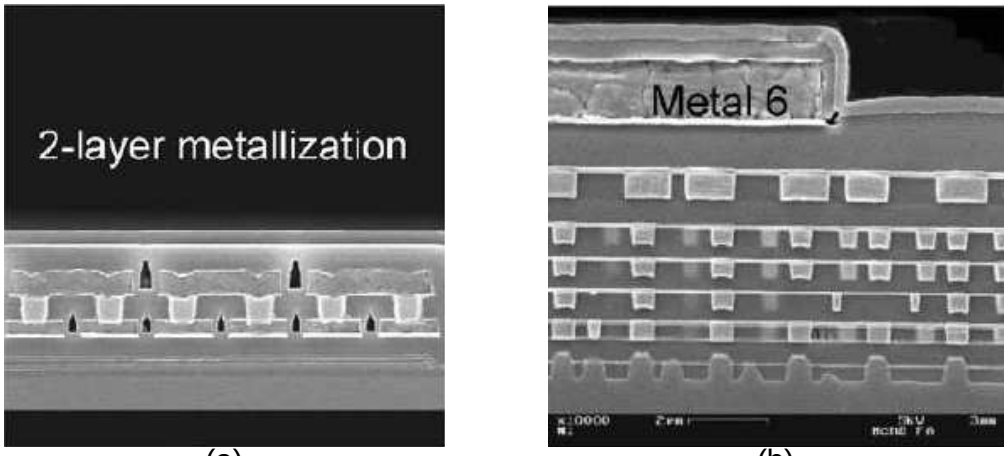

(a) (b)

Fig 1.1. SEM cross sections of an IC with (a) 2 layer metallization and (b) 6 layer metallization [16]

Backside localization techniques overcome these limitations by taking advantage of the fact that backside silicon is fairly transparent to near-infrared (NIR) light as shown in Figure 1.2. The transmittance is the highest around the silicon (Si) bandgap of 1107 nm and decreases significantly with doping concentration and backside thickness [6, 17]. Wavelengths below 1 μm are absorbed by the Si substrate. Device substrates are generally thinned to about 100 μm for the

highest transmittance without introducing stress induced damage from the backside preparation process.

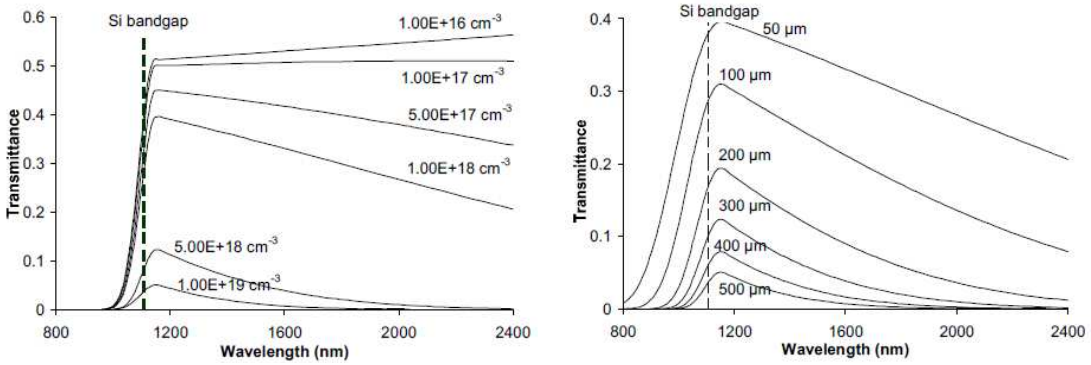

(a) (b)

Fig 1.2 – Light transmittance of (a) 500 µm p-Si with different doping concentrations and (b) p-Si at 10^{19} cm^{-3} with different thicknesses [6, 17]

For backside sample preparation, it is important to consider the doping concentration and backside substrate thickness because they affect the transmittance of light as shown in Figure 1.2. For instance, a highly doped sample at a doping concentration of 10^{19} cm^{-3} and backside thickness of 500 µm has transmittance less than 0.1, resulting in significant signal intensity attenuation. In practical terms, lightly doped substrates do not require much thinning while thinning can improve transmittance significantly for highly doped substrates.

1.4 Failure Analysis Roadmap

The International Technology Roadmap for Semiconductors (ITRS) provides updated roadmap of the needs and challenges facing the semiconductor industry over the next fifteen years so that research and developmental efforts can be

channeled more effectively. In the roadmap for 2009 as seen in Figure 1.3, the ITRS is bullish about the continuation of Moore's Law.

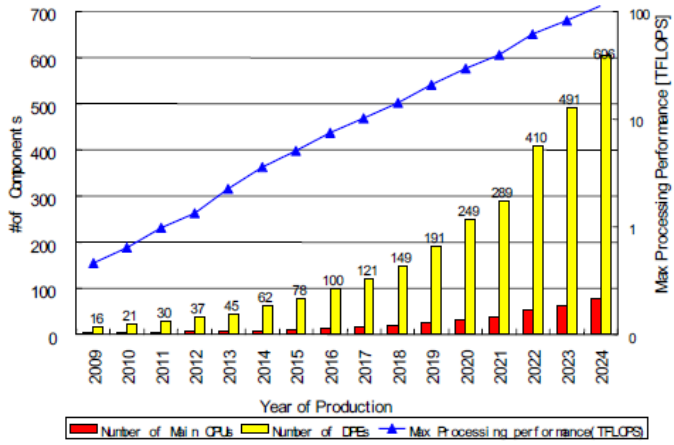

Fig 1.3 – ITRS technology trend based on roadmap for 2009 [18]

With the consolidation of transistors into functional cores in the die, the projected number of components to be packed in the die appears to be more gradual than historical trend. However, the projected exponential growth in the number of Data Processing Engines (DPE) shows the ITRS expects Moore's Law to continue beyond the present 32 nm technology node.

Table 1.1 tabulates some of the key parameters relevant to FA. As device dimension scales, the number of emitted photons and their intensities become significantly weaker. This is partly because voltage bias reduction reduces heat generation in the integrated circuits. Beyond 2010, the critical defect size is predicted to shrink below 22.5 nm.

Table 1.1 – Key parameters relevant to FA extracted from ITRS roadmap [18]

Year of Production	2005	2007	2010	2013
Dimensional Scaling				
DRAM Half Pitch (nm)	80	65	45	32
MPU Metal 1 Half Pitch (nm)	90	68	45	32
Wafer Diameter (mm)	300	300	300	300
Equiv. Gate Oxide Thickness (Physical) (nm) Extended Planar Bulk (High Performance)	1.2	1.1	0.65	NA
Critical Defect Size (nm)	45	34	22.5	16
Complexity				
Total Chip Area for MPU (mm^2)	111	140	140	140
Number of processor cores	2	4	8	16
Total Chip Area for DRAM (mm^2)	88	110	93	93
No of transistors per μm^2 at production (including on-chip SRAM) for MPU[1]	1.74	2.78	5.52	11.04
No of Cells per μm^2 for DRAM[1]	12.2	19.5	46.1	92.4
Number of Metal Levels for MPU	11	11	12	13
MPU Total Interconnect Length (m/cm^2)	1019	1439	2222	3125
Number of Metal Levels for DRAM	4	4	4	4
Electrical Performance				
Power Supply Voltage for MPU (V_{dd}) (V)	0.9 -1.1	0.8 -1.1	0.7-1.0	0.6 -0.9
Allowable Maximum Power for MPU (W)	200	300	300	300
On-chip Clock Frequency (MHz)	5,204	9,285	15,079	22,980
Sub-threshold Leakage ($I_{sd,leak}$) ($\mu A/\mu m$) Extended Planar Bulk (High Performance)	0.06	0.2	0.28	NA

MPU = Microprocessor Unit
DRAM = Dynamic Random Access Memory
[1] Derived from ITRS Data

At 32 nm technology node, the DRAM transistor half pitch and the MPU metal half pitch reduce to 32 nm. The roadmap noted the spatial resolution of far-field optical microscopy is limited by the wavelength of light. It highlighted the need for research in the optical techniques to address this issue. With the use of solid immersion lens, backside laser reflectance techniques can achieve spatial resolution of 250 nm [19].

The incidence of failures increases significantly with each new technology node as a consequence of the introduction of new materials, smaller geometries and faster devices. The new circuit architecture and advanced fabrication processes associated with the new technology nodes result in new failure mechanisms which require new failure analysis techniques for localization [2]. These are major challenges that will require new FA techniques and tools to overcome [20].

1.5 Backside Timing Measurement

For more than half a century, Moore's Law [21] has been followed. Approximately every two years, the number of transistors that can be packed in a unit area of an IC doubles. Transistor scaling enables faster transistor switching and circuit performance at a higher operating frequency. Figure 1.4 illustrates the historical trend of frequency doubling. There are two techniques that can measure timing information, namely Laser Voltage Probing (LVP) and Time-Resolved Emission (TRE).

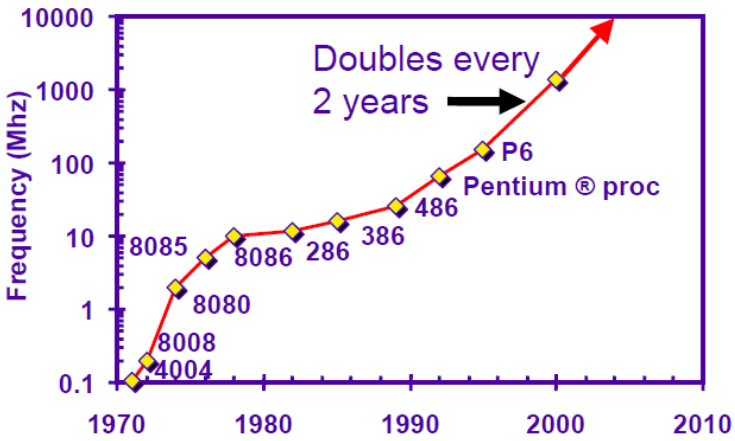

Fig 1.4 Frequency doubling every two years [22]

1.5.1 Laser Voltage Probing

LVP uses the principle that reflected laser of a transistor is modulated by the electro-optical effects associated with its switching to accurately determine the rise time, fall time and switching period of the probed transistor. The first prototypes resulted from research done in Stanford [23] in the 1980s. The first commercial LVP system that used this concept for timing measurements became

available in the 1990s [24]. With laser technology rapidly improving, gigahertz timing measurements were demonstrated by the turn of the 21th century. However, these systems are not able to determine the voltage magnitude of the waveform, although the signals correlated with the real signals. The limited use of laser reflectance-based systems to provide timing information is probably one of the main reasons why the technique did not become prevalent. Using the underlying principle of laser probing to extract timing information, other similar techniques have been known as Laser Timing Probe (LTP) techniques.

1.5.2 Time Resolved Emission

Light emission in CMOS circuits occurs during switching of the gates. As such, the temporal characteristics of the switching information can be used to derive the electrical characteristics of the circuits. TRE detects the switching photons with information that includes rise time, fall time and switching period [25]. This technique has been found to have picosecond resolution [26].

Picosecond Imaging Circuit Analysis (PICA) is the main technique for TRE. It has constantly been compared with LVP as shown in Table. 1.2. The main strength of PICA over LVP is parallel acquisition of data. Unfortunately, very long acquisition time is required due to weak photon emissions [27]. Even with its ability to do parallel acquisition, the total acquisition time required for PICA is significantly longer than LVP.

Table 1.2 – Comparison of laser probing and PICA techniques [28]

	LVP	PICA
Invasiveness	Negligible	None
Voltage linearity	Yes	No
Parallel acquisition	No	Yes
Temporal resolution	< 30 ps	< 30 ps
Acquisition time (10 µs tester loop)	1-2 min	10 hours

Furthermore, as transistor scales, the emitted photon emission intensity is expected to become even weaker, implying that longer integration time is needed. Moving forward, techniques using laser reflectance appear to have better chances of becoming mainstream tools compared to time-resolved photon emission techniques since the signal sensitivity of the latter degrades severely with device scaling.

1.6 Backside Temperature Measurement

If the frequency doubling trend had continued as seen in Figure 1.4, processors would be running at more than 10 GHz. Higher frequency would also result in higher heat dissipation for the IC. This is inevitable since Complementary Metal-Oxide-Semiconductor (CMOS) transistors remain as the workhorse of the semiconductor industry with no suitable replacement yet. CMOS transistors have very low leakage current during steady-state, but expend energy during switching [29]. Figure 1.5 illustrates the power crisis that could result if frequency doubling had continued. Power management becomes an important topic in IC design.

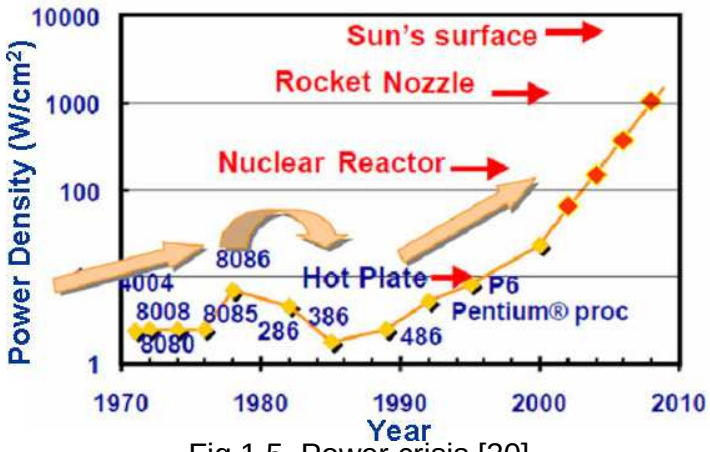

Fig 1.5 Power crisis [30]

In a bid to continue to scale performance without further increasing the frequency, dual-core and subsequently multi-core processors were introduced [31]. Packing more transistors per unit area in the die of an IC also increases the power density if the applied bias remains the same. If Moore's law is to continue, active power management is critical to enable more transistors to be packed in the die.

The task is difficult as there are currently no suitable techniques that can monitor the heat generation and dissipation in the cores at the temperature, timing and spatial resolution needed to make meaningful observations. While mainstream activities of design, manufacturing and test improve rapidly, the development of new FA tools and techniques to improve the analytical capabilities is constantly lagging behind [2].

The FA industry currently relies on InSb cameras for thermal imaging. It can detect wavelength range from 1.5 μm to 5.0 μm, has maximum frame rate of 90 fps and can achieve less than 25 mK resolution at a pixel pitch of 20 μm [32].

Figure 1.6 is a pseudo-transformed backside thermal emission image of a resistive structure at a substrate thickness of 200 µm and biased at 80 mW. The red areas represent maximum emission, and the blue areas represent negligible emission. The InSb camera is among the most sensitive NIR/IR cameras in the market, and is a very useful tool for identification of hot spots. However, it does not have the timing and spatial resolutions needed to monitor heat generation and dissipation in advanced integrated circuits.

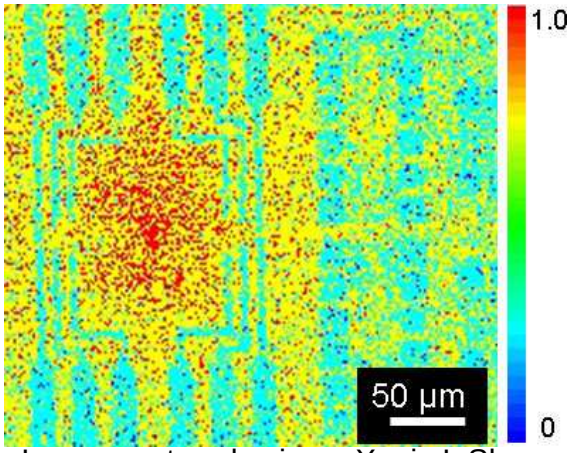

Fig 1.6 – Image captured using a Xenic InSb camera [32]

Thermoreflectance refers to the application of laser reflectance modulation in thermal characterization. It uses the principle that the reflected intensity is modulated by changes in the material reflectivity and absorption due to a temperature change of the IC. Past researches have demonstrated a spatial resolution of 1 µm, and a temporal resolution near 10 ns and a temperature resolution near 25 mK [33-35]. These techniques showed better thermal, spatial and temporal sensitivities for thermal characterization. However, calibrations are required before accurate temperature measurements can be made [34, 35].

Previous work focused on frontside laser probing due to the popularity of frontside FA until the late 1990s. More researches and development efforts are needed for backside thermoreflectance techniques.

1.7 Project Motivation

The objective of this project is to understand the fundamental physics governing laser reflectance techniques, and to develop novel backside characterization techniques using laser reflectance modulations based on these fundamental parameters. Prior works have established that laser reflectance modulates due to electro-optical [23] and temperature effects [34]. These understandings will aid in the theoretical and experimental explorations to achieve the objective.

At present, NIR lasers can achieve a spatial resolution of 250 nm with the use of solid immersion lens. The advent of laser technologies has also enabled laser timing reflectance to precisely track digital circuits running at 8 to 20 gigahertz. As such, laser reflectance is suitable to be developed into a non-contact electrical probe. But additional research needs to be dedicated to understand the fundamental electro-optical effects to derive signal voltage information from the measurements on top of the timing information. Compared to existing probing methods, laser probing is definitely superior in terms of resolution, reliability, repeatability and ease of use. Hence, it has the potential for wide applications in microelectronic device characterization.

Thermal information can also be derived from laser reflectance techniques. By understanding the thermal effects of laser modulation, it is possible to develop a high resolution thermal probe with high sensitivity that enables backside thermal mapping of the integrated circuit and its temperature variations. This will provide a new tool for precise defect isolation by tracking its temperature profile.

Independently, either technique would address some of the challenges facing the FA community. A comprehensive understanding of the interaction between electro-optical and thermal effects of laser modulation would allow the development of a non-contact probe that can characterize both electrical and thermal properties of the device.

This thesis is organized and presented as follows:

Chapter 2 covers a comprehensive review of reflectance physics. The variation of the absorption coefficient and refractive index due to temperature, electric field and free carrier concentration variations are discussed. Reflectance modulations due to MOS device operations are also discussed, and models to determine the length of the pinch-off region are put forth.

Chapter 3 covers a comprehensive review of reflectance systems and techniques. These include CCD-based systems and techniques, interferometric and non-interferometric laser-based systems and techniques, and laser-pulsed techniques.

Chapter 4 presents physical models for frontside and backside reflectance. The key parameters are identified and modeled. Reflectance modulation hypotheses for metal thin films and MOS transistors are described.

Chapter 5 presents the experimental system to carry out the reflectance works. The optical capabilities and limitations of the system are discussed. In addition, the effects of the laser source coherence, incident laser power and sample tilt are described. System configurations for measurements using the static and dynamic techniques are highlighted.

Chapter 6 presents a comparison study of static and dynamic techniques to determine its sensitivity and suitability in the measurements of backside laser reflectance modulation for resistive devices. Backside reflectance modulations at different applied bias, dimensions and substrate thicknesses are determined and compared to analytical data. Frontside laser reflectance modulations are also determined and compared.

Chapter 7 presents a comparison study of static and dynamic techniques to determine its sensitivity and suitability in the characterization of the linear, pinch-off and saturation operating modes of an NMOS transistor. The applied bias and dimensions of NMOS transistors are varied to determine its effects on laser reflectance modulations. NMOS and PMOS transistors of similar dimensions are

also compared. The experimental results are reconciled with the analytical understandings.

Chapter 8 describes the possible applications of the research findings in advancing the field of FA. Four novel applications using laser reflectance modulations are presented, and include localization of biased devices, identification of defective metal lines, non-invasive thermal probe for temperature determination, and non-invasive electro-optical probe for characterizing MOS devices.

Chapter 9 concludes the thesis and summarizes the key contributions of this research project. Several recommendations for future work are proposed.

Chapter 2 Review of Reflectance Physics Theory

Laser reflectance measures the reflected power of an incident laser beam [36]. Along the propagation path of a reflected laser beam, its intensity is attenuated by the medium which it traverses due to absorption. At the interface between two media, reflection and refraction occur. The refractive index of the media and the angle of the laser beam to the normal of the interface affect the intensity of the reflected beam. Two key parameters in reflectance physics are substrate absorption and refractive index.

The reflected laser intensity modulates due to changes in the absorption coefficient and the refractive index as a result of variation in the temperature, electric field and free carrier concentration. In addition, the changes in the absorption coefficient depend on the incident photon energy and impurity doping concentration. This chapter reviews the changes in the absorption coefficient and the refractive index due to these effects. The MOS device operations are described, and models for calculating the lengths of the pinch-off region are presented in the discussion on reflectance modulations for MOS transistors.

2.1 Absorption

As a photon travels through a medium, it may be scattered by the array of atoms constituting the material or it may be taken up and converted into thermal energy [36]. The latter process is known as dissipative absorption, with physical model

typically known as Lambert's Law [37]. In the model, the absorption coefficient α is defined as the exponential rate of change in the intensity of an electromagnetic wave as it passes through a given substance. The absorption coefficient depends on the incident photon energy, temperature, electric field and free-carrier concentration [17, 38]. A variation in any of these parameters changes the absorption coefficient and results in a modulation of the reflectivity. This modulation is imparted to the laser beam and detected in the reflected laser intensity. This section discusses each of these parameters in detail.

2.1.1 Absorption Coefficient Variation with Incident Photon Energy

The excitation of an electron from the valence to the conduction band for indirect bandgap material such as silicon (Si) requires the absorption of an incident photon and phonon-assistance due to momentum change where the phonons are quantized crystal lattice vibrations [39, 40]. For pure Si, the absorption coefficient for phonon-assisted absorption is defined as [17]:

$$\alpha_p = A^2 \left[\frac{\left(\hbar\omega - E_g + \hbar\omega_p\right)^2}{\exp\left(\hbar\omega_p / kT\right) - 1} + \frac{\left(\hbar\omega - E_g - \hbar\omega_p\right)^2}{1 - \exp\left(-\hbar\omega_p / kT\right)} \right] \qquad (2.1)$$

where $\hbar\omega$ and $\hbar\omega_p$ are the photon and phonon energies respectively, E_g the indirect bandgap energy, k the Boltzmann constant, T the temperature, and A^2 a constant which depends on the density-of-states, effective mass and temperature.

In addition, the incident photons may also be absorbed by the free carriers in the semiconductor substrate as characterized in the Drude model [41]:

$$\alpha_{fc} = B\lambda^2 N \qquad (2.2)$$

where B is a constant which depends on the free carrier effective mass and mobility, λ the optical wavelength and N the free carrier density.

The variation of the absorption coefficient due to phonon-assisted absorption and free carrier absorption in the NIR region is shown in Figure 2.1 [41] for p-Si at a doping density of $1x10^{19}$ cm^{-3}. Free carrier absorption dominates for incident photon energy lower than the Si bandgap while phonon-assisted absorption dominates for incident photon energy higher than the Si bandgap.

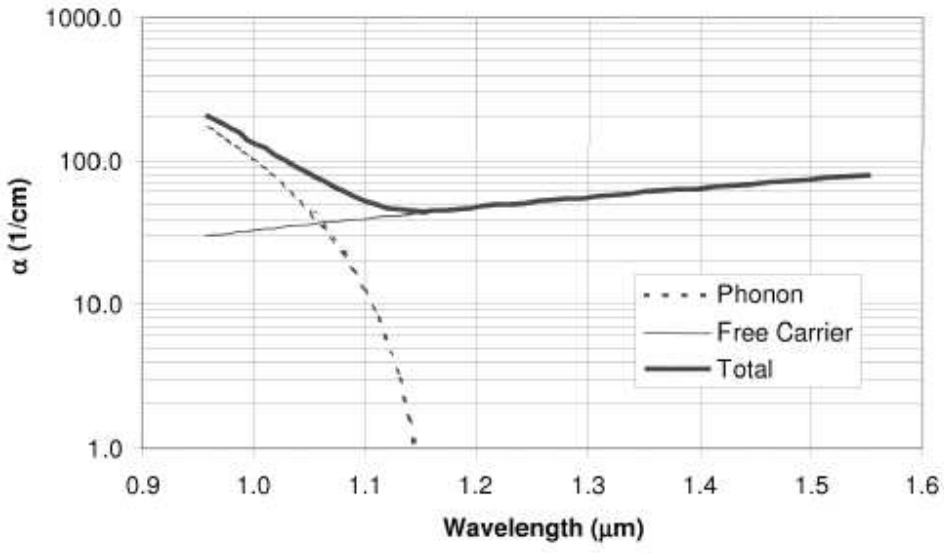

Fig. 2.1: Absorption coefficient versus wavelength [41]

At the incident wavelength of 1.34 μm, free-carrier absorption is the primary absorption mechanism.

2.1.2 Absorption Coefficient Variation with Doping Concentration

The impurity doping concentration determines the free carrier density in the semiconductor substrate, and thus affects the magnitude of free-carrier absorption. Similar to Eq. 2.2, the impurity doping concentration has a linear relation with the absorption coefficient [42]. The absorption model proposed by RA Falk [41] correlates well with earlier empirical data presented by SE Aw [17], E Barta [43], RA Soref [44] and WG Spitzer [42] in the determination of the absorption coefficient for n-type and p-type doped Si at various doping concentrations, and strengthens the hypothesis that free-carrier absorption is the primary mechanism at the incident wavelength of 1.34 μm.

2.1.3 Absorption Coefficient Variation with Temperature

PJ Chernek and JA Orson proposed a simple thermal response model for the Si substrate irradiated by 1.32 μm lasers which accounts for the free carrier and two-photon absorptions at different temperatures [45]:

$$\alpha(T) \approx \left[\alpha_{fc} + (1-R).I_0.\beta_{2P} - \gamma\right]\left(\frac{T}{T_0}\right) + \gamma\left(\frac{T}{T_0}\right)^9 \qquad (2.3)$$

where α_{fc} is approximately 0.0075 cm^{-1} for a Si doping concentration of 10^{15} cm^{-3} at room temperature, (1-*R*) the surface transmittance of Si, I_0 the peak irradiance of the laser in $MW.cm^{-2}$, β_{2P} the two-photon absorption coupling coefficient and is approximately 0.021 $cm.MW^{-1}$ at room temperature, $\gamma \approx 0.0013 cm^{-1}$ the high temperature absorption coefficient, and T_0 the room temperature.

As discussed in the previous sections, free carrier absorption is typically the primary mechanism at the incident wavelength of 1.34 µm. At higher incident photon intensities, two photons may be absorbed to result in the excitation of an electron from the valence to the conduction band, known as the two-photon process [46]. If the laser is in the $MW.cm^{-2}$ irradiance regime and the temperature of the Si substrate is below 650K, the two-photon absorption process dominates. If the temperature exceeds 650K, high temperature absorption dominates [45].

In the adaptation of the thermal response model for reflectance studies, it is noted that the probed laser beam intensities are kept low to mitigate its invasiveness, with irradiance less than 1 $MW.cm^{-2}$. In addition, microelectronic devices do not typically operate beyond 400K. As such, the free carrier absorption remains as the dominant mechanism.

2.1.4 Absorption Coefficient Variation with Electric Field

Independent research by W Franz [47] and LV Keldysh [48] in 1958 predicted that the absorption of Si changes with the application of a high electric field. This

phenomenon is commonly termed electro-absorption. Experimental validation was demonstrated in 1965 by PH Wendland and M Chester [49]. Continuous light from a grating monochromator was focused perpendicular to the surface of pn junctions on the top of Si samples that were biased with varying electric field strength of 10^4 to 10^6 $V \cdot cm^{-1}$. The light traversed the junction, the sample thickness which varies from 50 to 300 µm with resistivities ranging from 1 to 10000 Ω.cm, before entering a PbS detector. Figure 2.2 plots the electro-absorption spectrum of Si [49].

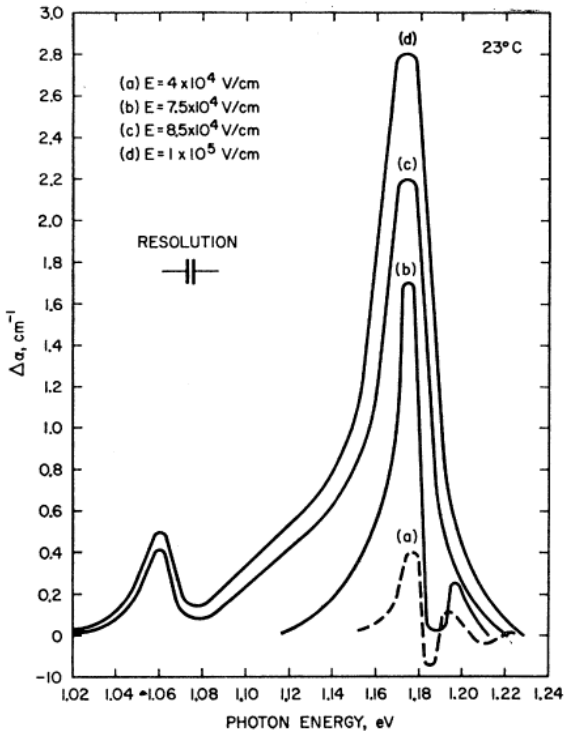

Fig. 2.2: Electro-absorption spectrum of Si [49]

Two major electro-absorption peaks at photon energies of 1.06 eV and 1.175 eV corresponding to 1170 nm and 1055 nm wavelength are observed. The peak at 1.175 eV is associated with phonon emission and remains constant with

temperature. The peak at 1.059 eV is associated with phonon emission and decreases rapidly as the temperature is lowered [49]. Similar experimental observations were made by A Frova and P Handler [50]. Extrapolation of the electro-absorption spectrum to 0.926 eV (corresponding to 1.34 μm wavelength) suggests negligible electro-absorption at that incident photon energy [44].

2.1.5 Absorption Coefficient Variation with Free Carrier Concentration

The optical absorption spectra of c-Si for free electrons and free holes are plotted in Figures 2.3a and 2.3b respectively [44]. For both plots, a valley is observed near 1.0 eV when the sample is undoped. As the free carrier concentration increases, the valley is observed to shift towards the higher photon energy levels. In the NIR region, the absorption coefficient for free electrons is observed to cover a narrower range of values compared to the absorption coefficient for free holes with similar free carrier density.

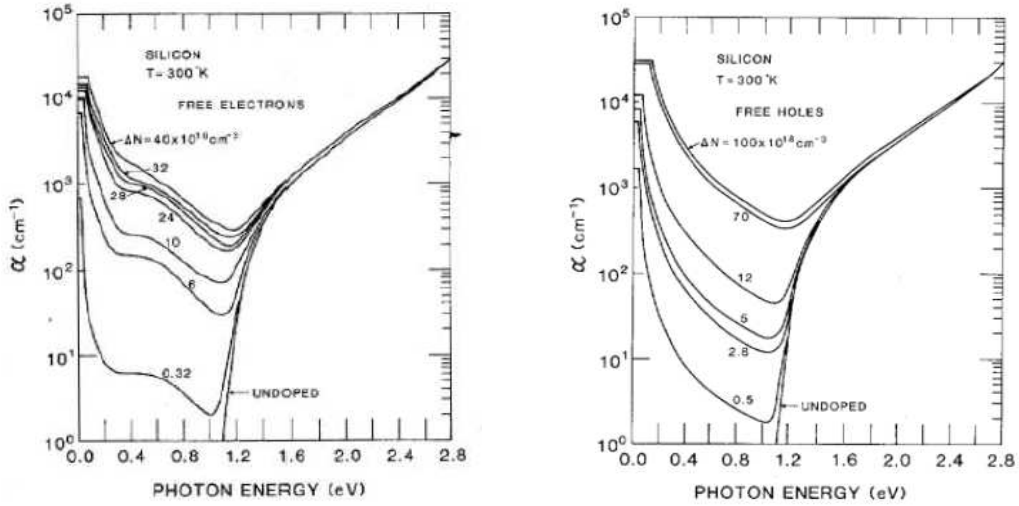

(a) (b)

Fig. 2.3: Optical absorption spectra of c-Si for (a) free electrons, and (b) free holes [44]

At 0.926 eV, the absorption coefficient has a value close to 4.0 when the free electron density is 3.2×10^{17} cm^{-3}. If the free electron density increases to 6×10^{18} cm^{-3}, about 20 times increase, the value of the absorption coefficient increases to about 80 which is also about 20 times larger. Similar magnitude responses are observed for variation in free hole density.

2.2 Refractive Index

The reflectance modulation of the reflected beam due to an incident laser depends on the refractive index of the media which varies with temperature, electric field and free-carrier concentration. This section discusses each of these parameters in detail.

2.2.1 Refractive Index Variation with Temperature

When the temperature increases, the material undergoes thermal expansion and the density decreases. This causes the refractive index to decrease. On the other hand, the polarizability increases with temperature due to limited degree of freedom in a crystal lattice arrangement, causing the refractive index to increase. Depending on the incident photon energy, either thermal expansion resulting in density change or temperature-dependent polarizability variation may dominate. An empirical model of the refractive index of Si *n(E,T)* as a function of temperature is as follows [51]:

$$n(E,T) = \sqrt{4.386 - 0.00343*T + \frac{99.14 + 0.062*T}{E_g^2 - E^2}} \qquad (2.4)$$

where *T* is the temperature of the material in degree Celsius, *E* is the incident photon energy in eV and E_g=3.652 eV is a constant.

The second term represents the thermal expansion effect and the last term represents the polarizability effect. Typical error in the function is limited to ±0.01.

2.2.2 Refractive Index Variation with Electric Field

Electro-refraction is often used to describe the change in refractive index when an electric field is applied. RA Soref and BR Bennett made use of empirical data in the electro-absorption spectrum as shown in Figure 2.2 to calculate the corresponding changes in refractive index for each applied electric field, by using

the Kramers-Kronig coupling relation between the two parameters [44]. A computer routine was used to interpolate values between entered points, and to provide a function. Subsequently, the electrorefraction spectrum was plotted, as shown in Figure 2.4

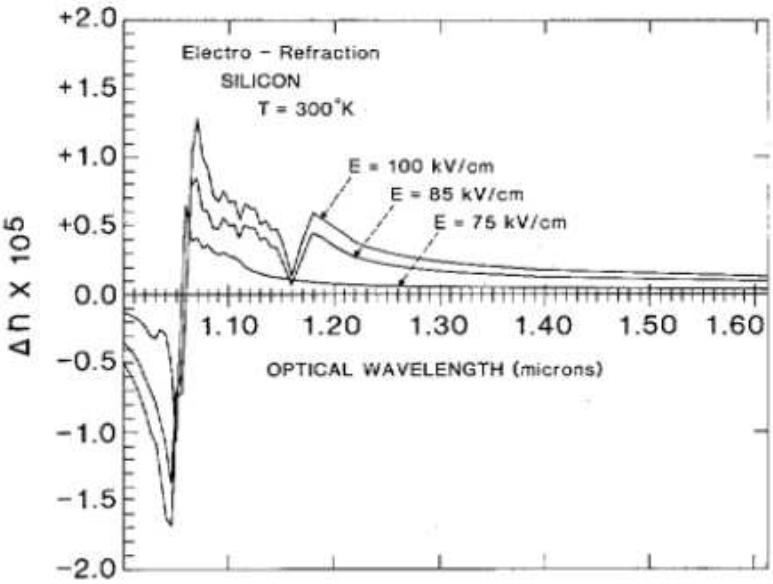

Fig. 2.4: Electrorefraction versus wavelength [44]

Two electro-absorption peaks (in Figure 2.2) are observed at 1055 nm and 1170 nm. At these two wavelengths, electrorefraction is observed to be negligible. When the incident wavelength is less than 1055 nm, the refractive index is observed to modulate negatively with the applied electric field. At longer wavelengths, the refractive index modulation is positive. Peak negative refractive index modulation is observed at 1045 nm, and peak positive refractive index modulation is observed at 1065 nm. As the applied electric field increases, secondary peaks and valleys are observed between 1055 nm and 1170 nm. For

all applied electric field strengths, the variation of the refractive index is in the range from 10^{-6} to 10^{-5}.

2.2.3 Refractive Index Variation with Free Carrier Concentration

Carrier refraction is used to describe the variation of the refractive index with free carrier concentration. Based on the Drude model [44], the change in refractive index due to changes in free electrons and free holes is as follows:

$$\Delta n = -\left(\frac{q^2\lambda^2}{8\pi^2 c^2 \varepsilon_0 n}\right)\left(\frac{\Delta N_e}{m_e^*} + \frac{\Delta N_h}{m_h^*}\right) \tag{2.5}$$

where q is the electronic charge, ε_0 is the permittivity of free space, n is the refractive index of unperturbed c-Si, ΔN_e is the change in free electron density, m_e^* is the effective mass of electrons, ΔN_h is the change in free hole density, and m_h^* is the effective mass of holes.

Figure 2.5 shows the carrier refraction spectrum in c-Si at 1.3 μm wavelength [44]. The refractive index increases when carriers are depleted and decreases when carriers are injected. Each decade increase in free carrier density results in a decade increase in the magnitude of the refractive index modulation.

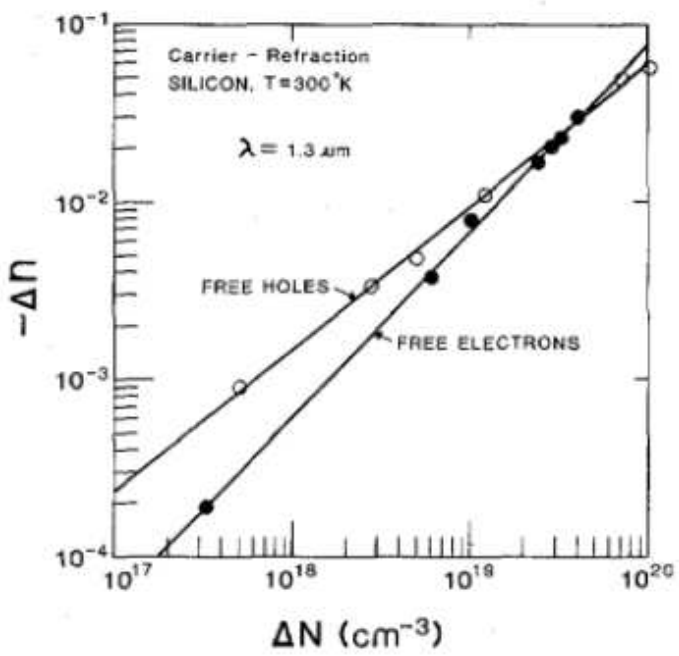

Fig. 2.5: Carrier refraction in c-Si at 1.3 µm wavelength [44]

2.3 Reflectance Modulation for MOS Transistor

In an operating MOS transistor, the free carriers in the channel are modulated by the gate bias V_{GS} and drain bias V_{DS}. The temperature in the channel rises due to the flow of I_{DS} current. The electric field is significant when the MOS device is in saturation mode. As a result, significant laser reflectance modulation in an MOS device is expected. Understanding the MOS device operation is pertinent to insights into laser reflectance modulations of an operating MOS device. This section describes the operations of an MOS transistor and presents models that are used in the determination of the pinch-off region.

2.3.1 MOS Device Operations

An enhancement-mode NMOS device is assumed in this discussion. Without any applied bias, there is no conduction in the channel and the transistor is turned off. Figure 2.6 shows the typical I_{DS}-V_{DS} characteristics of the NMOS transistor [52].

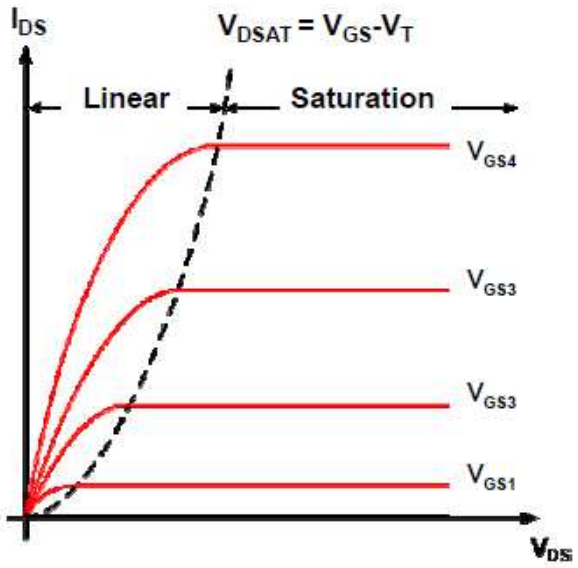

Fig. 2.6: I_{DS}-V_{DS} characteristics of NMOS device [52]

As a voltage V_{GS} is applied, a depletion layer is formed in the channel under the gate. The depletion layer width increases as V_{GS} increases. When V_{GS} exceeds V_T which is the threshold voltage marking the depletion-inversion transition-point, an inversion layer of minority charge carriers is formed on the surface of the channel directly under the gate oxide, forming a conduction path between the source and drain. As V_{GS} increases further, the free carrier density in the inversion layer increases, and the depletion layer width remains constant [53]. The onset of the inversion layer marks the inversion mode. Figure 2.7a is a

qualitative representation of the NMOS transistor in inversion mode. Figure 2.7b was simulated to determine the free electron density in the inversion layer for an NMOS transistor with 65 nm channel length and 32 nm channel width [54]. The variation of the free electron density along the channel is observed to be small.

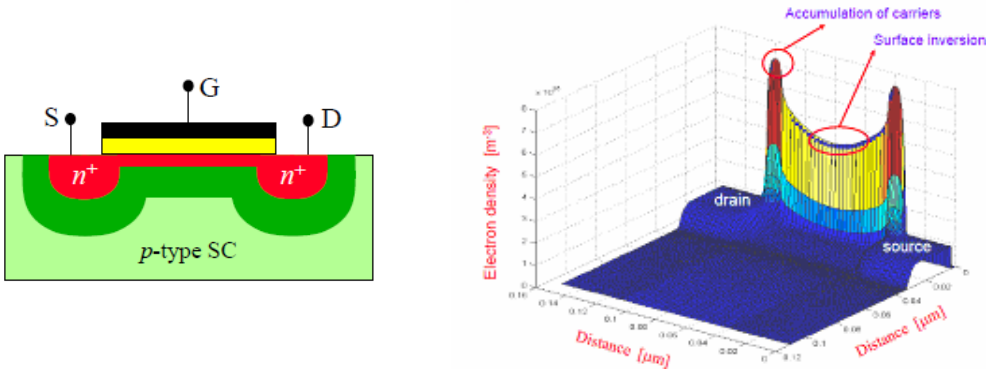

(a) (b)

Fig. 2.7: (a) Qualitative representation, and (b) free electron density along the channel of an NMOS transistor in inversion mode [54]

If a small drain voltage V_{DS} is subsequently applied, a current flows from the drain to the source through the conducting channel. As seen in Figure 2.6, the drain current I_{DS} increases linearly with the applied V_{DS}. The NMOS transistor is in linear mode. Figure 2.8a is a qualitative representation of the NMOS transistor in linear mode. The depletion regions in the substrate around the drain are observed to increase compared to the source due to the applied V_{DS} [53]. The free electron density in the channel near the drain is observed to decrease since the applied V_{DS} reduces the effective potential in that region [54].

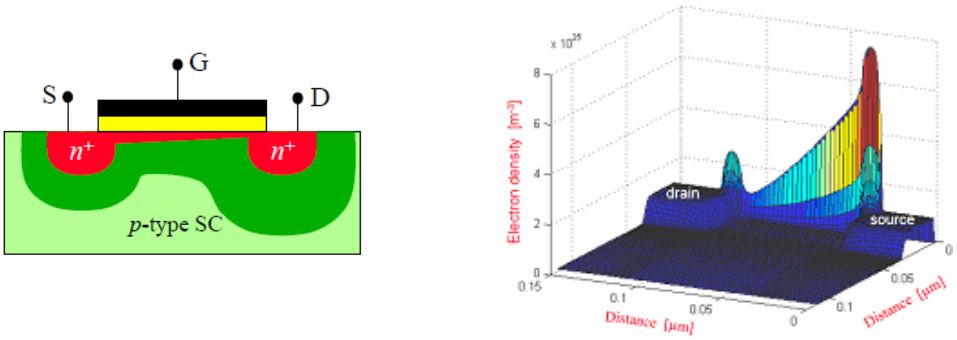

(a) (b)

Fig. 2.8: (a) Qualitative representation, and (b) free electron density along the channel of an NMOS transistor in linear mode [54]

As V_{DS} increases further, the depletion layer widths around the drain increase further, as shown in Figure 2.9a. The free electron density at the drain-end gets depleted and eventually reaches a pinch-off point whereby the carrier density at that point is very much smaller than the rest of the channel and almost equivalent to the carrier density in bulk silicon. This is illustrated in Figure 2.9b. The NMOS transistor is in pinched-off mode. In Figure 2.6, the intersection points of the I_{DS}-V_{DS} curves with the dotted line mark the pinched-off points.

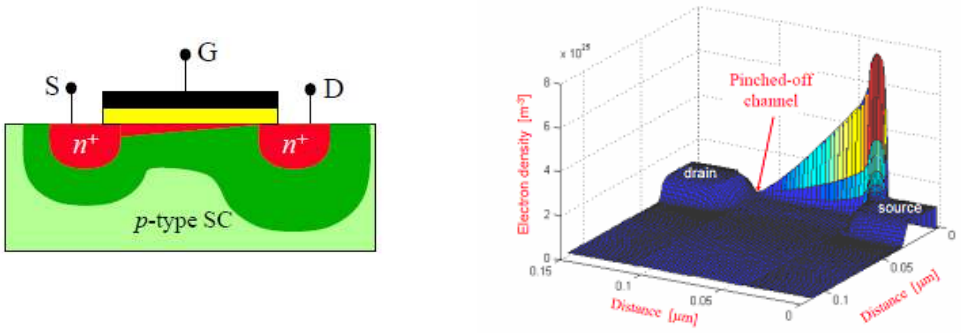

(a) (b)

Fig. 2.9: (a) Qualitative representation, and (b) free electron density along the channel of an NMOS transistor in pinched-off mode [54]

Further increase in V_{DS} moves the pinch-off point towards the source and the formation of a depletion layer with width ΔL, as shown in Figure 2.10. The voltage at the pinch-off point remains the same, and is commonly termed V_{DSAT}. The excess voltage is dropped across ΔL.

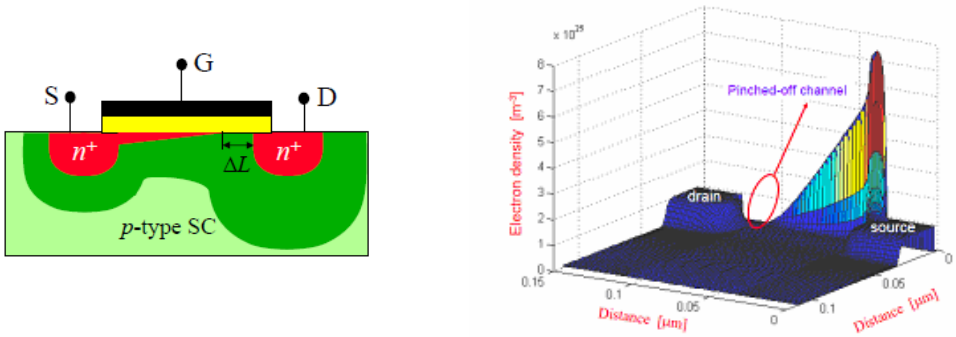

(a) (b)

Fig. 2.10: (a) Qualitative representation, and (b) free electron density along the channel of an NMOS transistor in saturation mode [54]

The depletion region ΔL is highly resistive [55] with very high electric field [56] and temperature [57] compared to the rest of the channel, and is commonly known as the length of the pinch-off region. In short-channel models, the electric field in the pinch-off region exceeds the saturation electric field when V_{DS} exceeds V_{DSAT}, resulting in velocity saturation of the free carriers [58], and thus the pinch-off region is also known as the velocity saturation region in short-channel models, with ΔL also known as the length of the velocity saturation region [59]. The next sections discuss analytical models to determine ΔL.

2.3.2 Single Abrupt Junction Model

When an NMOS transistor is in saturation mode, the pinched-off region is depleted, with free carriers similar to the majority charge carriers in bulk Si. The drain and pinched-off region forms a pn junction in reverse-biased mode, as shown in Figure 2.11 [53].

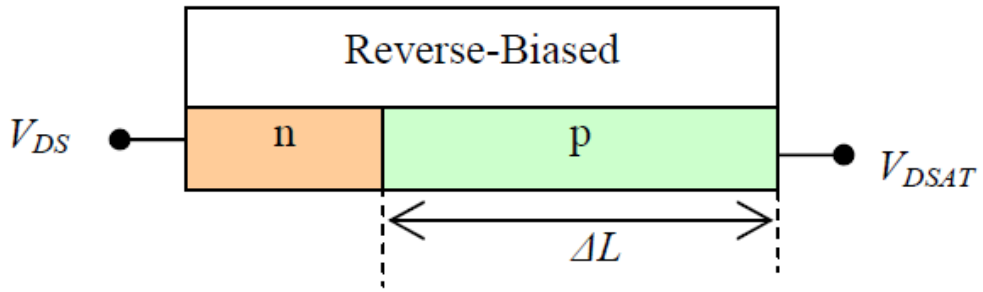

Fig. 2.11: Single-abrupt iunction model [53]

The single abrupt junction model is based on analytical derivation of the single reverse-biased pn junction. Since V_{DSAT} remains constant, the depletion layer width at the PN junction depends on the applied V_{DS}. As V_{DS} increases, the depletion layer width also increases. The depletion layer extends on both sides of the junction interface, with the total depletion width ΔL_{taj} for a two-sided abrupt junction expressed as [53]:

$$\Delta L_{taj} = \sqrt{\frac{2\varepsilon_{Si}}{q}\left(\frac{N_A + N_D}{N_A N_D}\right)(V_{DS} - V_{DSAT})} \tag{2.6}$$

where ε_{Si} is the permittivity of Si, q is the elementary charge, N_A and N_D are the acceptor and donor concentration on each side of the junction.

Since $N_A >> N_D$, the depletion width may be approximated to be only within the p-side of the junction where ΔL is the length of the pinch-off region. Eq. (2.7) reduces to ΔL_{saj} for a single-sided abrupt junction:

$$\Delta L_{saj} = \sqrt{\frac{2\varepsilon_{Si}}{qN_D}(V_{DS} - V_{DSAT})} \tag{2.7}$$

2.3.3 Pseudo-Two-Dimensional Model by Ko

In the single abrupt junction model discussed in Section 2.3.2, the oxide field and the mobile charges that result from the field have been ignored. To include these effects and to derive an exact solution for the length of the pinch-off region, E

Mansy solved the Poisson's equation and the current transport equation simultaneously by replacing the total charge density $\rho(x,y)$ with the sum of the depletion charge density qN_A and the mobile charge density qN_m. The general form for the Poisson's equation becomes [60]:

$$\frac{\partial^2 V(x,y)}{\partial x^2} + \frac{\partial^2 V(x,y)}{\partial y^2} = \frac{qN_A(x,y) + qN_m(x,y)}{\varepsilon_{Si}} \qquad (2.8)$$

A rigorous calculation of the field near the drain is only possible through computer-aided solution of the two-dimensional Poisson equation. PK Ko obtained an approximate solution ΔL_{KO} by applying Gauss' law to the charge enclosed in a volume surrounding the high-field region, with the inclusion of effects due to velocity saturation and junction depth [58].

$$\Delta L_{Ko} = P_{Const}.\ln\left(u + \sqrt{u^2 + 1}\right) \qquad (2.9)$$

where t_{ox} is the oxide thickness, x_j the junction depth, $P_{Const} = \sqrt{\frac{\varepsilon_{Si}}{\varepsilon_{ox}} t_{ox} x_j}$ and $u = \frac{V_{DS} - V_{DSAT}}{P_{Const}.E_S}$

RS Muller simulated the electric field across the channel for both single abrupt junction model and two-dimensional Poisson model [56], as shown in Figure 2.12 [59]. The solid curve is calculated with the two-dimensional Poisson. The field has approximate hyperbolic-cosine dependence in the velocity saturation region. The solid line is calculated with the single abrupt junction model.

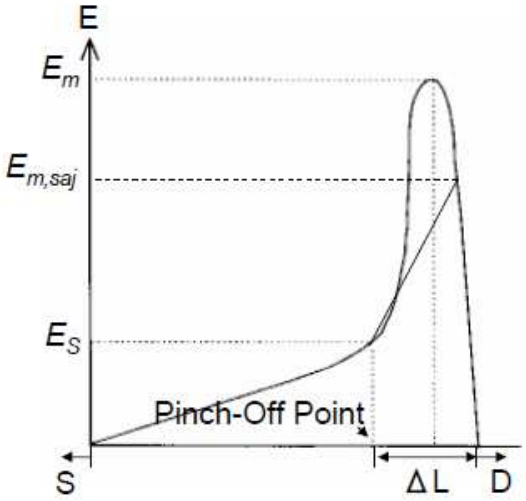

Fig. 2.12: Calculated electric field versus position in the channel for both two-dimensional Poisson model and single abrupt junction model [56].

The saturation electric field E_S marks the pinch-off point. The maximum electric field E_m occurs in the pinched-off region, as calculated using the two-dimensional Poisson model. Using the single abrupt junction model, the calculated maximum electric field $E_{m,saj}$ underestimated the maximum electric field. The two-dimensional Poisson model is accurate for modeling the channel field. The Pseudo-two-dimensional model put forth by Ko is used to explain the experimental data in the characterization of MOS transistors using reflectance measurements.

Chapter 3 Review of Reflectance Modulation Systems and Techniques

In Chapter 2, reflectance physics is reviewed. The reflected laser intensity depends on the absorption coefficient and refractive indices of the media, and its modulation depends on the variation of the parameters with temperature, electric field and free carrier concentration. The electric field and free carrier concentrations are commonly classified together as electro-optical effects [28]. This chapter reviews laser reflectance systems and techniques based on temperature and electro-optical effects. The review is organized from the simplest optical implementation to the most complex. Discussion covers flux-based charge-coupled-device (CCD) systems and single-laser-beam-based photodiode systems. The latter is further classified based on amplitude and phase detection schemes which include implementations based on single and dual lasers, continuous-wave and pulsed laser, fixed and scanning optical beam, interferometric and non-interferometric optical paths. The spatial resolution and telecentricity of laser reflectance systems are also discussed.

3.1 Flux-based CCD Systems

In the early 2000s, CCD camera-based thermoreflectance microscope system was introduced to measure reflectance modulations due to temperature variations of metal thin films. Figure 3.1 shows the optical setup of a frontside CCD camera thermoreflectance system which is typical of an imaging optical microscope [61].

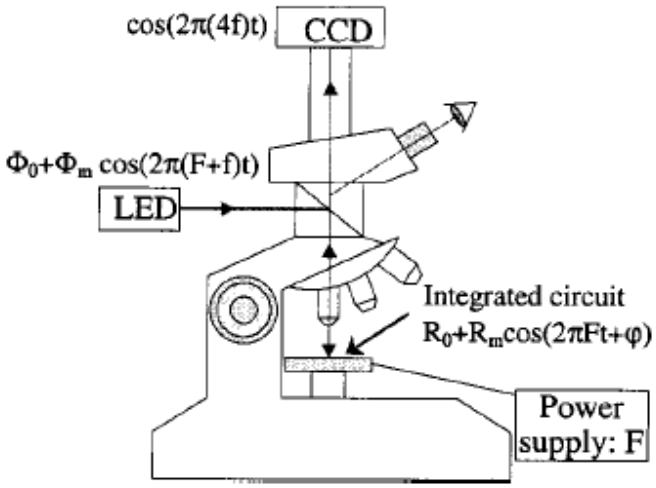

Fig. 3.1: CCD camera-based thermoreflectance system [62]

Illumination from a light emitting diode (LED) at a single wavelength is incident on the sample surface after travelling through the optics, get reflected and travel through the optical system again. A beam splitter diverts the return beam to the CCD array for detection. The optical magnification is changed manually by rotating the turret of objective lenses at different magnifications. The sample is placed on the stage, and is manually moved to the probed location with navigation viewed through the eye-pieces. A study was carried out to determine the optimum illumination wavelength to use [62]. It was found the wavelength selection depends on the properties of the probed material. Perhaps for simplicity, many later CCD-based thermoreflectance systems use broadband white light to provide illumination [63, 64].

Research and development efforts were separately explored by research groups in France and the United States [62, 63]. Given that traditional CCD camera did

not have enough sensitivity to detect the small thermoreflectance signal, the group in France employed lock-in detection techniques to improve the signal-to-noise (SNR) ratio for detection [62]. The group in the United States employed a fast temporal detection scheme and applied different gains to the AC and DC signals of each pixel which is then heterodyne filtered with a fast fourier transform (FFT) to improve the SNR [63].

Using an Indium Gallium Arsenide (InGaAs) CCD array which has a quantum efficiency greater than 0.6 in the wavelength range between 1.0 and 1.7 µm, G. Tessier demonstrated backside thermal imaging of integrated circuits by adapting the classical imaging microscope [64]. In addition, a solid immersion lens (SIL) was used to show that spatial resolution up to 440 nm can be achieved. CCD-based thermoreflectance systems have thermal resolutions of 50-100mK [63, 64].

3.2 Single-laser-beam Photodiode Systems

A single-laser-beam photodiode system differs from CCD-based systems with the distinction that the optical beam is incident on a single spot and the reflected optical beam is detected by a photodiode representing a single pixel. The incident optical power of the single-laser-beam photodiode system is larger than CCD-based systems, so the detection sensitivity of the laser reflectance modulation is improved [23, 65]. These systems are confocal if the out-of-focus signals are eliminated from entering the detector, most often with an exit pupil in

front of the detector [66]. Figure 3.2 shows the first confocal microscopy system invented by Marvin Minsky at Harvard University in 1957 [67].

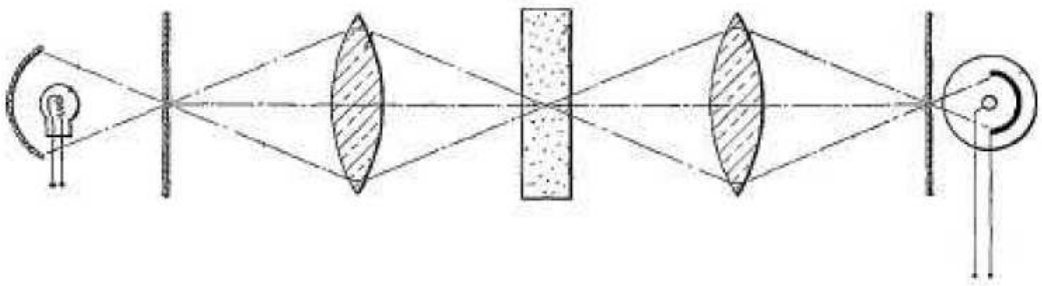

Fig. 3.2: First confocal microscopy optical setup [67]

In a confocal microscopy system, a single point on the object axis is illuminated, and the signal from that point is received on the same or an identical lens at a point detector [68]. Compared to other imaging microscope, the confocal microscope has the advantage that light scattered from parts other than the illuminated point on the DUT is rejected from the optical system [66]. The confocal microscopy system also has the following advantages [67]:

(i) Increased effective resolution

(ii) Improved signal-to-noise ratio

(iii) Electronic adjustment of magnification

There is no further classification in terms of confocal and non-confocal microscopy systems due to difficulties in ascertaining relevant details from existing literatures. However, further classification may be made based on amplitude modulation (AM) or phase modulation (PM) detection schemes.

Amplitude modulation detects the change in the reflected laser intensity due to temperature or electro-optical effects which also result in a phase change of the reflected laser beam. Using an interferometer with a reference beam together with the probed beam, the resultant reflected intensity correlates to the phase modulation [69]. It is reported phase modulation detection resulted in stronger signals compared to amplitude modulation detection, as shown in Table. 3.1. This section discusses the implementations based on single and dual laser, continuous-wave and pulsed laser, fixed and scanning optical beam.

Table 3.1 – Phase versus amplitude modulation [69]

	Modulation Level (ppm)
DUT Amplitude Signal	100-500
DUT Phase Signal	1000-2000

3.2.1 AM using Single Pulsed Laser with Fixed Optical Beam

In the mid-1990s, Intel developed a system to detect laser reflectance modulations due to electro-optical effects [65], as shown in Figure 3.3. It was named laser voltage probe (LVP) and has since been widely used by other researchers to represent similar systems and techniques.

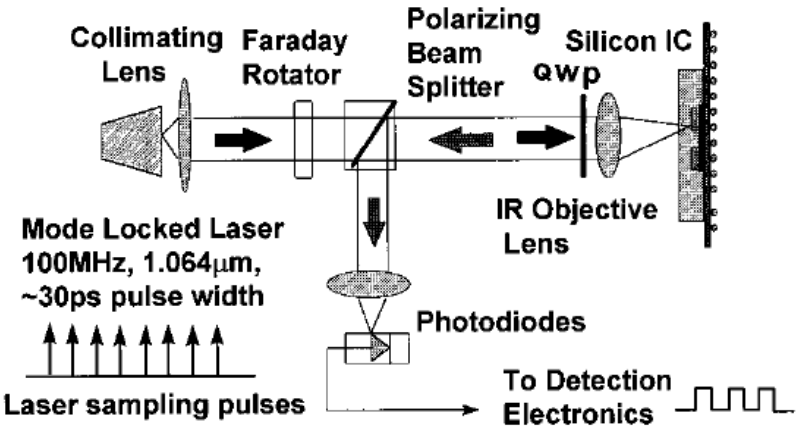

Fig. 3.3: Simplified schematic of LVP system used in Intel [65]

A mode-locked laser at 1064 nm wavelength is used to generate laser light pulses at a repetition rate of 100 MHz which is phase locked to the master clock oscillator in the tester being used to drive the IC, and could achieve measurement bandwidth of 12 GHz [65]. A collimating lens is used to ensure parallel rays enter the optical system. A Faraday Rotator is used to optically isolate the laser source to ensure its stability by mitigating back-reflection. The probe beam passes through the beam splitter, is focused on the pn junction of a backside prepared IC, and reflected from the metal contact at the front of the IC, returns back through the same optical path, and is diverted by a beam splitter to the photodiodes. The optical beam and apparatus are fixed. The sample has to be translated to move the probe beam to the pn junction.

It was observed the reflectance modulation of a laser source at 1064 nm wavelength is larger than another at 1.34 μm wavelength as the electro-absorption at 1.064 μm wavelength is more significant than those at 1.34 μm

wavelength [65]. This conclusion supports earlier experimental evidence provided by PH Wendland and M Chester in 1965 [49].

However, a laser source at 1.064 µm wavelength is more invasive due to carrier stimulation compared to a similar laser source at 1.34 µm wavelength which causes thermal stimulation [6]. The invasiveness of the 1.064 µm laser may be mitigated by minimizing the optical probe power which also reduces the sensitivity of the reflectance modulations [65].

3.2.2 AM using Single CW Laser with Fixed Optical Beam

The first frontside application of thermoreflectance is demonstrated by a research group at the University of Bordeaux in the early 1990s, as shown in Figure 3.4 [70]. Polarized CW laser at 632.8 nm wavelength is used with a laser source power of 1 mW.

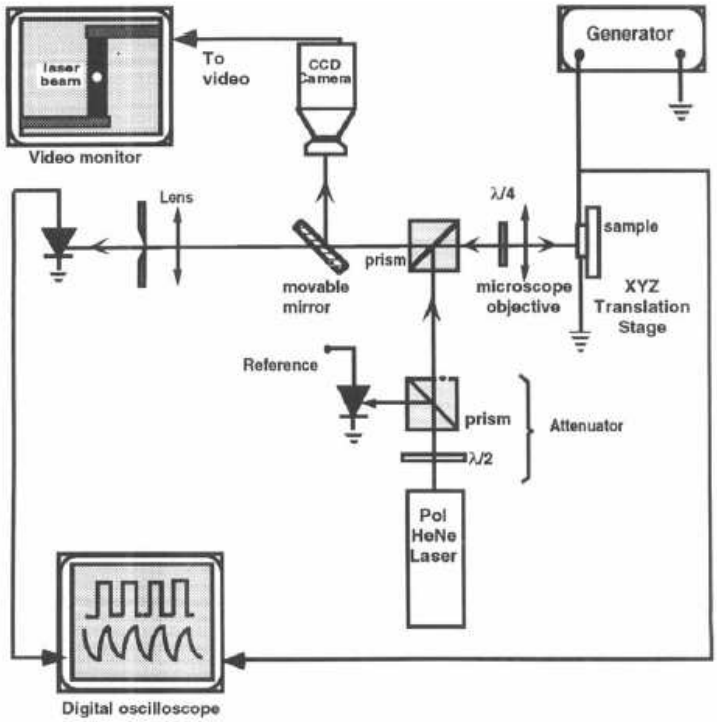

Fig. 3.4: Thermoreflectance based on reflectometry [70]

The laser beam passes a variable light intensity attenuator made of a half wave plate and a polarizing beam splitter. The intensity of the incident laser power is attenuated by rotating the half wave plate, and may be monitored with the reference signal. The block also ensures optical isolation of the incident laser. The beam is subsequently directed and focused onto the sample surface by another polarizing beam splitter. A quarter wave plate in front of the objective lens rotates the linear polarization of the reflected laser beam by 90º, allowing the reflected beam to be directed to the photodiode. The optical beam and apparatus are fixed. The probed beam is moved into position by translating the sample with the XYZ translation stage. For navigation purpose, a movable mirror is placed in

the path of the reflected beam to direct the laser beam to a CCD detector and output to a video monitor.

A p-doped diffused Si resistive sample was used. Periodic Joule heating was applied by passing current pulses of 76 mA at 40 µs duration through the resistor, and the reflectance modulations were observed. The system was reported to have a spatial resolution of 1 µm, thermal resolution of 10 mK and system frequency up to 10 MHz [70].

The group realized that accurate temperature determination from the frontside reflectance modulations requires the passivation thickness to be known. Figure 3.5 shows the reflectance modulation differs greatly at different passivation thicknesses at similar experimental conditions. Sample A is passivated with oxide thickness 0.53 µm and sample B is depassivated with residual oxide thickness 0.014 µm [71]. As such, frontside-based thermoreflectance techniques require calibrations of the samples [34, 72], limiting the usefulness of the techniques.

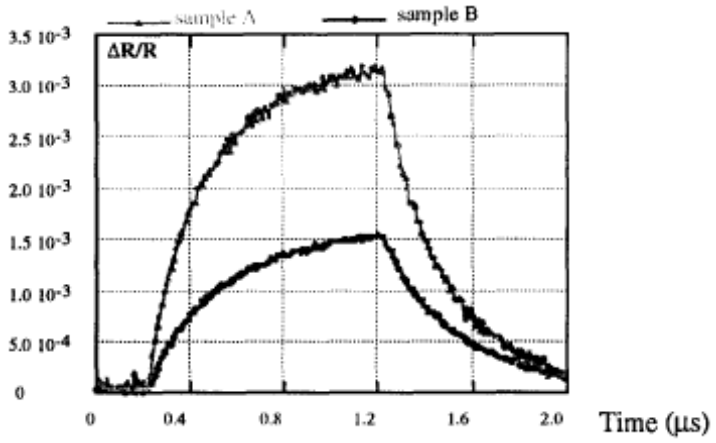

Fig. 3.5: Temporal relative reflectance response of two samples to a 1 μs, 70 mA current [71]

3.2.3 AM using Dual CW Laser with Fixed Optical Beam

An early application of thermoreflectance effects was demonstrated in the early 1980s to study optical-related material properties of probed samples, as shown in Figure 3.6. No electrical bias was provided to the samples. Heat is applied to the DUT with one heating beam. Another probe beam is used to measure the reflected intensity modulation. Both beams are incident normal to the sample surface, with the two spots displaced 2 μm apart. This is a frontside-based technique. The optical beam and apparatus are fixed. The sample is moved into position by translating the sample.

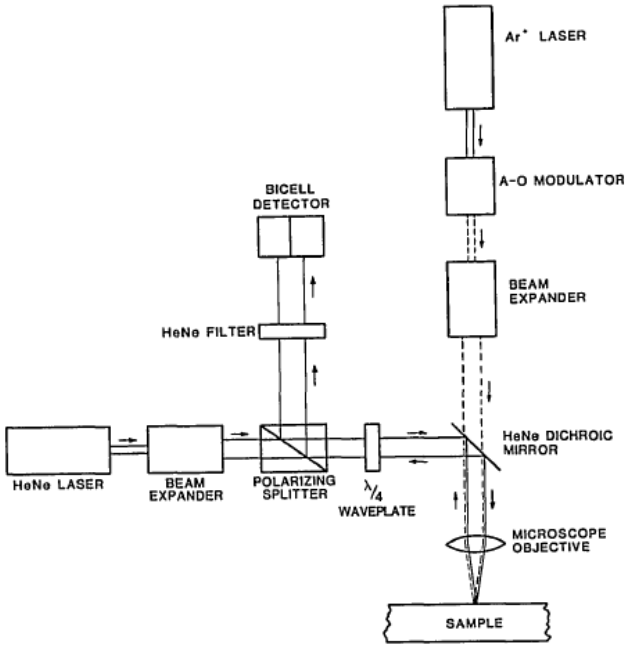

Fig. 3.6: Laser beam deflection technique used for thin-film thickness measurements [73]

The heating beam is a laser source at 488 nm wavelength and has approximately 30 mW sample incident power. The probe beam is a laser source at 633 nm wavelength and has approximately 2 mW sample incident power. The laser spot on the sample is 2 to 4 μm. The reflected intensity of the probe beam is measured by a bicell detector.

When the heating beam is focused and incident on the sample surface, the surface at that spot is heated up. This results in thermoelastic deformation due to thermal expansion at that point, with resulting modulation of the reflected laser intensity for the probe beam. This technique has been used in the study of surface optical and thermal properties, and to measure thickness of opaque and transparent thin films [73, 74].

3.2.4 AM using Single CW Laser with Scanning Optical Beam

Another research group at Stanford employed the setup shown in Figure 3.7. to carry out frontside-based thermoreflectance studies on metal interconnects and microdevices such as silicon-on-insulator (SOI) transistors. The sample is placed on a probe station, and the laser beam is scanned across the sample using scanning mirrors. The system is among the first in demonstrating laser reflectance modulations using a scanning laser beam. The probe laser beam has a wavelength of 825 nm, with incident power less than 1 mW. Heat is applied by electrically-biasing and pulsing the sample, resulting in Joule heating [70].

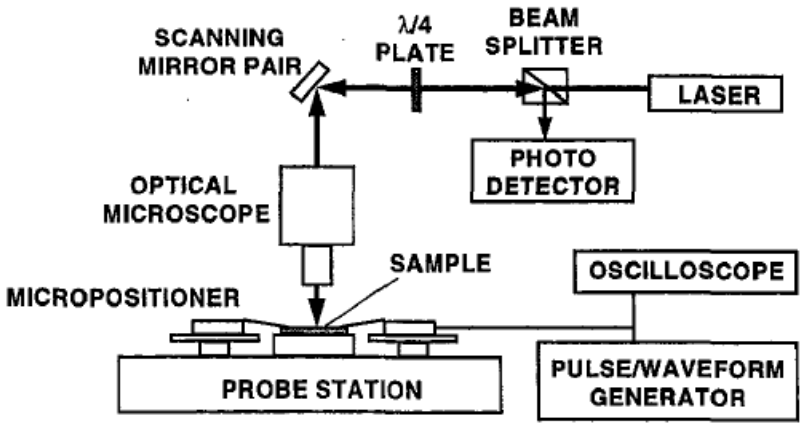

Fig. 3.7: Scanning laser-reflectance thermometry [34]

An incident linearly polarized laser beam passes through the beam splitter, is circularly polarized by the quarter-wave-plate, and scanned across the sample surface by the scanning mirrors. The reflected beam traverses through the same optical path. After passing through the quarter-wave-plate again, the laser beam

is linearly polarized again, with a rotation of 90º to the optic axis. The reflected beam is diverted to the photo-detector by the beam splitter. The system demonstrated a thermal resolution of 100 mK, spatial resolution of 1 µm and temporal resolution near 10 ns.

A similar laser-scanning optical system has also been used for backside reflectance modulation of electro-optical effects, as shown in Figure 3.8. The optics used is typical of a scanning optical microscope (SOM) system. The laser source is a CW laser at 1.319 µm wavelength. The use of a spectrum analyzer in signal detection removes the need to tap internal trigger signals from the IC, simplifying the experimental technique [75]. Single-point voltage sweep or laser-scanned modulation map may be carried out.

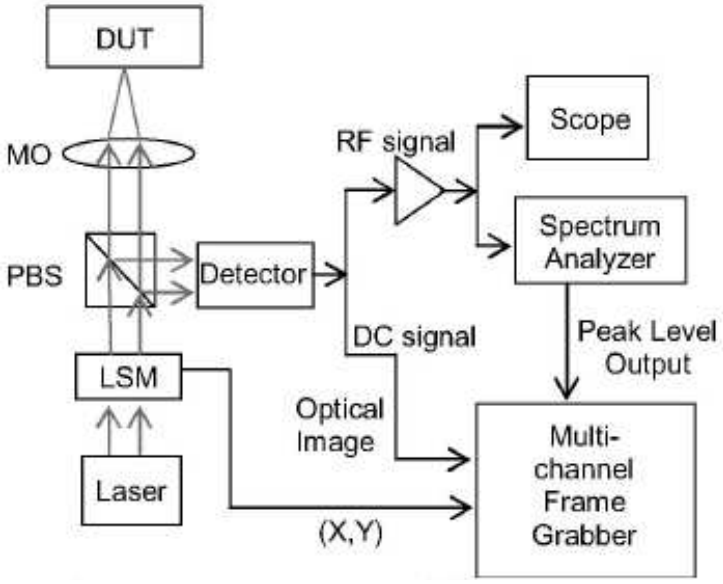

Fig. 3.8: Simplified LVP measurement system [76]

A refractive solid-immersion-lens (RSIL) was used together with the setup shown in Figure 3.8 to detect timing information in microelectronic devices [77]. The spatial resolution was enhanced to 200 nm, at a bandwidth of 7 GHz. The system demonstrated successful measurements of 50 ps response time from NMOS and PMOS transistors. Laser Timing Probe (LTP) was coined to refer to such systems.

3.2.5 PM using Single CW Laser with Fixed Optical Beam

The first successful application of backside laser reflectance modulation due to electro-optical effects in the measurement of timing information from electrical signals in Si integrated circuits was demonstrated by Heinrich based on his doctoral research at Stanford University in the 1980s [23, 78]. Figure 3.9a shows the developed system. A CW laser at 1.3 µm wavelength is used. A birefringent Nomarski prism is used to separate the incident laser into a probe beam and a reference beam that are separated 74 µm apart. The probe beam is incident on the active device and its reflectance is modulated by electro-optical effects of the active device [78].

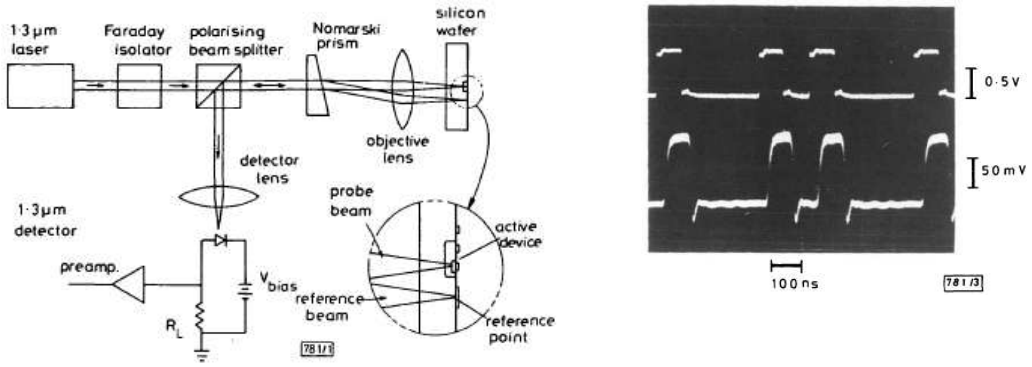

(a) (b)

Fig. 3.9: (a) Backside optical probe system using reference beam and (b) measured timing waveform of a 100MHz digital signal [78].

Phase modulation of the probe beam relative to the reference beam produce polarization modulation of the combined return beam which is sensed by the polarizing beam splitter and converted to an amplitude modulation at the photodetector [79]. The reference beam is used to improve the signal-to-noise (SNR) ratio, so that the minute modulation due to electro-optical effects can be identified.

In Figure 3.9b, the waveform on top was the probed electrical signal with 0.5V amplitude and frequency of 100 MHz. The waveform below was reproduced from reflectance measurements. The system was able to accurately measure the timing information of the 100 MHz digital signal, but unable to determine its voltage amplitude. Due to the strong dependence of the signal amplitude on focus and spot position, device geometry and details of the manufacturing process, it is not possible to accurately determine the signal voltage [80].

3.2.6 PM using Dual Pulsed Laser with Fixed Optical Beam

3.2.6.1 Non-interferometric

In the early 2000s, a research group at Credence Systems developed a system to detect polarized electroabsorption of MOS devices. The system is referred to as Polarization Difference Probing technique (PDP). When an MOS device is in saturation, the electric field in the pinch-off region of the channel is very high and directional along the y-axis. When gate or drain voltage is applied, the resultant electric field is always along the x-axis or/and y-axis. So, there is negligible electric field modulation along the z-axis. Figure 3.10 illustrates the point.

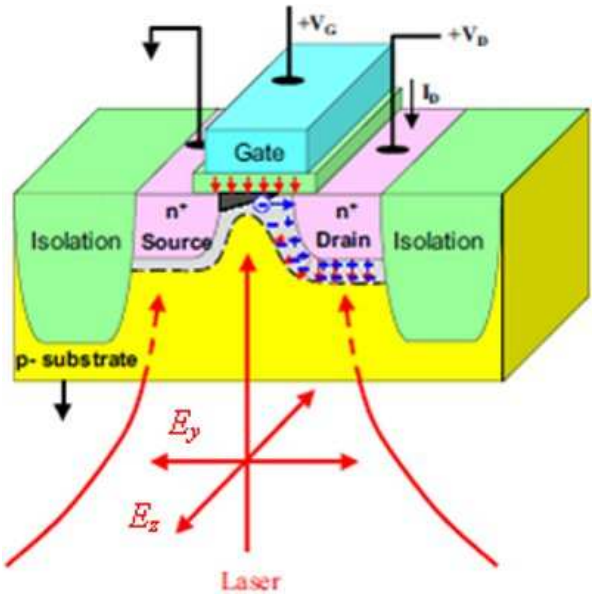

Fig. 3.10: Polarization Difference Probing [81]

The successful implementation of the technique requires two identical and orthogonal linearly polarized laser beams (E_y and E_z) to be incident at the channel of an MOS device with alignment to the y and z directions of the MOS

device. The PDP optical path is shown in Figure 3.11. The top half shows the incident path and the bottom half shows the return path. Two orthogonal, linearly polarized laser beams are equivalent to a resultant beam at an angle of 45º.

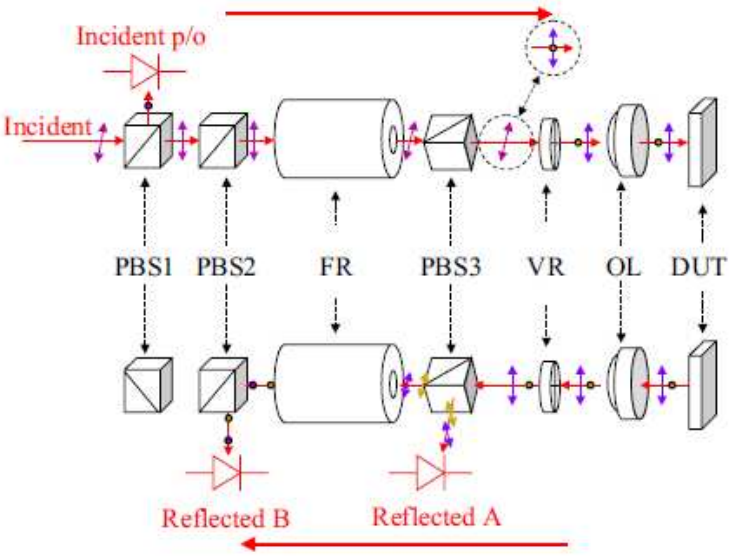

Fig. 3.11: PDP optical path [81]

When the incident beam passes through polarizing beam splitter PBS1 and PBS2, only the vertically polarized beam propagates through. The Faraday Rotator (FR) rotates the polarization state of the beam by 45 degrees and polarizing beam splitter PBS3 is oriented in that same direction. The variable-retarder (VR) has fast and slow axes along the y and z axes to result in two equal-amplitude and orthogonally polarized beams.

The reflected beams traverse back through the same optics. The reflectance modulation of the E_y and E_z beams are detected separately by photon detectors A and B, and digitally processed to determine the difference between the two

signals which correspond to reflectance modulation due to the polarization difference [81].

To reduce noise, an elaborate scheme that employs two pulsed lasers at 1.064µm is used. With this scheme, there is no reference arm that is commonly used in interferometers for phase detection, removing the need to match the path-length and the power between the two interferometer arms. However, aligning the incident laser to the required orientation is difficult. A mode-locked laser with 10 ps pulse width has been used to increase the system bandwidth to 20 GHz [81].

3.2.6.2 Interferometric

The earliest LVP systems became commercially available in the 1990s. It incorporated a Michelson-type Interferometer [36] into the optics where the reference beam is directed to a reference arm that is not on the IC, as shown in Figure 3.12. This was done to overcome the difficulty of having the reference beam on the same IC as the transistor density increased in accordance to Moore's law. Checkpoint Technologies has been credited with the first implementation [69].

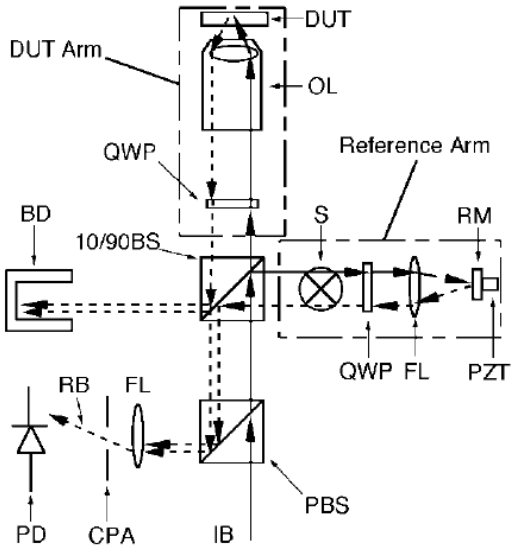

Fig. 3.12: Basic phase interferometer detection system [69]

In such systems, the light source is split into two arms; 90% of the intensity goes to the DUT, 10% goes into the reference arm and is reflected by a mirror at the end. The reference arm is adjusted so that the combined reflected signal from the two arms is not distorted due to phase offsets. When the DUT is modulated, the interferometer measures the phase offset due to the modulation.

It is necessary to tune the reference beam in the reference arm such that the phase modulation of the system has good sensitivity. In practice, the optimal point has to be determined by the operator [69]. In addition, the laser power going to the probe beam and the reference beam have to be controlled, so that when the two combines in the return path, the power intensities of the two signals are comparable. Failure to carry out the calibrations would compromise the usefulness of the technique.

In 2007, a research group in Japan developed a frontside thermoreflectance system that incorporates Michelson-type interferometer in the optics as shown in Figure 3.13. This setup is very similar to those developed for LVP measurements as shown in Figure 3.12.

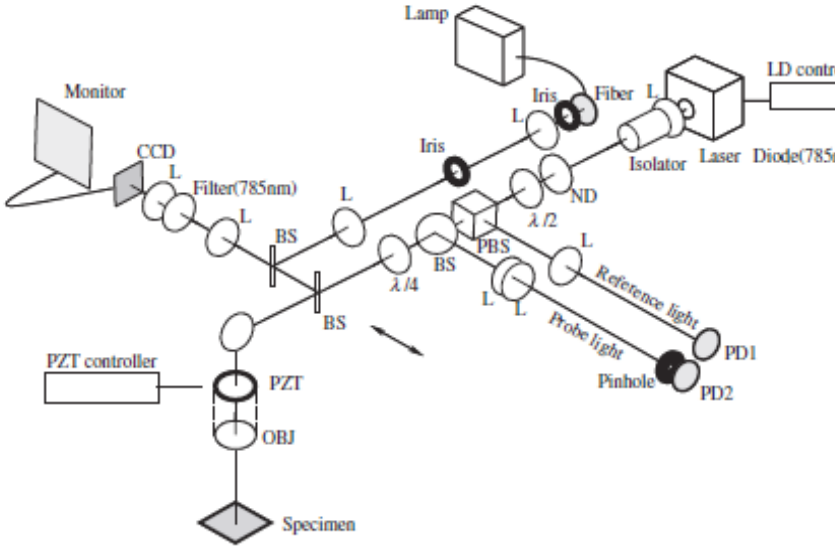

Fig 3.13: Interferometric thermoreflectance setup [82]

The interferometer detects phase modulation due to temperature variation of the sample surface which is converted to amplitude modulation at the PBS and detected by the photon detector. As mentioned earlier, such a setup requires path-length and power matching of the probe arm and reference arm, which has to be determined operationally.

3.3 Spatial Resolution

Depending on the optical system and device to measure, there are various spatial resolution definitions which may be used. First and foremost, in an imaging microscopy system with diffraction limited optics, the minimum achievable spot size is defined as the minimum resolvable spatial resolution R as [68]:

$$R = \frac{1.03\lambda f_L}{D} \tag{3.1}$$

where λ is the wavelength of the light source, f_L is the focal length and D is the pupil diameter of the objective lens.

The wavelength and the numerical aperture of the objective lens affect the image resolution. In terms of the objective lens NA, the full-width-half-maximum (FWHM) of the optical spot is given by [23]:

$$R = \frac{\lambda\sqrt{1-NA^2}}{2NA} \tag{3.2}$$

An alternative and more commonly used definition is that of the circular Airy diffraction image with a central bright disk and progressively weaker concentric dark and bright rings, instead of considering the point spot as being infinitely small. In this case, the Airy disk resolution is defined as [66]:

$$R = \frac{1.22\lambda}{NA} \tag{3.3}$$

For two points, the Rayleigh's Criterion may be used which states that two neighboring point sources are distinguishable from each other if the maximum response to one is located at the first zero of response to the second point. On this basis, the minimum resolvable spatial resolution R becomes [83]:

$$R = \frac{0.61\lambda}{NA} \tag{3.4}$$

The criteria specified in Eqs. 3.3 and 3.4 are defined for non-confocal microscopy systems with incoherent light source. If coherent light source is used, the spatial resolution would depend on its incident polarization, and may degrade by up to 34% [68]. In the case of confocal microscopy systems, better spatial resolutions are achieved. Using the Rayleigh Criterion, the improvement is calculated to be 7.3% [68]. If the FWHM of a point spot is used, an improvement of about 41% is achieved for the spatial resolution [84].

The determination of an absolute and authoritative spatial resolution value is difficult. It depends on the selected resolution criteria, the type of optical system, the objective lens and the coherence of the light source. In practice, conventional high NA optics have been used to achieve spot sizes of 1-2 μm [85]. If higher spatial resolution is desired, the use of Si solid immersion lens (SIL) on the Si

substrate for backside probing enhances the effective spatial resolution to 200-250nm [83].

3.4 Telecentricity and Sample Tilt

The microscope objective lenses used may or may not be corrected for telecentricity. This section discusses about telecentricity and the impact of sample tilt for a telecentric system. In scanning confocal microscopy systems, the microscope objective lenses are corrected telecentrically [66]. A telecentric system is space invariant and linear, ensuring constant magnification factor, as shown in Figure 3.14.

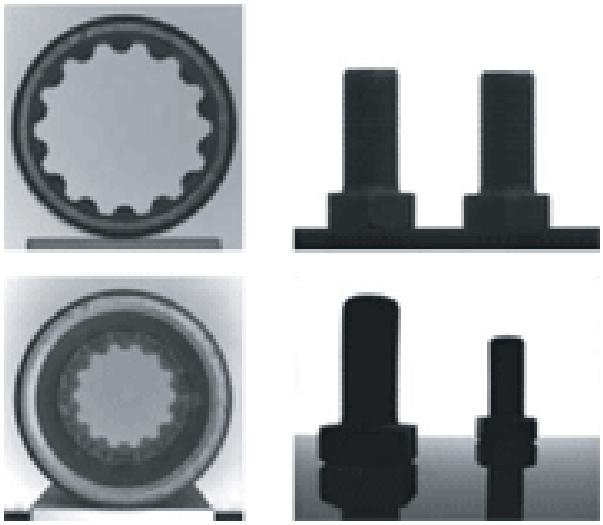

Fig. 3.14: Comparison of (top) telecentric lens (bottom) ordinary lens [86]

The image on the left is an internal spline on a cylindrical object, and the image on the right shows two identical machine screws. As expected, in a telecentric system, constant magnification such that all equally sized objects have the same

image size is observed in the top images. In a non-telecentric system, as shown by the bottom images, different sizes are observed. Figure 3.15 illustrates the ray diagram of a telecentric system.

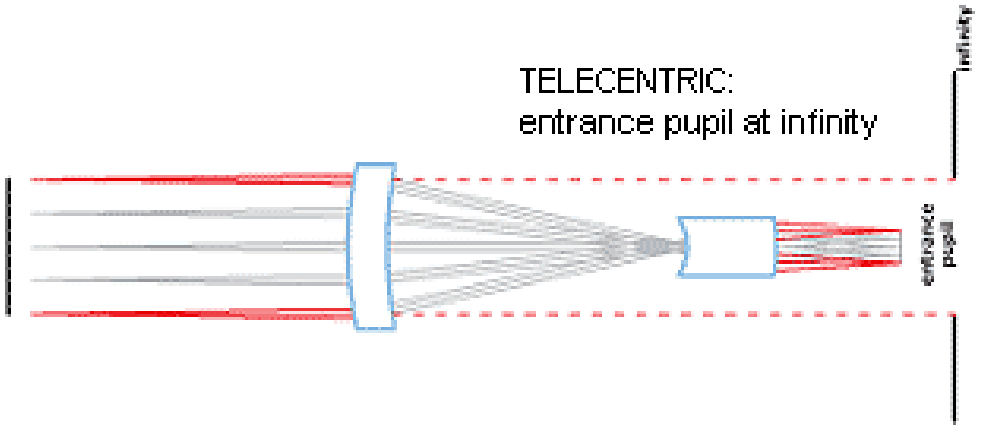

Fig. 3.15: Telecentric system ray diagram [86]

From the ray diagram, it is expected that a telecentric system would only ensure constant magnification when the DUT is aligned with the object plane. If the DUT is tilted, image distortion would result.

3.5 Summary

The development of systems and their applications of reflectance modulation based on electro-optical and temperature effects have, in general, taken very divergent paths. Reflection modulation based on electro-optical effects has been applied to timing measurements of electrical signals on integrated circuits. Reflectance modulation based on temperature effects has been applied to the

measurement of material properties, thin film thickness and temperature determination.

For resistive elements, reflectance modulation due to temperature effects is dominant. For active devices, such as MOS transistor and PN junctions, the interplay between electric field and Joule heating depends on the electrical bias and the resultant current. As such, it is difficult to fully isolate the electro-optical effects from thermal effects.

Interestingly, Figures 3.12 and 3.13 show that the setup may be similar for both reflectance modulation studies on electro-optical and temperature effects. Most of the reflectance modulation systems and studies are frontside-based. There are opportunities in developing an integrated system that is capable of both timing and temperature measurements. In addition, there are opportunities for fundamental research in backside-based reflectance modulation techniques.

Chapter 4 Models and Hypothesis

In this chapter, reflected laser beam models are developed for frontside and backside techniques. The reflectance modulations due to changes in temperature for various impurity doping concentrations are computed and analyzed for both frontside and backside models. The frontside and backside reflectance modulations due to changes in electric field and free carrier density are presented. Hypotheses are stated for the backside laser reflectance modulations due to the variations in temperature, electric field and free carrier density.

4.1 General Laser Beam Propagation

A generic laser beam propagation model is presented in Figure 4.1. The material is passivated for the frontside model, and Si for the backside model. For simplicity of the illustration, aluminium (Al) metal line is selected as the probed device. The incident laser intensity is I_0. It is assumed that the intensity loss in air is negligible. It is further assumed that the incident ray and all the reflected and transmitted rays are normal to the interface, i.e. at perpendicular incidence.

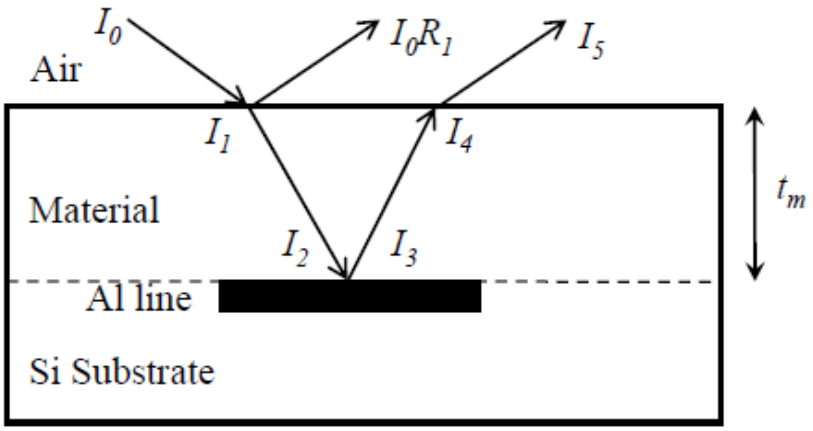

Fig. 4.1: Reflected laser beam model

At the Air-Material interface, the transmitted light I_1 is given by:

$$I_1 = I_0.(1 - R_1) = T_1 I_0 \tag{4.1}$$

where R_1 is the reflectance of the interface and T_1 is the transmittance between the two media. The intensity of the reflected light is I_0R_1.

For perpendicular incidence, the reflectance R and transmittance T_r from Fresnel equations [36] simplify to:

$$R = \left(\frac{n_t - n_i}{n_t + n_i}\right)^2 \tag{4.2}$$

$$T_r = \left(\frac{4.n_t.n_i}{n_t + n_i}\right)^2 \tag{4.3}$$

where n_t and n_i are the refractive indices of incident and transmitting medium respectively.

The transmitted light propagates through the material of thickness t_m and the intensity attenuation follows Lambert's Law [37] such that at the Material-Al interface, the light intensity I_2 is given by:

$$I_2 = I_0.(1-R_1).e^{-\alpha t_m} \tag{4.4}$$

where α is the absorption coefficient of the material.

The reflected light I_3 is given by:

$$I_3 = I_0.(1-R_1).R_2.e^{-\alpha t_m} \tag{4.5}$$

where R_2 is the reflectance of the Material-Al interface.

The reflected light I_3 propagates again through the material and the resulting intensity I_4 at the Material-Air interface is:

$$I_4 = I_0.(1-R_1).R_2.e^{-2\alpha t_m} \tag{4.6}$$

The reflectance R_3 at the Material-Air interface is the same as that for the reflectance R_1 at the Air-Material interface for perpendicular incidence. The resultant transmitted light I_5 is:

$$I_5 = I_0.(1-R_1)^2.R_2.e^{-2\alpha t_m} \tag{4.7}$$

Neglecting subsequent reflections due to the reflected beam of I_4 at the Material-Air interface, the total light intensity I_t that is measured by the photon detector is the sum of surface and device reflections given by:

$$I_t = I_0.R_1 + I_0.(1-R_1)^2.R_2.e^{-2\alpha t_m} \quad (4.8)$$

The reflected light intensity depends on the reflectance which is determined by the refractive indices of the media at the interface, the absorption coefficient and the substrate thickness. In Chapter 3, frontside and backside reflectance techniques have been reported. Based on Eq. 4.8, the frontside and backside reflectance models are presented in the next two sections.

4.2 Frontside Reflectance Model

The metal lines used in integrated circuits are typically gold (Au), aluminium (Al) or copper (Cu). A passivation layer of oxide with typical thickness less than 1 μm is used to protect the surface metals from elements of corrosion. As discussed in Section 3.2.2, the calibration of the passivation thickness is needed to accurately determine the temperature variation from the reflectance modulations.

The focus of this reflectance work is for backside analysis, and the frontside model is developed mainly for comparison. Simplicity in its computation without gross error is preferred. Since the passivation thickness is less than 1 μm, the effects due to the absorption coefficients are not significant, and will be ignored in

the simplified frontside model. Simplifying Eq. 4.8, the total light I_f that is measured by the photon detector is:

$$I_f = I_0.R_1 + I_0.(1-R_1)^2.R_2 \qquad (4.9)$$

The detected reflected intensity is dependent on R_1 and R_2. Strong surface reflection is an issue in frontside measurements [64].

4.3 Backside Reflectance Model

The material is Si for the backside model. Typical wafer substrate thickness t_s is 800 µm. For the backside analyses, a die needs to be backside prepared and t_s needs to be thinned to the range of 100 to 500 µm depending on its impurity doping concentrations [17]. Eq. 4.8 is valid for most CCD-based systems [87] and laser scanning microscopy systems [34] used for backside measurements, with the exception of laser-scanning confocal microscopes [66]. In the latter case, the surface reflectance can be neglected as the objective lenses are corrected telecentrically. So, the total light intensity I_b measured by a laser-scanning confocal microscopy system can be represented as:

$$I_b = I_0.(1-R_1)^2.R_2.e^{-2\alpha t_s} \qquad (4.10)$$

The refractive index of the media, the substrate thickness and the absorption coefficient affect the detected laser intensity. The substrate thickness determines the propagation path in the substrate, and hence the amount of absorption. In Chapter 2, the variation of the absorption coefficient and refractive index due to changes in the temperature, electric field and free carrier concentration has been discussed. The following sections analyze the reflectance modulations based on the frontside and backside models due to the parameters for an incident laser wavelength of 1.34 μm.

4.4 Reflectance Modulation due to Changes in Temperature

The variation of the absorption coefficient and refractive index of Si with temperature is studied. The absorption coefficient values over the temperature range from 300 to 400 K are simulated using Eq. 2.3 for assumed free carrier concentration of 10^{16} cm^{-3} at a peak laser irradiance of 1 $mW \cdot \mu m^{-2}$ (equivalent to 0.1 $MW \cdot cm^{-2}$), with the refractive index of Si equal to 3.5174 at room temperature, giving Si surface transmittance of 0.69.

From Eq. 2.4, the thermal model for the refractive index of Si proposed by GE Jellison and FA Modine [51] is converted to the temperature scale of Kelvin and simplified for the specific case where the incident laser wavelength is 1.34 μm as:

$$n_{Si}(T) \approx \sqrt{11.9104 + 0.001538T} \qquad (4.11)$$

where T is the temperature of the Si substrate in Kelvin.

The refractive indices of air and Al are assumed constant at values of 1.0 and 1.36964 respectively [88]. The refractive indices of Si over the temperature range from 300 to 400 K are simulated using Eq. 4.11. Using Eq. 4.2, the R_1 and R_2 values are calculated which correspond to the reflectances of the Air-Si interface and Si-Al interface respectively. Figure 4.2 shows the simulated variation of R_1, R_2 and α over the temperature range from 300 to 400 K at a wavelength of 1.32µm.

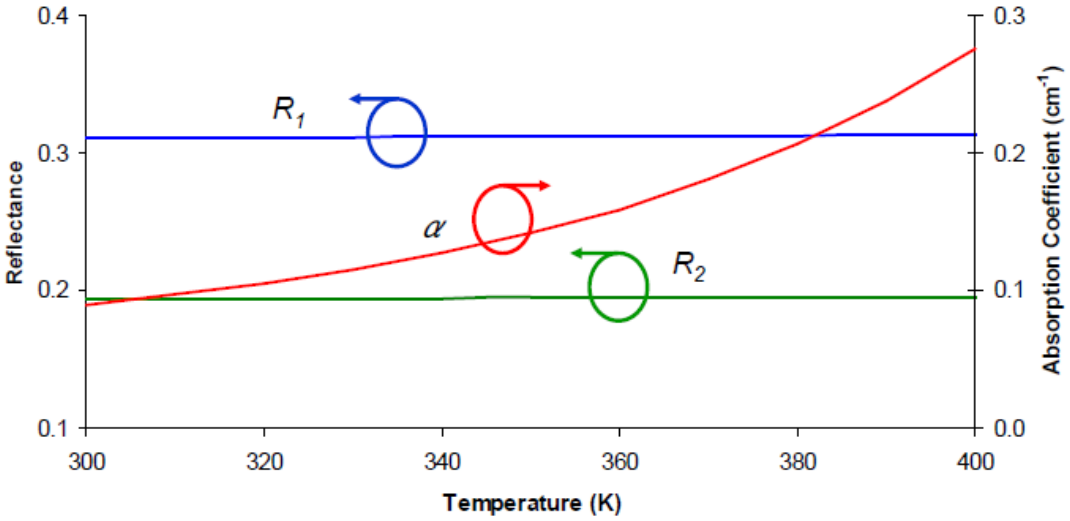

Fig. 4.2: Variation of R_1, R_2 and α with temperature

From the graph, the absorption coefficient is about 0.089 at 300 K. If the temperature increases to 400 K, the absorption coefficient increases to 0.275, equivalent to an increase of 207%. It is observed the absorption coefficient increase non-linearly with the temperature rise. At 300K, R_1 and R_2 are 0.3105 and 0.1931 respectively. If the temperature increases to 400 K, R_1 and R_2

increase to 0.3129 and 0.1953 respectively, corresponding to less than 1.2% increase in value. The absorption coefficient is expected to be the dominant factor in the laser reflectance modulations.

Based on Eq. 4.10, the magnitude of the absorption coefficient affects its effects on the reflected intensity. Based on the Drude model and discussed in Section 2.1.2, the impurity doping concentration N_{doped} has a linear relation with the absorption coefficient due to impurity and lattice scattering. Empirical data for n-doped and p-doped Si at different impurity doping concentrations support this relationship as shown in Figures 4.3 and 4.4 respectively [17, 41-44]. The figures show that each decade increase in doping concentration (either n-type or p-type doped) results in a decade increase in the magnitude of the absorption coefficient.

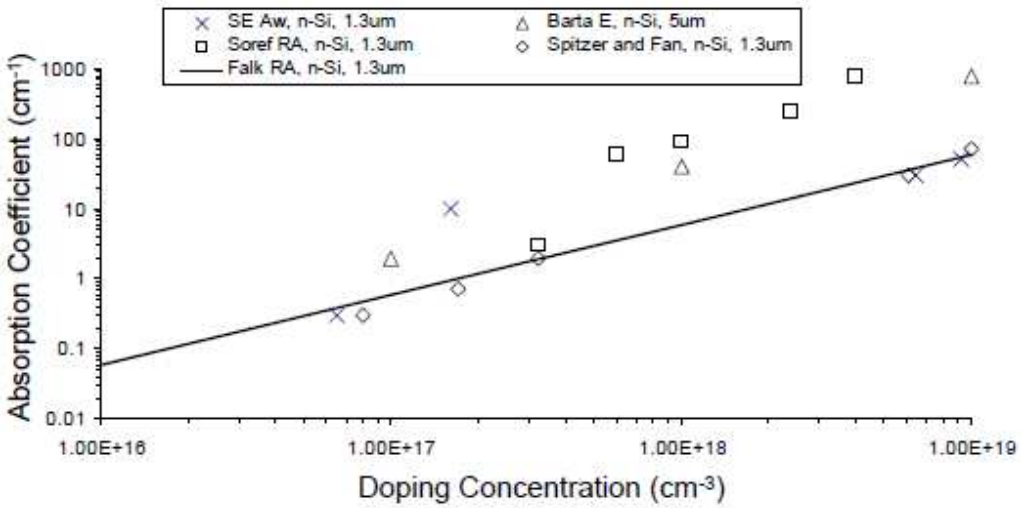

Fig. 4.3: Absorption coefficient of n-doped Si at various doping concentrations

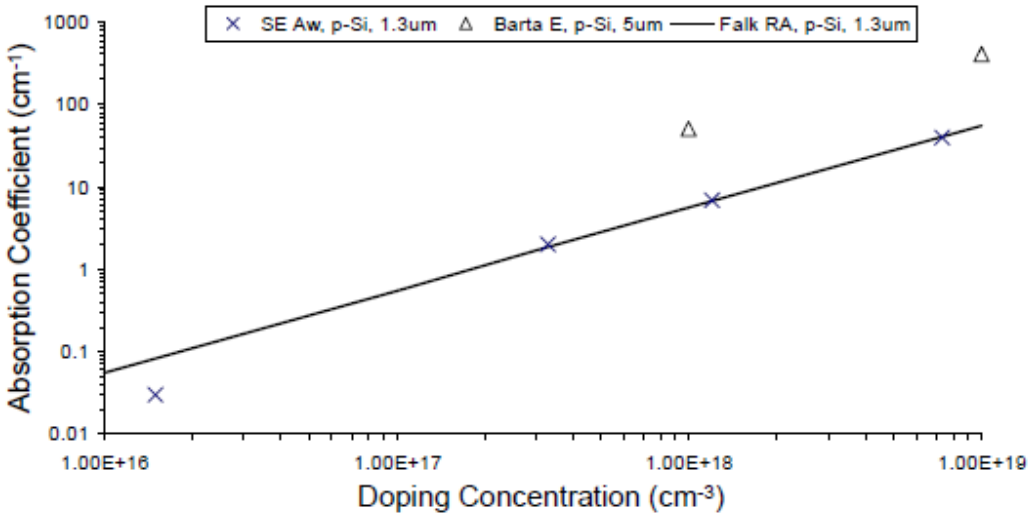

Fig. 4.4: Absorption coefficient of p-doped Si at various doping concentrations

The absorption models proposed by RA Falk [41] correlates well with earlier empirical data presented by Aw [17], Barta [43], Soref [44] and Spitzer [42] in the determining of the absorption coefficient for n-type and p-type doped Si at various doping concentrations, and strengthens the hypothesis that free-carrier absorption is the primary mechanism at the incident wavelength of 1.34 µm.

For typical reflectance techniques, the probed laser beam intensities are kept low to mitigate its invasiveness, with irradiance less than 1 MW·cm^{-2}. In addition, microelectronic devices do not typically operate beyond 400 K. Incorporating the effect of the impurity doping concentration, the thermal model for the absorption coefficient proposed by PJ Chernek and JA Orson [45] is modified as:

$$\alpha\left(N_{doped},T\right)\approx\left[0.0075\left(\frac{N_{doped}}{10^{15}}\right)+\left(1-R\right)I_0\beta_{2P}-\gamma\right]\left(\frac{T}{T_0}\right)+\gamma\left(\frac{T}{T_0}\right)^9 \quad (4.12)$$

where T is the temperature of the Si substrate in Kelvin, and T_0 is 300 K and N_{doped} is larger than 10^{12} cm^{-3}.

Based on Eqs. 4.11 and 4.12, the effects of N_{doped} and T are incorporated into the backside model of Eq. 4.10. The reflected intensity over the temperature variation of 300K to 400K are computed for impurity doping concentrations of 10^{14} cm^{-3}, 10^{16} cm^{-3} and 10^{18} cm^{-3} respectively.

4.4.1 Impurity Doping Concentration of 10^{14} cm^{-3}

The reflectance modulation is the ratio of the change in the reflected intensity at the higher temperature to the reflected intensity at the reference temperature of 300K. Figure 4.5 plots the reflectance modulations over the temperature range from 300K to 400K for an impurity doping concentration of 10^{14} cm^{-3}.

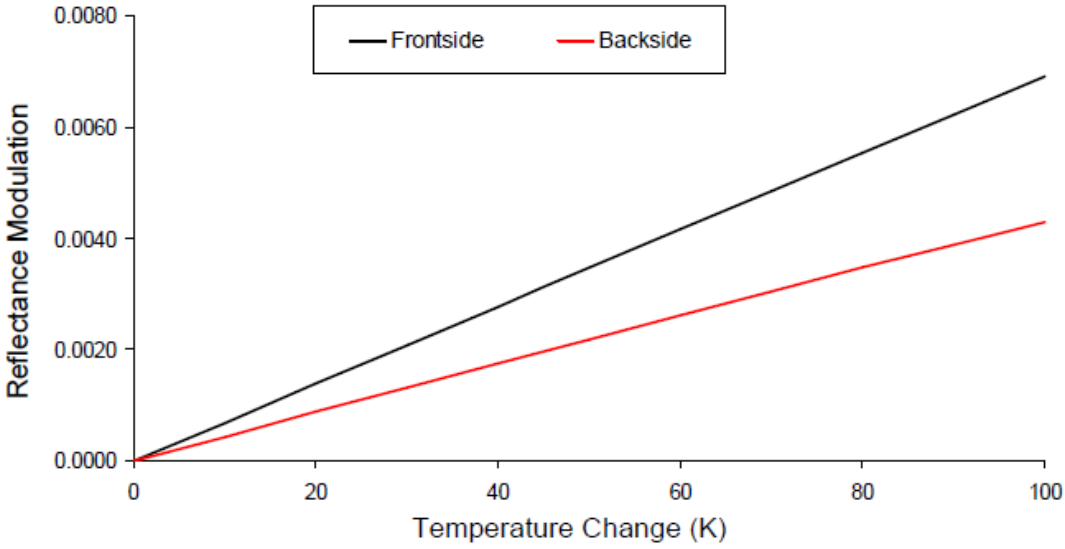

Fig. 4.5: Variation of R_1, R_2 and α with temperature at impurity doping concentration of 10^{14} cm^{-3}

When the temperature increases from 300 to 400 K, the reflectance modulations of both frontside and backside models are positive as the substrate absorption is negligible, and increase with temperature. The reflectance modulations of the frontside model are generally larger than the backside model due to the additional surface reflection. At a temperature change of 100 K, the reflectance modulation based on the frontside model is 0.0069, and the reflectance modulation based on the backside model is 0.0043. The backside reflectance model highlights the reflectance modulations are positive when the modulations of the reflected intensity are primarily due to the temperature variation of the reflectance.

4.4.2 Impurity Doping Concentration of 10^{16} cm^{-3}

Figure 4.6 plots the reflectance modulations over the temperature range from 300 to 400 K for an impurity doping concentration of 10^{16} cm^{-3}.

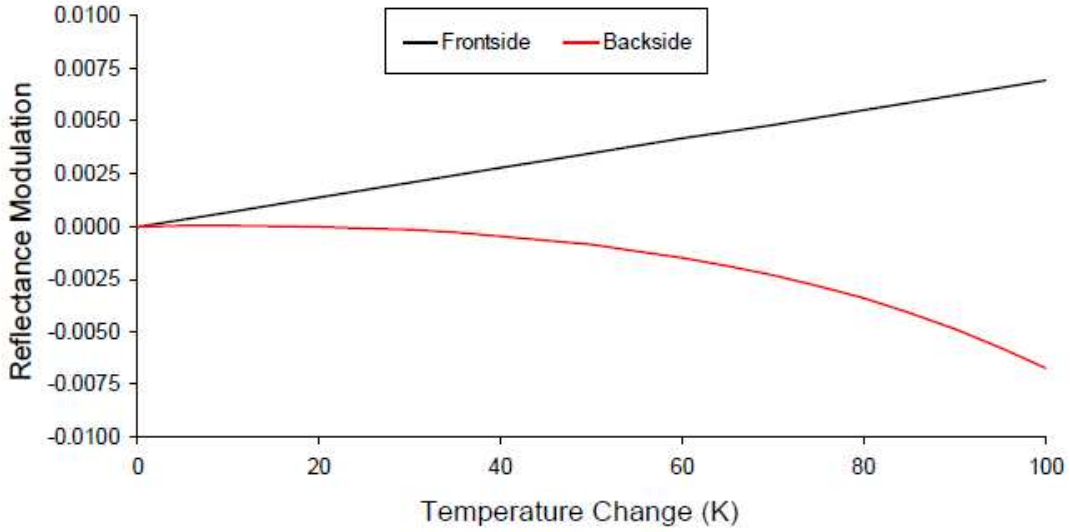

Fig. 4.6: Variation of R_1, R_2 and α with temperature at impurity doping concentration of 10^{16} cm^{-3}

As the temperature increases from 300 to 400 K, the reflectance modulations of the frontside model are identical to Figure 4.5. At the increased impurity doping concentration 10^{16} cm^{-3}, the reflectance modulations of the backside model are negative due to substrate absorption and increase non-linearly with temperature. At a temperature change of 100K, the reflectance modulation based on the frontside model is 0.0069, and the reflectance modulation based on the backside model is -0.0067. The backside reflectance model highlights the reflectance modulations are negative when the modulations of the reflected intensity are primarily due to the temperature variation of the absorption coefficient.

4.4.3 Impurity Doping Concentration of 10^{18} cm^{-3}

Figure 4.7 plots the reflectance modulations over the temperature range from 300 to 400 K for an impurity doping concentration of 10^{18} cm^{-3}.

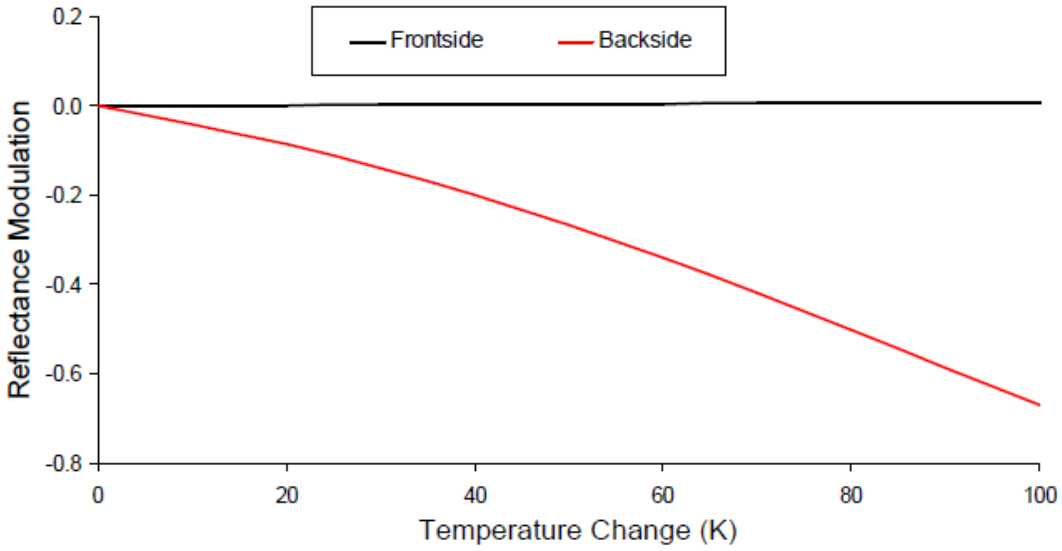

Fig. 4.7: Variation of R_1, R_2 and α with temperature at impurity doping concentration of 10^{18} cm^{-3}

As the temperature increases from 300 to 400 K, the reflectance modulations of the frontside model are the same as Figures 4.5 and 4.6. The reflectance modulations of the backside model are negative and much larger than the frontside model due to significant substrate absorption. At a temperature change of 100 K, the reflectance modulation based on the frontside model is 0.0069, and the reflectance modulation based on the backside model is -0.6701. In this case, the backside reflectance modulations are one to two orders of magnitude larger. This analysis shows that backside reflectance modulation techniques can

achieve better sensitivity compared to frontside modulation techniques for temperature measurements.

4.5 Reflectance Modulation due to Changes in Electric Field

The effects of electroabsorption and electrorefraction have been discussed in Chapter 2. Empirical data suggests that electroabsorption is negligible when the laser beam is 1.34 µm wavelength [44, 49]. In the following analysis, the effects due to electroabsorption are neglected. From Figure 2.4, the refractive index of Si is observed to increase by 0.5×10^{-6}, 2×10^{-6} and 3×10^{-6} at the applied electric field of 75, 85 and 100 $kV \cdot cm^{-1}$ respectively. The corresponding reflectance modulations of the frontside and backside models are computed and presented in Table 4.1. In the analysis, it is assumed the laser wavelength is 1.34 µm, the laser intensity is 1.0 $mW \cdot \mu m^{-2}$, substrate doping concentration is 10^{16} cm^{-3}, substrate thickness is 300 µm and the substrate temperature remains constant at 300 K.

Table 4.1: Reflectance modulations due to electrorefraction

E ($kV.cm^{-1}$)	Δn_{Si} (10^{-6})	$\frac{\Delta I_f}{I_{t0}}$ (10^{-6})	$\frac{\Delta I_b}{I_{t0}}$ (10^{-6})
75	0.5	0.15914	0.10255
85	2	0.63655	0.41019
100	3	0.95483	0.61528

In Table 4.1, the first column is the applied electric field. The second column provides extracted values from Figure 2.4 for the change in refractive index to the applied electric field. The third column computes the reflectance modulations for the frontside model. The fourth column computes the reflectance modulations for the backside model. It is observed that the reflectance modulations are positive at the applied electric field. The values calculated using the frontside and backside models do not differ significantly. Compared to the reflectance modulations due to the temperature effect, the reflectance modulations due to electric field effect are observed to be significantly weaker.

4.6 Reflectance Modulation due to Changes in Free Carrier Density

The changes in refractive index and absorption coefficient due to changes in the free carrier density have been discussed in Chapter 2. This section explores reflectance modulation due to variation in free electron and free hole densities. Tables 4.2 and 4.3 tabulate the changes in refractive index and absorption coefficient for variation in free electron and free hole densities respectively [44].

Table 4.2: Changes in refractive index and absorption coefficient due to variation in free electron density [44]

ΔN_e (cm^{-3})	Δn_{Si} (10^{-6})	$\Delta \alpha_{Si}$ (cm^{-1})
10^{16}	-6	0.04
10^{17}	-60	0.4
10^{18}	-600	4

Table 4.3: Changes in refractive index and absorption coefficient due to variation in free hole density [44]

ΔN_h (cm^{-3})	Δn_{Si} (10^{-6})	$\Delta \alpha_{Si}$ (cm^{-1})
10^{16}	-125	0.03
10^{17}	-300	0.3
10^{18}	-1500	3

Each decade increase in the free electron density leads to a corresponding decade increase in the magnitude for the change in the absorption coefficient and refractive index. The same trend is observed for the change in the absorption coefficient for variation in the free hole density. A smaller rate of change is observed for the change in the refractive index for variation in the free hole density. The reflectance modulations based on the frontside and backside models are computed and tabulated in Tables 4.4 and 4.5, showing the reflectance modulations due to variations in free electron density and free hole density respectively. The impurity doping concentration of the substrate is assumed to be 10^{16} cm^{-3}.

Table 4.4: Reflectance modulation due to variation in free electron density

ΔN_e (cm^{-3})	$\frac{\Delta I_f}{I_{t0}}$ (10^{-3})	$\frac{\Delta I_b}{I_{t0}}$ (10^{-3})
10^{16}	-0.0019	-2.40
10^{17}	-0.0191	-23.73
10^{18}	-0.1910	-213.47

Table 4.5: Reflectance modulation due to variation in free hole density

ΔN_h (cm^{-3})	$\frac{\Delta I_f}{I_{t0}}$ (10^{-3})	$\frac{\Delta I_b}{I_{t0}}$ (10^{-3})
10^{16}	-0.0040	-1.82
10^{17}	-0.0955	-17.90
10^{18}	-0.4776	-164.99

In Tables 4.4 and 4.5, the first column shows the variation in the free carrier density. In the second column, the computed reflectance modulation is based on the frontside model. In the third column, the computed reflectance modulation is based on the backside model.

For both frontside and backside models, the reflectance modulations are negative with increase in free carrier density. For each variation in free carrier density, the reflectance modulations for the backside model are larger than the reflectance modulations for the frontside model by 2 to 3 orders of magnitude. This indicated that the reflectance modulation due to free carrier density variation is primarily due to the change in the absorption coefficient, and that backside reflectance modulation techniques can achieve better sensitivity compared to frontside modulation techniques for measurements of electro-optical effects.

4.7 Reflectance Modulation Hypotheses

The reflected intensity of a laser beam is modulated due to changes in the refractive index and the absorption coefficient as a result of variations in the temperature, electric field and free carrier concentrations as discussed in the earlier sections of this chapter.

Typical substrate doping ranges from 10^{15} to 10^{16} cm^{-3} [89]. Backside reflectance modulations due to temperature effect for microelectronic devices are expected to be negative. The sensitivity of the backside technique is expected to be comparable or better than the frontside technique. A study on backside reflectance modulation due to temperature effect of metal thin films concluded the peak reflectance modulation resulted from maximum temperature change of the device [90].

In the normal operation of an MOS transistor as a part of a VLSI circuit, the device constantly switches from inversion to saturation and then switches back. The pinch-off region is depleted of free carriers [53], has high electric field [56], and is the most resistive section of the channel [55], with corresponding heat dissipation profile that peaks in the pinch-off region [57]. As such, the variations in the temperature, electric field and free carrier density of the pinch-off region in the channel of an MOS transistor are expected to result in significant reflectance modulations. The magnitude of the reflectance modulation is expected to correlate with the length of the pinch-off region.

It should be highlighted that the discontinuity in free carrier density along the channel is apparent at the pinch-off point which acts as the boundary between two distinct regions: pinch-off region and the source section of the channel. In fact, the Reddi-Sah model [55] predicted discontinuity in the electric field at the pinch-off point [58, 91]. Subsequent analytical models have evolved and assumed electric field continuity at the pinch-off point. This is generally achieved with analytical solution of the electric field E_S at the pinch-off point for the source section [91]. E_S is then applied as the boundary condition for the pinch-off region with the assumption of electric field continuity at the pinch-off point [60]. Backside reflectance modulations along the channel should give new insights into these assumptions.

Chapter 5 Experimental Setup and Measurement Methods

This chapter describes the experimental setup that is used for the laser reflectance modulation measurements. The coherence and incident laser power of the laser source are studied. The achievable spatial resolution of the system is discussed. A study is conducted on the impact of sample tilt on the system which is telecentric. The measurement methods are described, which include static and dynamic techniques.

5.1 Experimental Setup

The optical setup is shown in Figure 5.1. It is a laser scanning confocal microscopy system based on the first confocal microscopy system invented by Marvin Minsky at Harvard University in 1957 [67].

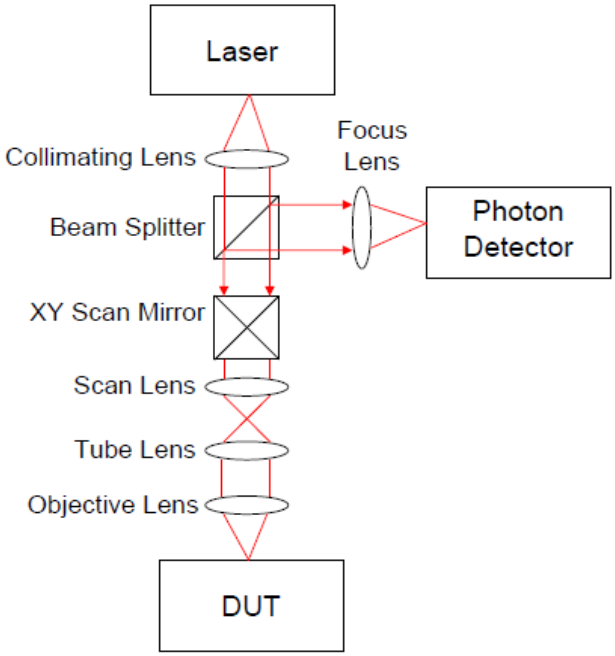

Fig. 5.1: SEMICAPS SOM1100 optical setup

The laser source is at 1.34 µm wavelength. The collimating lens ensures parallel rays enter the optical setup. The XY scan mirror is made up of a pair of motorized mirrors that scan the laser beam in the X and Y directions. The laser beam is focused at the probed area of the DUT. The reflected beam travels back through the same optical path, and get reflected at the beam splitter to the photon detector.

There are five selectable objective lenses at magnification powers of 5x, 10x, 20x, 50x and 100x. The lenses are housed in a light-tight turret and sit on a vibration isolation table. The optical setup is motorized in the X, Y and Z axes to provide full navigation around the device and effective focusing with different objectives. The field of view is 3.6 mm x 3.6 mm for 5x objective lens and 0.09 mm x 0.09

mm for 100x objective lens. The experiments are done with the 50x objective lens, which has an effective field of view at 130 µm x 130 µm. Each frame is made up of 512 pixels x 512 pixels.

The DUT stage sits on the vibration isolation table. A vacuum suction system is implemented to lock the DUT during testing. The SEMICAPS SOM1100 has all the functionalities illustrated in Figure 5.1, and is used for the experiments.

5.2 Laser Coherence

The use of coherent laser source typically causes interference fringes in the reflected light of the optical surfaces [66]. It occurs when the rays at the detector has different optical path lengths, and the superposition of the waves have resultant maxima and minima points [36].

A monochromatic coherent laser source at 1.34 µm wavelength is used to capture a reflected image of a backside prepared Vishay VSSR 1603 trimmed resistive structure at a substrate thickness of 300 µm, as shown in Figure 5.2a. The reflected intensity across KK' is plotted in Figure 5.2b. Interference fringes are observed as small ripples riding on the resistive surface. For backside techniques, the interference fringes are more severe than frontside techniques [92].

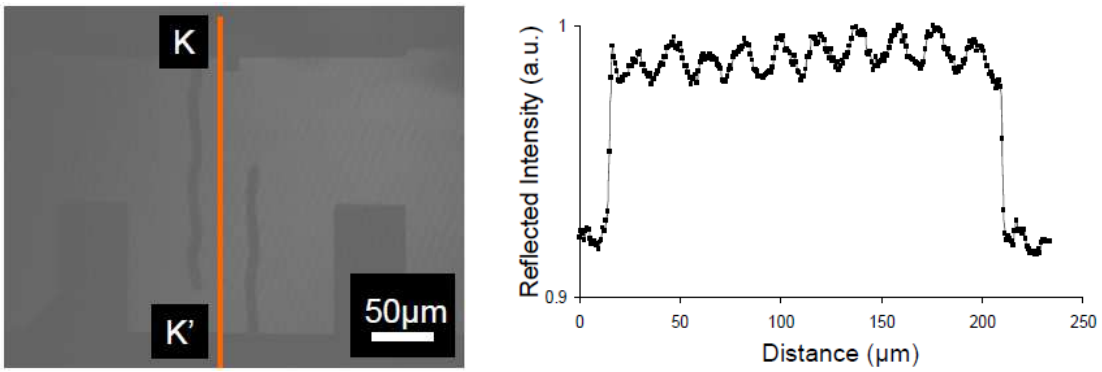

(a) (b)

Fig. 5.2: (a) Backside laser-scanned image using coherent 1340 nm laser source, and (b) reflected intensity across KK'

The fringe patterns are inherent in the signal and depend on the sample and the optical setup. It is possible to reduce the visible effects of the fringe patterns with system gain adjustments. In typical reflected imaging and laser-induced measurements which are qualitative, the fringe patterns are not a problem to the relevant techniques. However, the interference fringe is an issue for laser reflectance modulation techniques, as these techniques are based on detection of reflectance modulation [64] with magnitudes much smaller than the fringe patterns.

The same experiment was conducted using a monochromatic non-coherent light source at 1.34 µm wavelength. Compared to the coherent laser source, the incident beam of the non-coherent light source is not polarized. The same device as shown in Figure 5.2a is used. The reflected intensity across KK' is plotted in Figure 5.3. The ripples that were observed in Figure 5.2b are not observed. The reflected intensity is observed to be monotonically decreasing across the

resistive structure which was not observed in Figure 5.2b. This was due to sample tilt which is discussed in Section 3.4 and studied in a later section. The non-coherent 1.34 µm light source is used for all the reflectance measurements in this thesis.

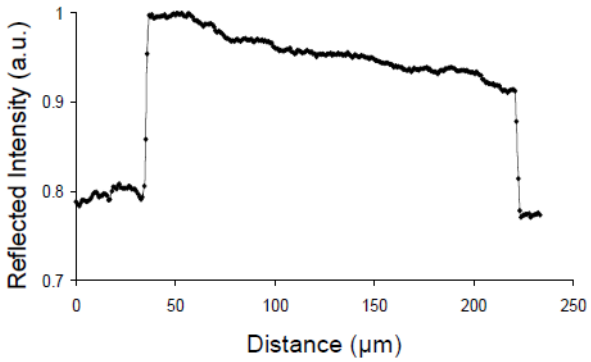

Fig. 5.3: Reflected intensity across KK' using a non-coherent 1.34 µm light source

5.3 Probe Beam Power

In the review of the reflectance modulation systems and techniques, it is possible to see differing trends of the probe beam power on the DUT for temperature effect and electro-optical effect. For the reflectance modulation due to temperature effect, a consistent trend of decreasing probe beam power is observed. In the 1980s, the incident power of the probe beam on the DUT is approximately 2 $mW \cdot \mu m^{-2}$ [73]. In the late 1990s, this has decreased to less than 1 $mW.\mu m^{-2}$ [34]. This is to ensure the free carrier absorption mechanism for temperature variation is dominant in the reflectance modulations as discussed in Eq. 2.3 and Figure 4.2.

Interestingly, the probe beam power was hardly mentioned in the literatures for the development of laser reflectance modulation based on electro-optical effects. In fact, the LTP system in SEMICAPS typically uses higher probe beam power [93]. At a higher probe beam power, the system can detect smaller fluctuations in the charge density of an active device [23].

A study was conducted to determine the probe beam power of the non-coherent 1.34 µm light source which can be tuned by varying its supply current in the range of 150 to 500 mA. A power meter is used for single point measurements at 50x magnification objective lens as the supply current of the non-coherent light source is varied from 150 to 500 mA, as shown in Figure 5.4.

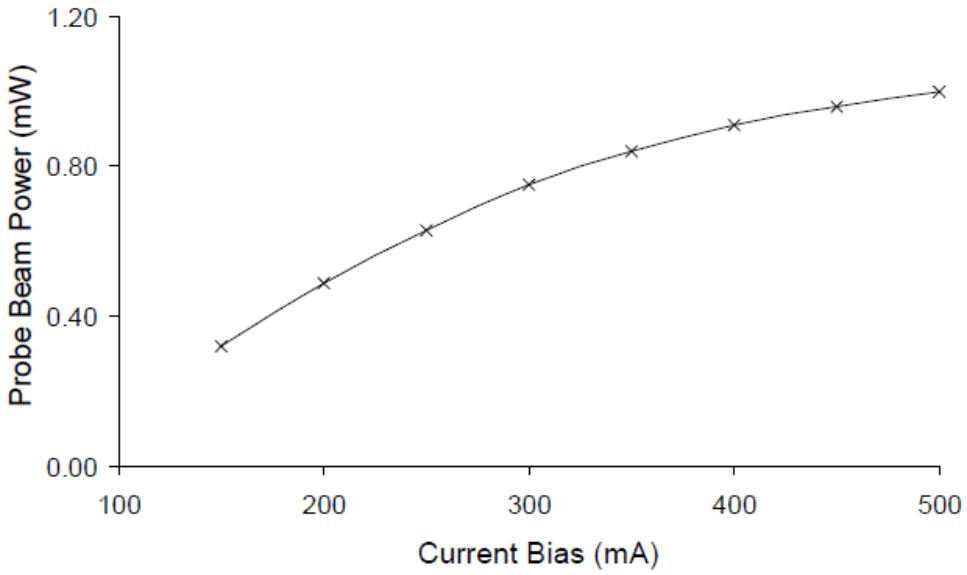

Fig. 5.4: Probe beam power versus supply current

A backside-prepared resistive metal thin film is used to study the sensitivity of the reflectance modulation at a current bias of 150, 250 and 500 mA for the non-coherent light source. For each current bias, different electrical biases are applied to the resistive sample, as shown in Figure 5.5. The Si substrate of the sample is 100 µm.

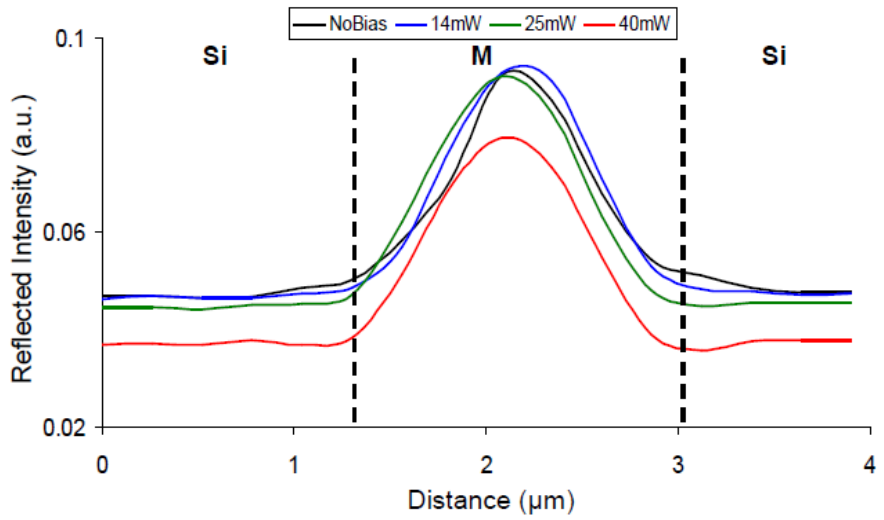

(a)

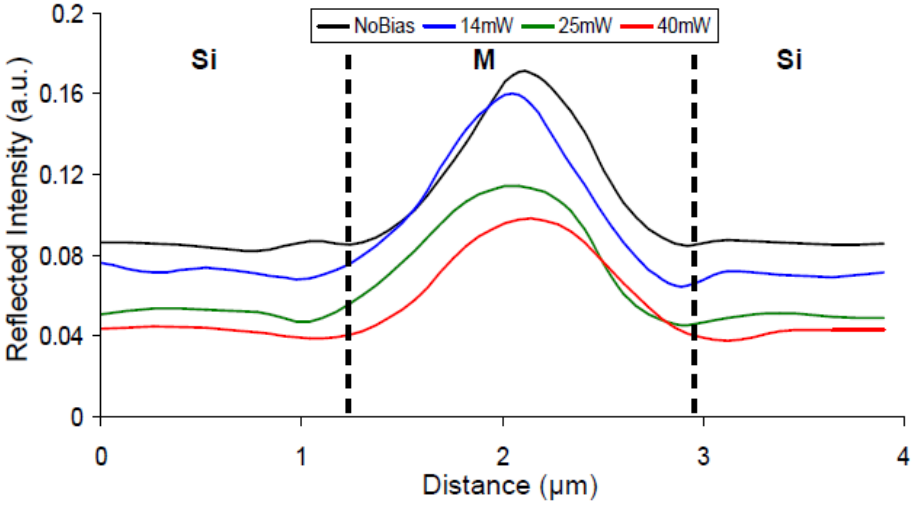

(b)

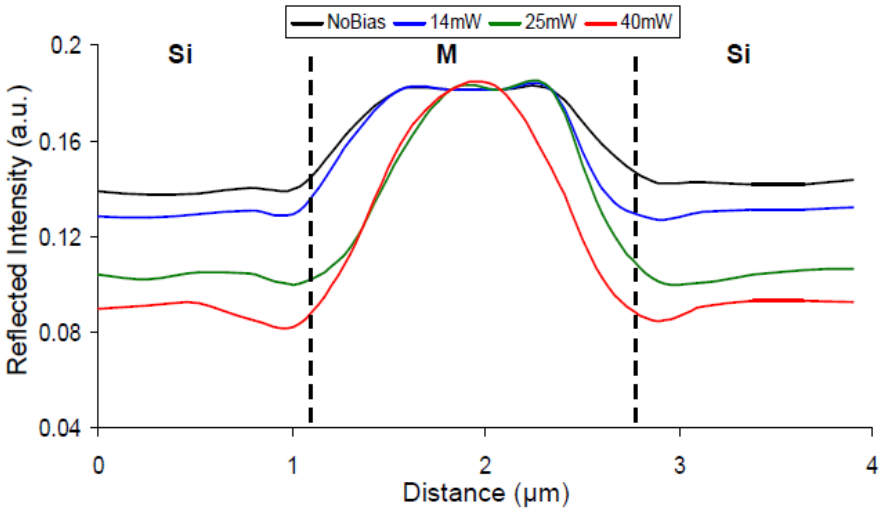

(c)

Fig. 5.5: Current bias is (a) 150 mA, (b) 250 mA, and (c) 500 mA

In Fig 5.5a, the current bias is 150 mA. The reflected intensities at 14 mW and 25mW electrical bias can hardly be resolved from the reflected intensities at no electrical bias. The sensitivity of the reflectance modulation is thus poor. In Figure 5.5b, the current bias is 250 mA. The reflected intensities at 14 mW and 25 mW can clearly be resolved. The sensitivity of the reflectance modulation at this current bias is good. In Figure 5.5c, the current bias is 500 mA. Due to stronger probe beam power, the reflected intensities of the metal line at an electrical bias of 14 and 25 mW saturate and cannot be resolved. The system gain of the photon detector can be reduced to prevent metal line saturation. However, since the probe beam is more invasive, it is not preferred. The selection of a current bias at 250 mA for the non-coherent light source is optimal for this case study. The probe beam power on the DUT at this setting is about $0.22 mW \cdot \mu m^{-2}$. This setting is used for the reflectance modulation studies in the next chapters.

5.4 Spatial Resolution

As discussed in Section 3.3, the determination of an absolute and authoritative spatial resolution value is difficult. It depends on the selected resolution criteria, the type of optical system, the objective lens and the coherence of the light source. The Rayleigh's Criterion is assumed in the determination of the optical spatial resolution. The incident wavelength is 1.34 µm. The objective lens at 50x magnification has an NA of 0.6. The minimum resolvable spatial resolution is calculated to be 1.36 µm.

5.5 Telecentricity and Sample Tilt

A study was conducted to determine the effect of sample tilt on laser reflectance images for a telecentric system. A resistive meandering structure is backside prepared at a substrate thickness of 100 µm, mounted on a two-axis tilt stage and secured on the DUT stage. Optical correction was carried out to ensure the DUT was not tilted.

Without an electrical bias, two reflected images were captured one after another. The two images were subtracted and presented in Figure 5.6a. The white areas represent positive difference, the black areas represent negative difference and the gray areas represent negligible change. The difference image is sharp and uniform with the edges of the resistive structure showing the largest difference

(positive on one edge and negative on the other) due to a slight lateral shift in the sample.

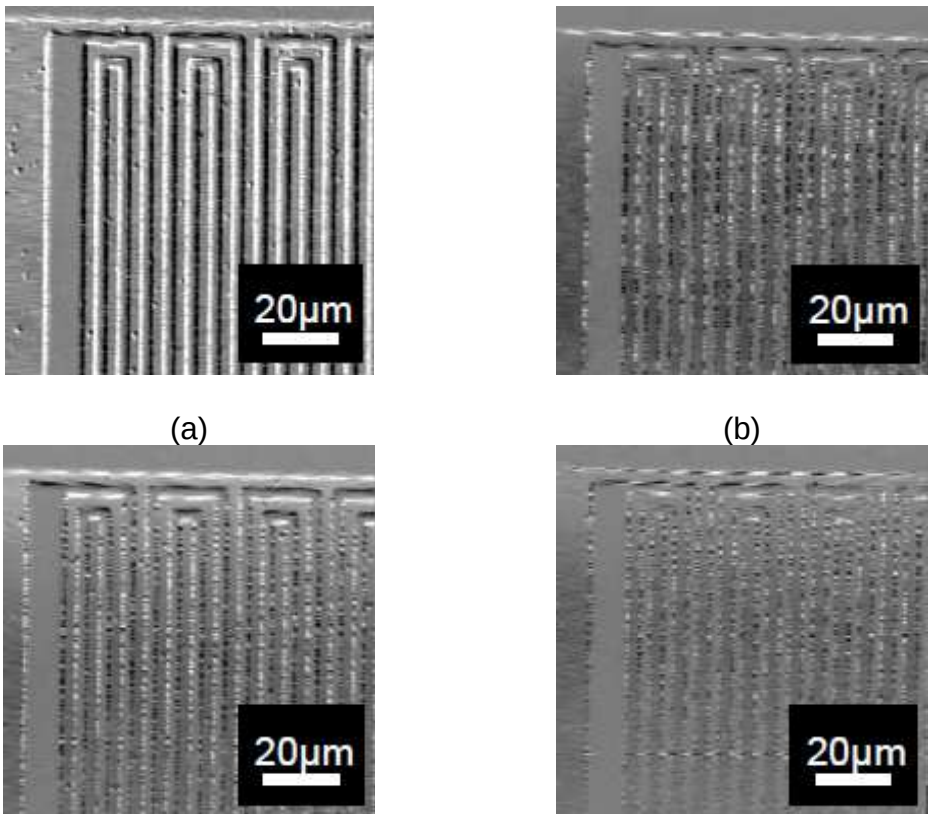

(a) (b)

(c) (d)

Fig. 5.6: Differential images at sample tilt (a) 0º, (b) 3º, (c) 6º and (d) 9º

In a telecentric system, when the sample is tilted, the reflected intensity is weaker, and image distortion is expected. The sample was tilted from the object plan by 3 degrees, and two subsequent reflected images are measured to determine the differential image shown in Figure 5.6b. The difference image is not sharp and the difference is smaller. Along the same edge, the difference may be positive or negative.

The process is repeated for two additional tilt angles of 6 degrees and 9 degrees, with the corresponding differential images shown in Figures 5.6c and 5.6d. Observations similar to Figure 5.6b are made. The study highlighted the importance of ensuring the DUT is aligned to the object plane before carrying out the reflectance modulation experiments.

5.6 Measurement Methods

This research focuses on developing reflectance modulation techniques suitable for both reflectance modulation measurements due to temperature effect and electro-optical effect. The techniques are classified according to the electrical bias configuration of the DUT. When a DC bias is applied, the technique is referred as static. The technique is referred as dynamic when AC bias is used.

5.6.1 Static Reflectance Modulation Technique

The setup in Figure 5.7 can be used for both static and dynamic techniques. In the static technique, a DC electrical bias is applied to the DUT, and the reflected intensity at each point is detected by the photon detector and amplified as signal V_a without the Lock-in Amplifier. As the scan mirror sweeps laterally across the X and Y axes, a reflected image is reconstructed.

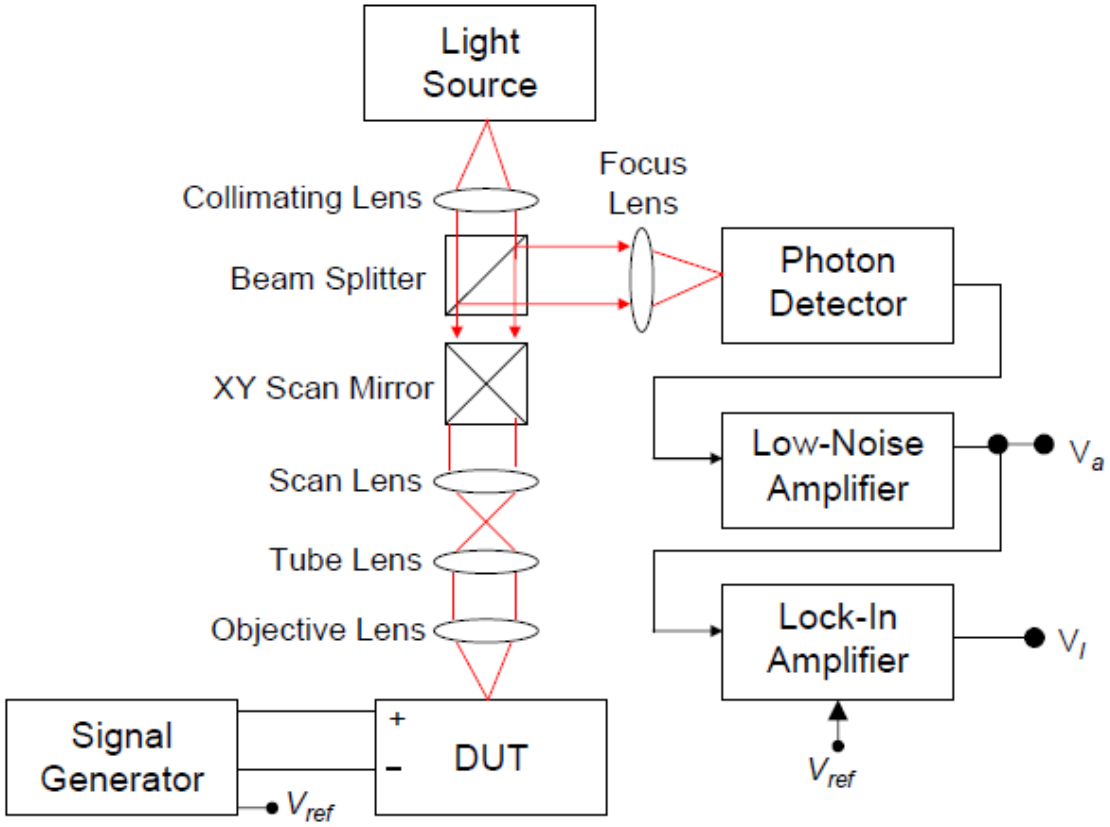

Fig. 5.7: Setup for static and dynamic techniques

To determine the reflectance modulation at each point, a reflected image of the DUT is captured when no electrical bias is applied. This serves as the reference image. Subsequently, DC electrical bias is applied. The temperature on the DUT will change due to Joule heating [70]. Another reflected image of the DUT is then captured after thermal equilibrium is reached. This is referred as the biased image. A difference image is determined by taking the relative difference of each pixel in the biased image with its corresponding pixel in the reference image. Each pixel of the difference image provides information of the relative reflectance modulation at that point.

Continuous wave (CW) and pulsed light sources at 1.34 µm wavelength have been separately used, with the rest of the setup unchanged. Pulsing is known to reduce the heating effect of the probe beam and enhance sensitivity with the accumulation of acquisition data [94]. The improvement in signal sensitivity with pulsing is illustrated in Section 7.1. If the reflectance modulation signal is relatively strong, CW light source is preferred since the data acquisition time is shorter and the experimentation is simpler.

5.6.2 Dynamic Reflectance Modulation Technique

Section 7.1 illustrates a particular case where the static techniques do not have the required sensitivity to detect the reflectance modulations of the probed device. In such cases, the dynamic setup is used, as shown in Figure 5.7. AC electrical bias is applied to the DUT, and a lock-in amplifier is used to enhance the sensitivity of the response with resulting signal V_I at the reference frequency V_{ref}. The output V_I is differential in nature, enhancing signals at the reference frequency and discriminating unwanted signals at other frequencies.

Only CW 1.34 µm light source is used. As the beam scans laterally across the X and Y axes, the differential image is reconstructed without additional processing necessary. Again, each pixel of the differential image provides information of the relative reflectance modulation at that point. Due to the additional lock-in

amplifier, the dynamic technique is capable of achieving much higher sensitivity compared to the static technique.

Depending on the underlying physical phenomenon where the reflectance modulation may be due to temperature effect or electro-optical effect, the appropriate measurement technique is used. The application of the static and dynamic techniques in reflectance modulation measurements of different microelectronic devices are shown in the next chapters.

Chapter 6 Reflectance Modulation of Microscale Metal Interconnects

Frontside and backside laser reflectance modulations of resistive devices which result from Joule heating due to an applied electrical bias are compared using the static technique. The variation of backside laser reflectance modulations of resistive devices with different dimensions and substrate thicknesses at different electrical biases are presented. The experimental results are compared with the backside reflectance modulation model discussed in Chapter 4. The backside reflected intensity is found to modulate negatively with increasing temperature and is one to two orders of magnitude higher than published results.

6.1 Sensitivity

An aluminium (Al) resistive structure #R1 with 2 µm metal line width is backside prepared with 140 µm substrate thickess, as shown in Figure 6.1. Using a 1.34µm CW light source, the reflectance modulations for the static technique at different electrical biases are determined, and the respective line profiles across AA' are presented.

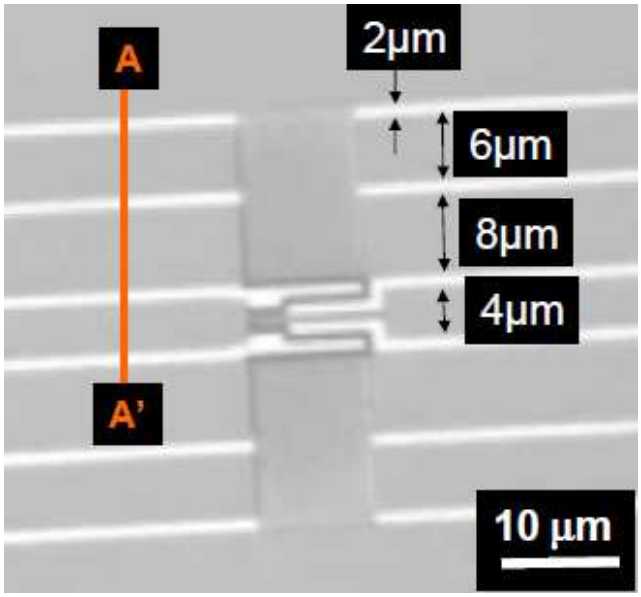

Fig. 6.1: Reflected image of resistive structure #R1

Figure 6.2a shows the reflected intensities across line profile AA' of Figure 6.1 at an electrical bias of 0, 6, 11 and 18 mW. The reflected intensities across the metal lines are much higher than the spacing in between as the metal lines reflect more light. The decrease in the reflected intensity due to an increase of electrical bias is clearly observed. The reflected intensity in the spacing area is also modulated due to heating from the metal lines.

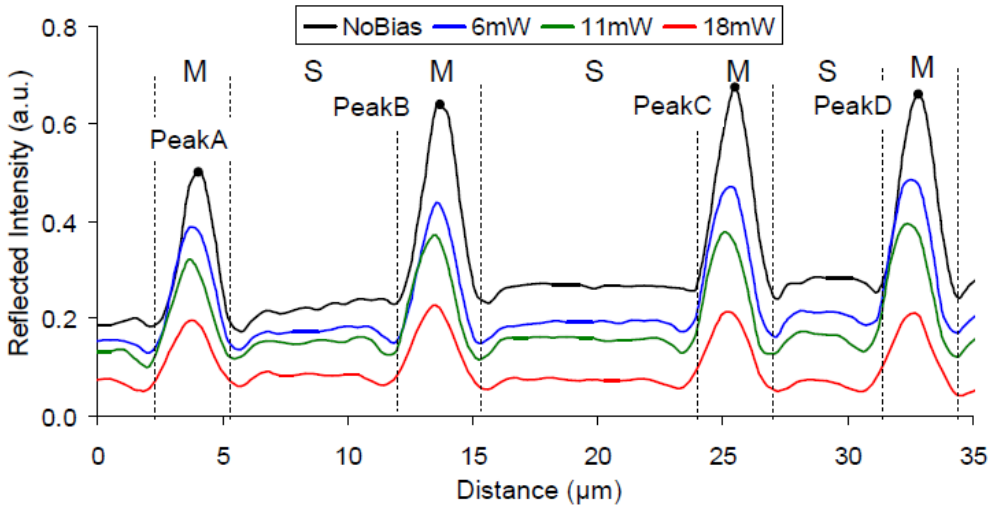

(a)

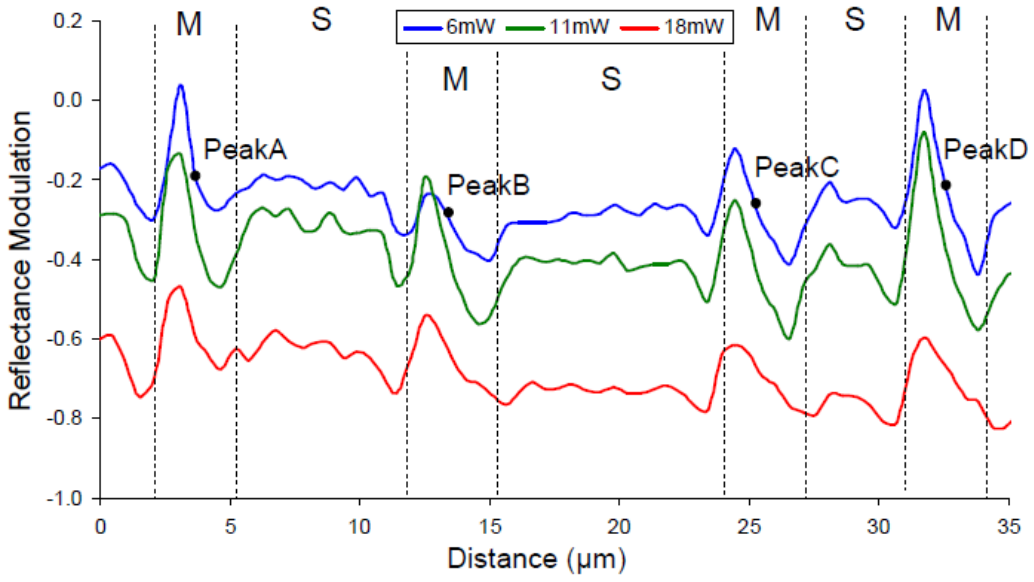

(b)

Fig. 6.2: (a) Reflected intensity, and (b) reflectance modulation using the static technique across metal (M) lines and spacing (S) of line profile AA'

The reflected intensities when no electrical bias is applied serve as the reference. For each applied DC electrical bias, the reflectance modulation at each point is computed by taking the relative difference of that biased point with respect to the

reference point, as shown in Figure 6.2b. The locations of the peak reflected intensities A, B, C and D of the metal lines in Figure 6.2a are highlighted in Figure 6.2b. At those locations, the reflectance modulations are distinct for the applied electrical bias. As an illustration, the reflected intensity of Peak B at no electrical bias and 6 mW DC bias are 0.64 and 0.44 respectively. The reflectance modulation at that point is calculated as $\frac{0.44-0.64}{0.64}=-0.312$. A negative value denotes a smaller reflected intensity at the applied electrical bias. A positive value denotes a larger reflected intensity at the applied electrical bias.

The reflectance modulations in the spacing are more uniform compared to the metal lines. It is also observed the peaks and valleys of the reflectance modulation correspond to the edges of the metal lines, as a result of lateral displacement, and those points are classified as false edge effects. It is observed the static technique with CW 1.34 µm light source has enough sensitivity for thermoreflectance measurements.

In typical cases, the static technique has enough sensitivity to determine the reflectance modulations of the metal lines at different applied electrical bias. The static technique is simpler in terms of experimental apparatus and implementation. In such cases, the static technique is preferred due to these advantages. For the rest of this chapter, the reflectance modulation results are acquired using the static technique.

6.2 Reflectance Modulation at Different Applied Electrical Biases

An Al meandering resistive structure #R2 from a commercial 0.18 µm technology process with metal line width of 4 µm and spacing of 4 µm is backside prepared with substrate thickness of 240 µm, as shown in Figure 6.3. Electrical bias is applied across the pads marked V_{b+} and V_{b-}, and the reflectance modulation within Area C is observed, for both frontside and backside techniques.

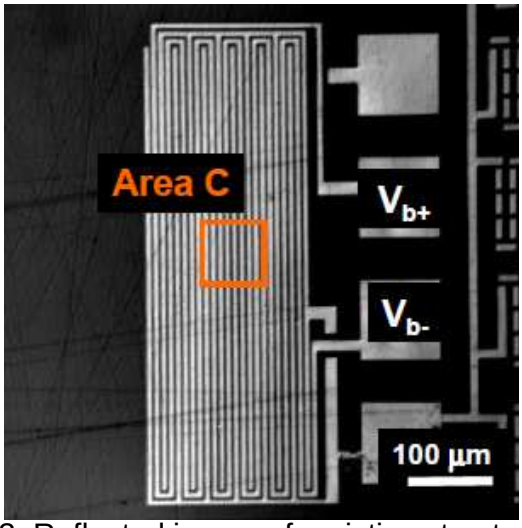

Fig. 6.3: Reflected image of resistive structure #R2

6.2.1 Backside Reflectance Modulation

The backside reflectance modulations for sample #R2 are measured using the static technique with 1.34 µm CW light source with an objective lens at 20X magnification and electrical bias of 17, 37 and 66 mW. The differential reflectance modulation images are presented in Figure 6.4. As discussed, sample #R2 is a resistive device, so the electrical bias results mainly in Joule

heating [70]. The temperature change results in a variation of the refractive index and absorption coefficient, modulating the reflected laser intensities.

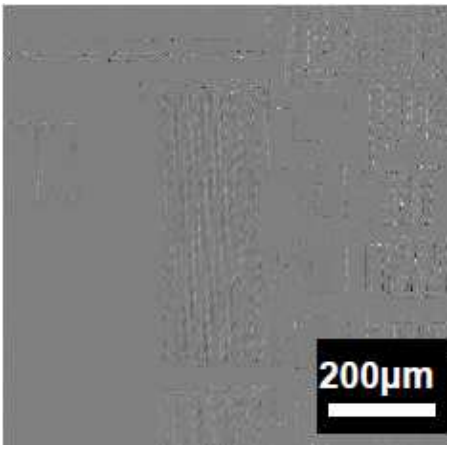

(a)

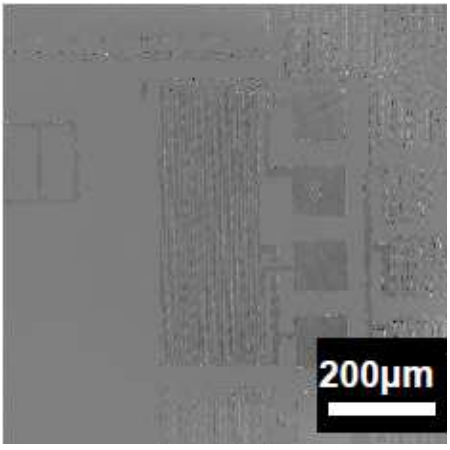

(b)

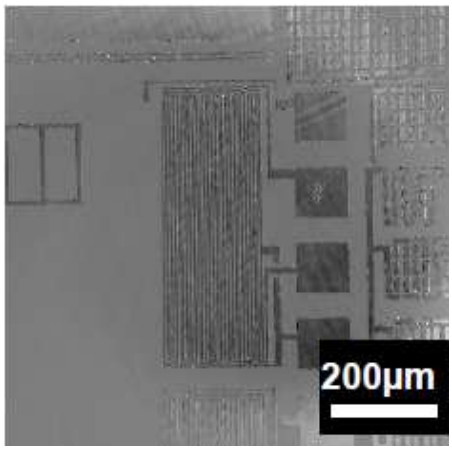

(c)

Fig. 6.4: Differential reflectance modulation images of sample #R2 at an electrical bias of (a) 17 mW, (b) 37 mW and (c) 66 mW

As the applied electrical bias is increased, the biased resistive device is observed to darken significantly compared to the rest. The biased device can thus be easily identified from the rest using the differential reflectance modulation images.

An objective lens at 50X magnification is used to acquire the backside reflectance modulations of Area C with the static technique at 4 and 16 mW as shown in Figure 6.5a and 6.5b respectively which are transformed in rainbow pseudo-colour where the red areas represent the largest reflectance change and the blue areas represent the least change.

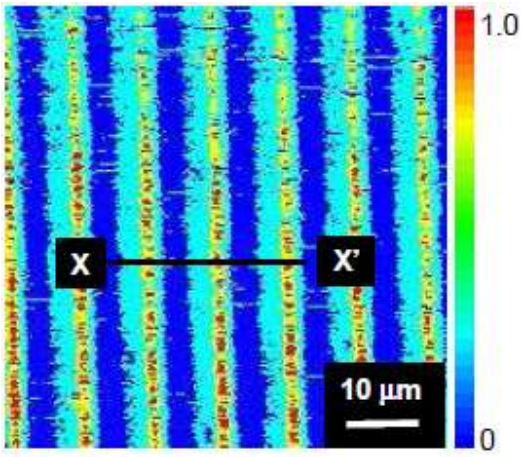

(a)

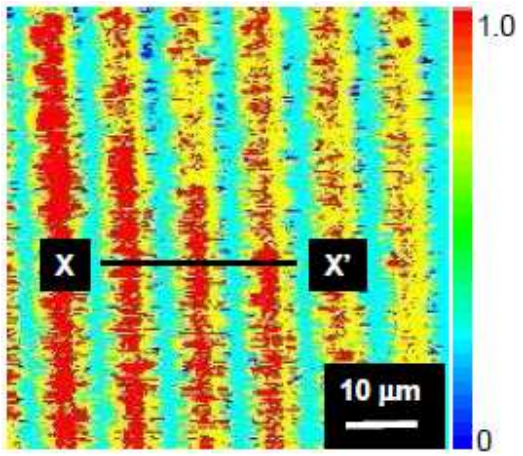

(b)

Fig. 6.5: Reflectance modulation of area C for
(a) 0 – 4 mW and (b) 0 – 16 mW bias

At the lower electrical bias of 4 mW, the reflectance modulation across each metal line is relatively symmetrical, with negligible reflectance modulations for the spacing in between. At the higher electrical bias of 16 mW, the reflectance modulations across the metal lines vary, indicating non-uniform heating on the metal lines, possibly due to variations in the fabrication process. Larger reflectance modulations on the metal lines are observed. Reflectance

modulations are also observed on the spacing in between, indicating the substrate is heating up due to the applied electrical bias. The micrographs clearly showed greater reflectance modulation result from higher electrical bias. Figure 6.6 shows the reflected intensity variation across the line profile XX' of Figure 6.5a and 6.5b.

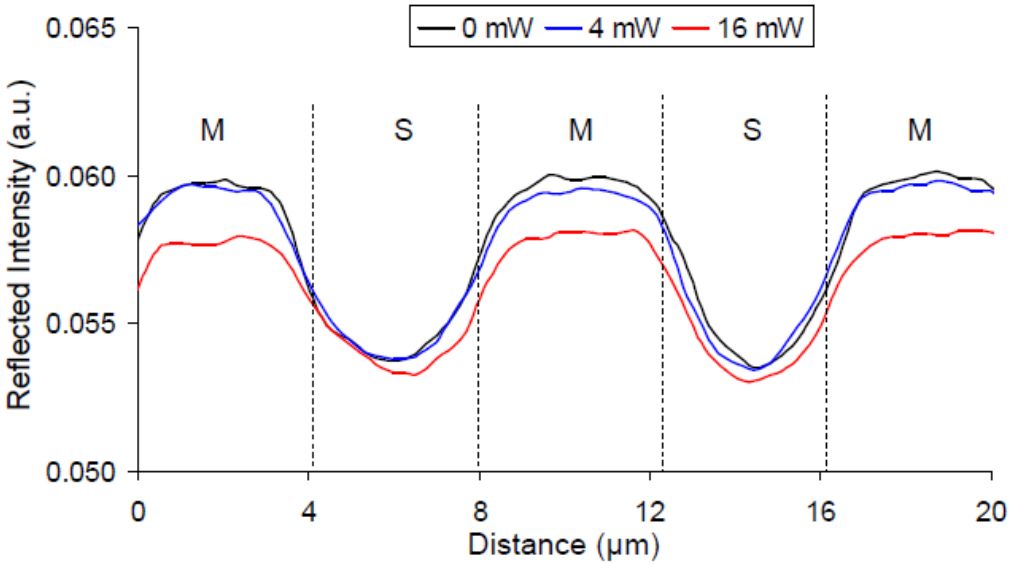

Fig. 6.6: Line profile XX' of reflected intensity for sample #R2 across metal (M) lines and spacing (S)

The trend is similar to observations made in Figure 6.2a. The decrease in the reflected intensity modulation due to an increase in electrical bias is observed. At a higher electrical bias, the reflected intensity in the spacing area is also modulated due to heating from the metal lines. At an electrical bias of 4 mW and 16 mW, the temperature change of the metal line is 5.5 and 11.6 K respectively.

6.2.2 Frontside reflectance modulation

Figure 6.7 shows the reflected intensity variation across line profile XX' of Sample #R2 measured using the frontside static laser reflectance modulation technique. A higher electrical bias is needed to observe the reflectance modulation as the magnitude of the reflectance modulation for the frontside technique is poorer than the backside technique. The reflected intensity from the metal surface is affected by lateral and vertical expansions at a higher temperature. Compared to backside technique, more severe lateral displacement is expected. Reflectance modulations from uneven metal surfaces at higher temperature may also result in erroneous results.

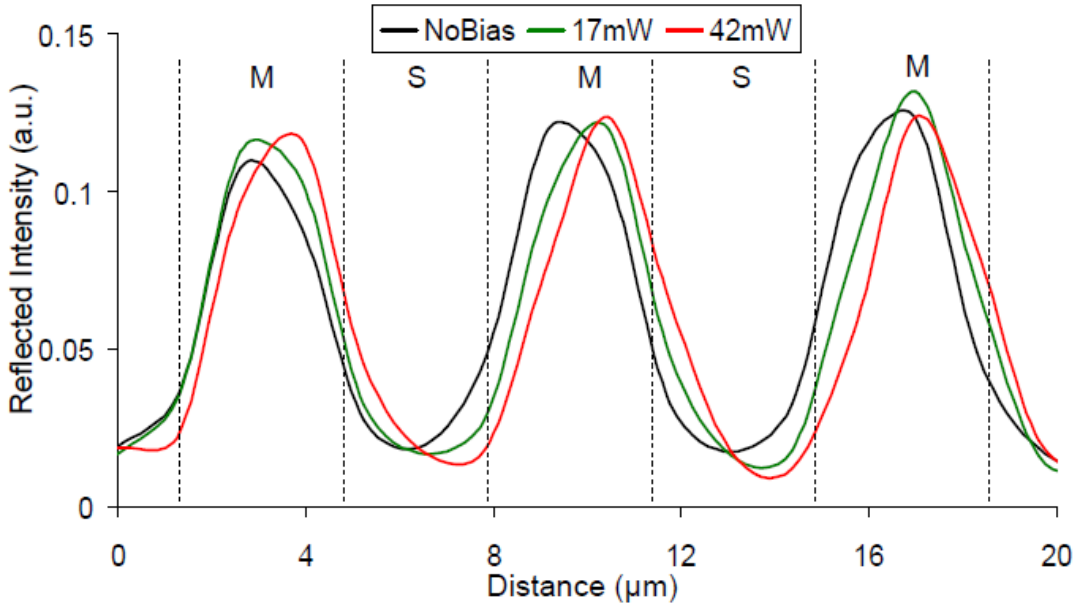

Fig. 6.7: Line profile XX' of reflected intensity from the frontside for sample #R2 across metal (M) lines and spacing (S)

The results show the reflectance modulation due to the electrical bias is small. For two of the three metal lines, a higher electrical bias is observed to result in higher reflected intensity. As observed, the lateral displacements of the metal lines are more severe compared to the backside-based technique. The determination of the temperature variation due to the thermoreflectance modulation requires accurate determination of the passivation thickness on the metal lines [71] of Sample #R2 which has not been attempted. This section presented a comparison study of frontside and backside thermoreflectance modulations using similar samples and experimental techniques. It is observed the reflectance modulation for the backside technique is larger compared to the frontside technique.

6.3 Backside Reflectance Modulation at Different Dimensions

The backside reflectance modulation results of resistive structures #R1 and #R2 are compared to study the effect of device dimension. Sample #R1 is designed to be temperature calibrated using four-point measurements of the resistance change with temperature.

A sample is backside prepared and temperature calibrated, so that the temperature of the metal line when biased can be accurately determined. The substrate thickness is initially polished to 500 µm, and reflectance modulation measurements are carried out.

The sample is then polished to reduce the substrate thickness until a series of reflectance measurements are obtained at different substrate thicknesses. Two such samples are used to ensure consistency of the results. The absorption coefficient of Sample #R1 at room temperature is experimentally determined to be about 8 to 10 cm^{-1}. Figure 6.8 shows the results from Sample #R1 at a substrate thickness of 340 µm.

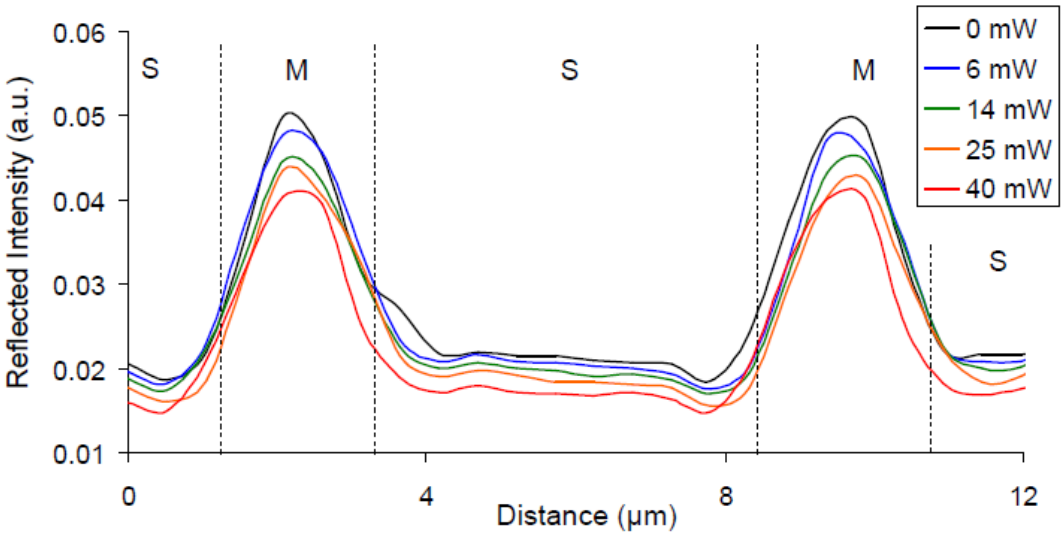

Fig. 6.8: Line profile AA' of reflected intensity for sample #R1 across metal (M) lines and spacing (S)

In this case, as the relative spacing between the metal lines increases, the reflected intensity in the spacing area is flatter to show that indirect heating from the smaller metal lines is not as severe as Sample #R2. At an electrical bias of 6, 14, 25 and 40 mW, the temperature changes of the metal line are 3.4, 10.0, 19.0 and 25.8K respectively.

The peak reflectance intensity modulations of the metal lines are used to derive the reflectance coefficient *r* and thermoreflectance coefficient *k*. Table 6.1 tabulates the coefficients of the metal lines together with calculated values using the model in Section 4.3 and published results for other metal thin films based on the frontside and backside techniques. The derived *r* and *k* values are based on metal line temperature change of 10.0 K for Sample #R1 and 11.6 K for Sample #R2.

Table 6.1: Compiled reflectance coefficients

	r	k (K^{-1})	*Remarks*
Sample #R2, Experiment	-3.34×10^{-2}	-2.88×10^{-3}	Backside
Sample #R2, Model	-3.83×10^{-2}	-3.30×10^{-3}	Backside
Sample #R1, Experiment	-7.33×10^{-2}	-7.33×10^{-3}	Backside
Sample #R1, Model	-4.61×10^{-2}	-4.61×10^{-3}	Backside
Shimizu [82]	2×10^{-3}	6.67×10^{-5}	Frontside
Quintard [71]	1.5×10^{-3}	5.68×10^{-4}	Frontside
	3.1×10^{-3}	1.20×10^{-3}	Frontside
Tessier [64]	3.80×10^{-3}	1.17×10^{-4}	Backside

The experimental *r* and *k* values are negative and agree well with the calculated values. However, the published *r* and *k* values are one to two orders of magnitude lower. This is because for the frontside measurements, the absorption of the passivation layers is low and positive reflected intensity modulation is due

mainly to the temperature variation of reflectance. The phenomenon has been verified by published frontside reflectance models [34, 71].

For the backside values by G Tessier [64], an undoped Si substrate was used. In that case, the absorption coefficient is negligibly small at the NIR wavelength, and the reflected intensity modulation is due primarily to the temperature variation of reflectance.

The model is modified to neglect the absorption coefficient in the case of undoped Si, so that the backside reflection model only accounts for the temperature variation of reflectance. The calculated values of *r* and *k* are compared to G Tessier's published results [64] at a substrate thickness of 500µm, as tabulated in Table 6.2. The temperature change on the metal line is 32.5K in [64] and in the model.

Table 6.2: Reflectance coefficients for the undoped substrate

	r	k (K^{-1})	*Remarks*
Tessier [64]	3.80×10^{-3}	1.17×10^{-4}	ΔT=32.5K
Model	1.45×10^{-3}	4.45×10^{-5}	ΔT=32.5K

In this case, the values of *r* and *k* obtained are positive when the reflected intensity modulation is primarily due to the temperature variation of reflectance and are close to the values obtained by Tessier. The results indicated the

negative *r* and *k* values obtained in Table. 6.1 are due to the temperature variation of the absorption coefficient which results in negative reflectance modulations at a higher temperature.

6.4 Backside Reflectance Modulation at Different Substrate Thicknesses

6.4.1 Without an Electrical Bias

Figure 6.9 shows the reflected intensities at substrate thicknesses of 140, 240, 340 and 500 µm for Sample #R1 without an electrical bias, i.e. at room temperature. The solid line is generated by the model described in Section 4.3.

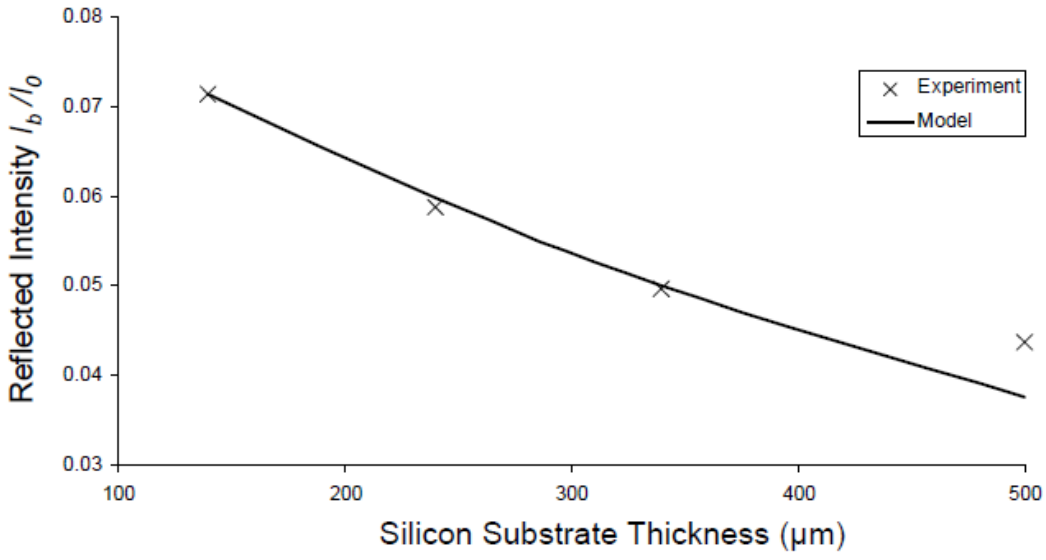

Fig. 6.9: Reflected intensities at different substrate thicknesses and room temperature

The measured reflected intensities are dependent on instrument gain while the reflected intensities calculated from the model are fully corrected for no gain. As

such, a constant scaling factor is used on all the measured reflected intensities so that the measured reflected intensity at a substrate thickness of 140 μm is equivalent to the model. The experimental points are in good agreement with the model.

6.4.2 With an Electrical Bias

In another experiment, the same set of electrical bias is applied to each substrate thickness of Sample #R1 to measure the reflected intensities at different substrate thickness. The backside reflectance model is used to determine the reflected intensities at metal line temperatures of 300, 310, 320, 330 and 340K, and substrate thicknesses of 140, 240, 340 and 500 μm. Figure 6.10 shows the experimental and calculated reflected intensities.

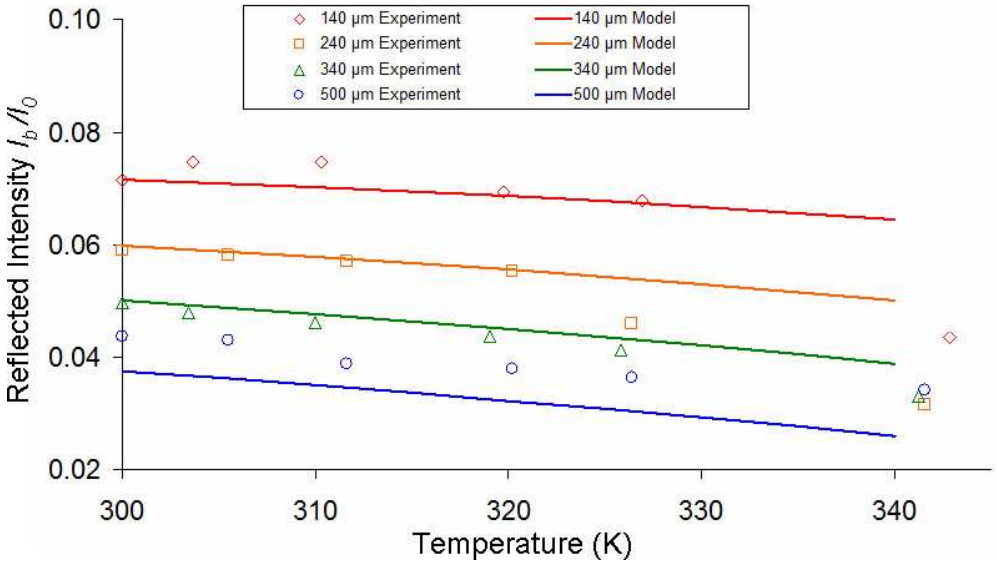

Fig. 6.10: Reflected intensities at different thicknesses and temperatures

It is observed the reflected intensities decrease as the temperature on the metal line increases. The experimental data agree well with the model, except at a high temperature. An offset is also observed when the substrate thickness is 500 µm. At a high substrate thickness, a temperature gradient exists across the substrate. The effective absorption coefficient is therefore lower than the uniform value used in the model.

As before, the peak reflectance intensity modulations of the experimental and model values for the metal lines are used to determine *r* and *k* values at different substrate thickness. The derived *r* and *k* values are based on metal line temperature change of 20 K. The coefficients are tabulated in Table 6.3. Experimental and model values are observed to agree well. The *r* and *k* values increase with increasing substrate thickness due to the decrease in unbiased reflected intensity and the increase in absorption.

Table 6.3: Reflectance coefficients at different substrate thickness

	Experiment	*Model*	*Experiment*	*Model*
Substrate Thickness (µm)	r	r	k (K^{-1})	k (K^{-1})
500	-13.14×10^{-2}	-14.13×10^{-2}	-6.51×10^{-3}	-7.07×10^{-3}
340	-12.15×10^{-2}	-9.82×10^{-2}	-6.39×10^{-3}	-4.91×10^{-3}
240	-6.32×10^{-2}	-7.01×10^{-2}	-3.13×10^{-3}	-3.50×10^{-3}
140	-3.01×10^{-2}	-4.11×10^{-2}	-1.53×10^{-3}	-2.06×10^{-3}

6.5 Summary

The static backside reflectance technique is observed to be suitable for most thermoreflectance characterizations. The backside reflectance modulation is larger than the frontside reflectance modulation. The backside reflectance intensities are observed to modulate negatively with electrical bias for the case when the absorption coefficient of the Si substrate varies significantly with temperature compared to the reflectance. In this case, the reflectance and thermoreflectance coefficients are one to two orders of magnitude larger than the values for the frontside reflectance measurements or when the Si substrate is undoped.

The experimental data are found to agree well with the developed backside reflectance model. The reflected intensity modulation with electrical bias depends on the reflectance, absorption coefficient and substrate thickness. Positive or negative reflected intensity modulation depends on whether the modulation is due primarily to the temperature variation of the absorption coefficient or the reflectance.

Chapter 7 Characterization of MOS Transistor Channel

The channel of MOS transistors is characterized using static and dynamic laser reflectance modulation techniques at linear, pinch-off and saturation modes of operation [53]. The static techniques lacked sensitivity. The dynamic technique employs lock-in amplification to enhance the sensitivity of the response, and is used to characterize NMOS and PMOS devices for variation in modulation frequency, gate bias, channel length and MOS device type. The reflectance modulations of the channel contain a primary peak near the drain-end when the MOS transistor is in saturation mode. The location of the primary peak is compared with the pinch-off point from the drain-end based on the Pseudo-Two-Dimensional Model. The experimental and analytical values are found to be in good agreement.

7.1 Sensitivity

An NMOS transistor from 0.18 µm process technology node with channel width W = 10 µm and L_{mask} = 2 µm is backside prepared at a substrate thickness of 350 µm. Figure 7.1 shows the reflected backside image with the channel enclosed in Area D and line profile YY' across the channel.

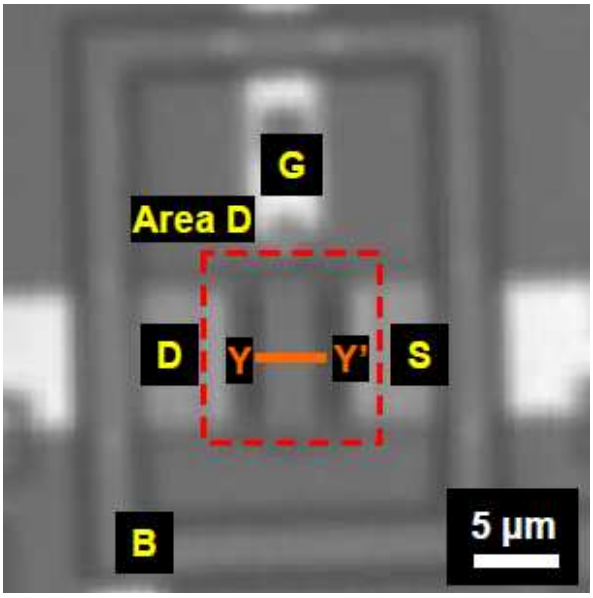

Fig. 7.1. NMOS transistor with *Lmask* = 2µm

Figure 7.2 shows the I_{DS}-V_{DS} characteristic of the NMOS transistor. The transistor is first put in inversion mode by applying V_{GS}= 5V. Then, the bias points of V_{DS} are selected to cover the full operating modes: V_{DS}= 0V (unbiased), V_{DS}= 1V (linear), V_{DS}= 2V (pinch-off), V_{DS}= 3V to 5V (saturation) of the NMOS transistor. This bias scheme is used in the reflectance modulation experiments.

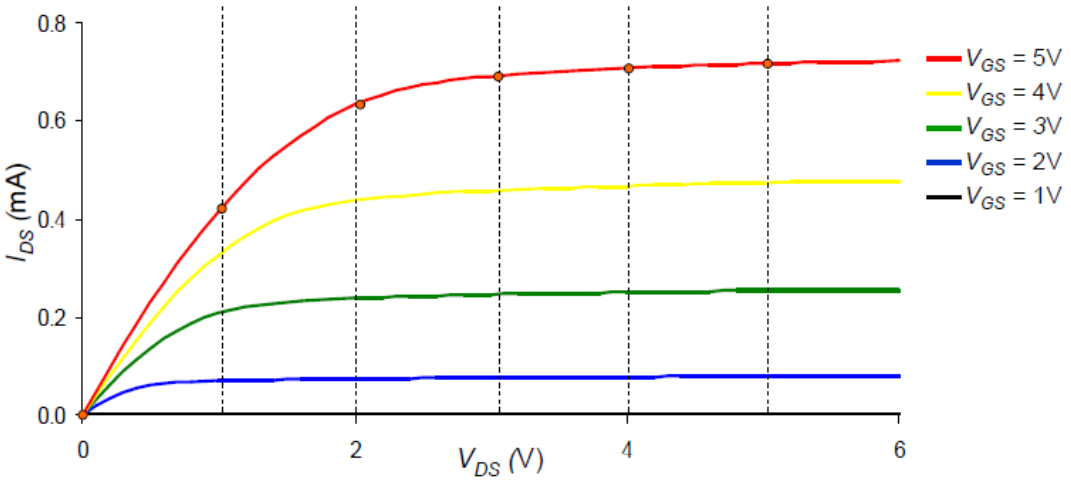

Fig. 7.2. The I_{DS}-V_{DS} characteristics of NMOS transistor with L_{mask}= 2 µm

In the static technique, as discussed in Section 5.6.1, an non-coherent 1.34 µm CW light source is used. Source S and bulk B are grounded. DC bias V_{GS} and V_{DS} are applied to gate G and drain D, with reflected signal V_a. The experimental setup is shown in Figure 5.7. The experimental spatial error is ±0.25 µm. Lower spatial error is possible with the use of solid immersion lens [19]. The relative difference of each pixel is computed and denoted as ΔV_a.

Figure 7.3 shows the ΔV_a of Area D as seen in Figure 7.1 when both V_{DS} and V_{GS} are 5V, transformed in pseudo-color. The red areas represent significant positive reflectance modulations. The blue areas represent significant negative reflectance modulations. The green areas represent negligible reflectance modulations. The reflectance modulations within the channel are visibly negligible, and significant reflectance modulations are observed at the edges due to false edge effects which are not areas of interest.

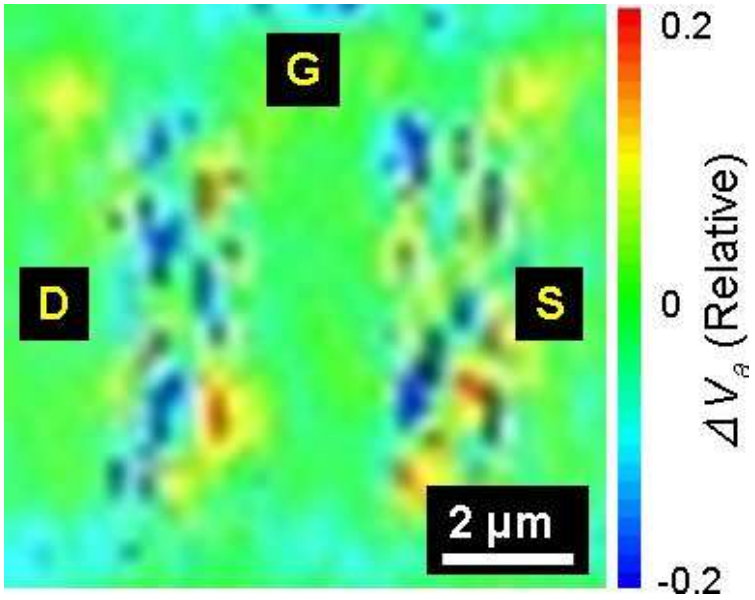

Fig. 7.3. Pseudo-color image of ΔV_a in area D for NMOS transistor with L_{mask} = 2 µm when both V_{DS} and V_{GS} are 5V, using static technique with CW laser

The ΔV_a plotted across the channel YY' is shown in Figure 7.4. Significant reflectance modulations are expected near the drain-end, increasing in intensity with V_{DS}. No such coherent trend is observable. It is apparent that the static technique with CW light source lacks sensitivity as shown in this case.

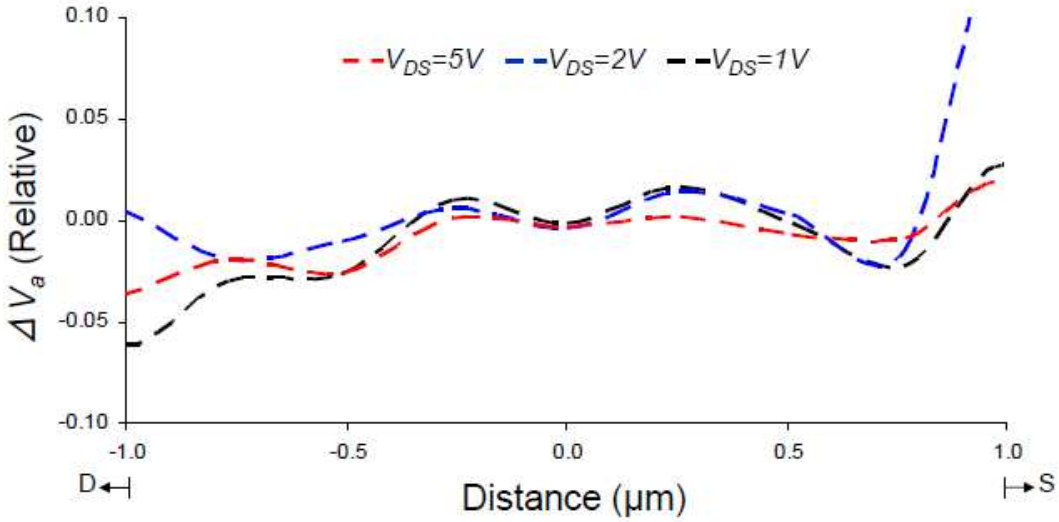

Fig. 7.4. Plot of ΔV_a across channel YY' using static reflectance modulation technique and CW laser

Figure 7.5 shows another line profile of the same region using the static technique, but with pulsing at 7.33 kHz and 50% duty cycle. Light pulsing reduces probe beam heating and enhances sensitivity with the accumulation of acquisition data [94].

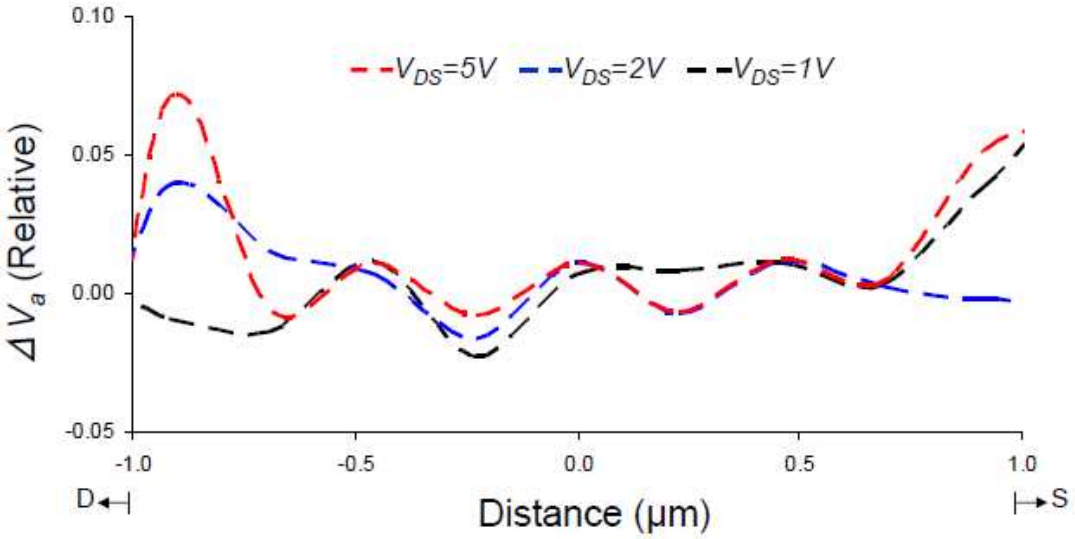

Fig. 7.5. Plot of ΔV_a across channel YY' using static reflectance modulation technique and pulsed laser

With light pulsing, it is observed reflectance modulation increases near the drain-end as the NMOS transits from linear to pinch-off and then to saturation. The trend is very clear when compared to Figure 7.4. The static technique using pulsed laser shows improvement in sensitivity.

In the dynamic technique as described in Section 5.6.2, V_{DS} is modulated by applying square waves at a frequency V_{ref} of 7.33 kHz with 50% duty cycle. Lock-in amplification is used to enhance the sensitivity of the response with a lock-in time constant of 2 ms. The laser dwell time at each pixel is set at 2 ms. The acquisition time for Area D with 100 pixels by 100 pixels takes less than a minute.

This technique relies on the dynamic response of V_{DS}, and is appropriately termed dynamic backside laser reflectance modulation technique. In this

comparison study on sensitivity, the same NMOS transistor shown in Figure 7.1 is used. The differential reflectance of Area D at each bias is transformed in pseudo-color as shown in Figure 7.6. The red areas represent significant reflectance modulations. The blue areas represent negligible reflectance modulations.

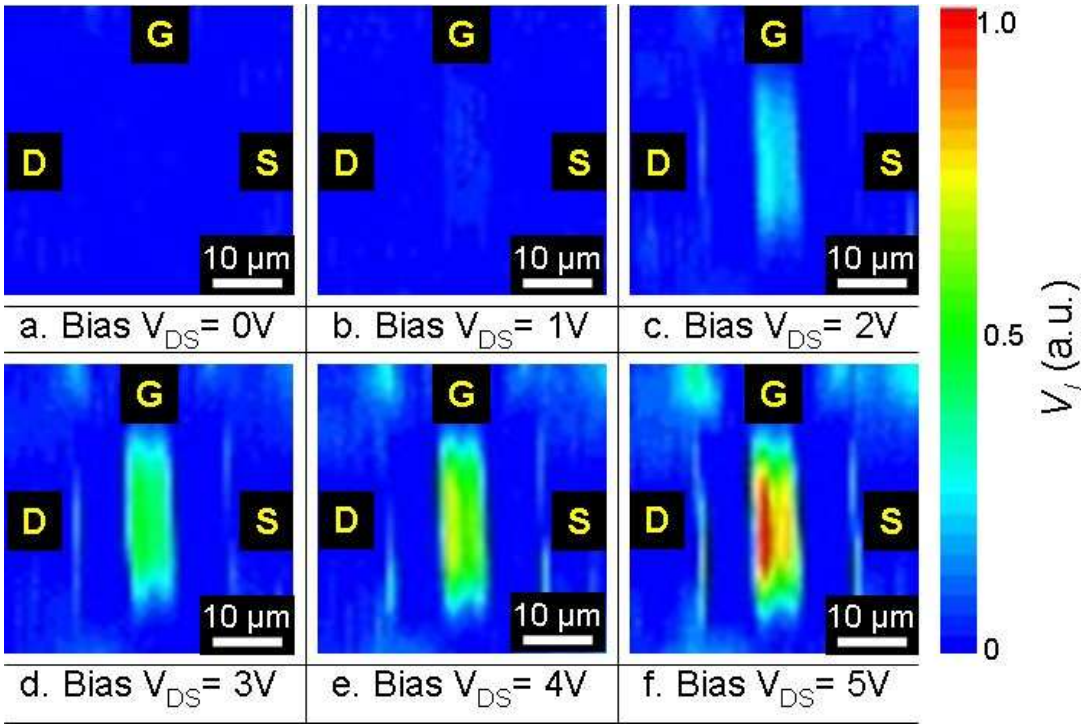

Fig. 7.6. Pseudo-color image of V_I in area D for NMOS transistor with L_{mask}= 2 µm when V_{GS}= 5V and various V_{DS}, using dynamic technique with CW laser

Negligible reflectance modulation is observed when the NMOS device is unbiased or in linear mode. At pinch-off, faint reflectance modulation is detected near the drain-end. In saturation mode, strong reflectance modulation of the channel near the drain-end is clearly observed, increasing in intensity with

increased V_{DS}. It is further noted the edges are more defined resulting in less false edge effect. Plots across the channel YY' is shown in Figure 7.7.

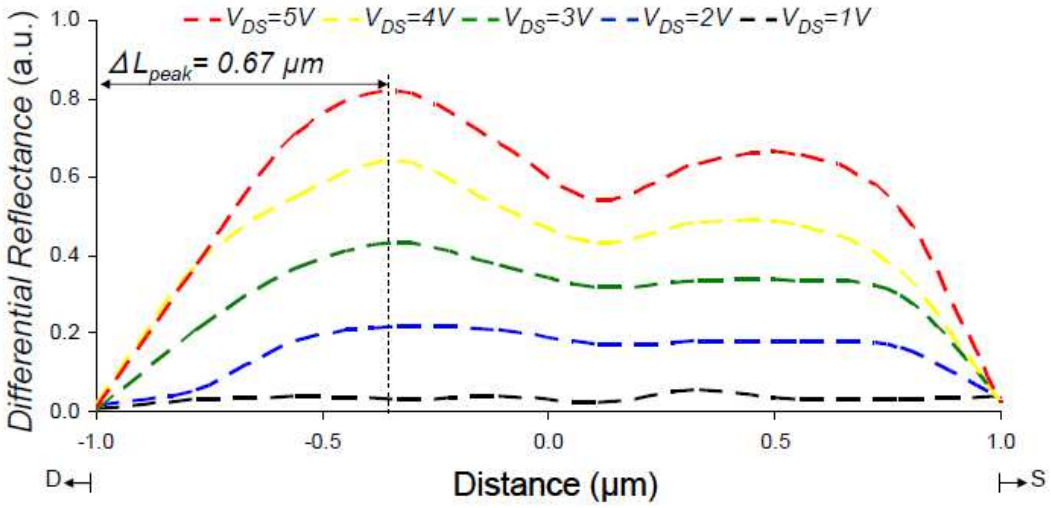

Fig. 7.7. Plot of channel YY' for NMOS transistor with L_{mask}= 2 µm, V_{GS} = 5V and V_{ref} = 7.33 kHz, using the dynamic technique

A distinct peak near the drain-end is seen at V_{DS}= 3V when the NMOS just enters into saturation. With increased V_{DS}, this peak becomes more dominant. The position of the peak from the drain-end is marked as ΔL_{peak}. From V_{DS}= 3V to 5V, ΔL_{peak} is stationary at 0.67 µm from the drain-end. The observations support the hypothesis that reflectance modulation is significant when the NMOS is in saturation.

Comparison of ΔL_{peak} with the length of the *VSR* calculated using Pseudo-Two-Dimensional Poisson Model proposed by PK Ko [58] suggests the primary peak is the pinch-off point. Further studies using the dynamic technique on the reflectance modulations at different V_{ref}, V_{GS}, channel lengths, and MOS types

seek to strengthen this hypothesis and to confirm the observed primary peak is the pinch-off point.

A secondary peak near the source-end is also observed when V_{DS}= 4V and 5V, possibly due to localized heating as a result of non-uniform doping in the channel. The results indicate clearly that the static technique does not have the required sensitivity. With the dynamic technique, the reflectance modulations of the channel at different operating points of the NMOS transistor are distinct, with the pinch-off clearly visible. As such, the dynamic laser reflectance modulation technique can be used to characterize the operating behaviors of the NMOS transistor.

7.2 Variation of Modulation Frequency

The same NMOS transistor with L_{mask}= 2 µm as shown in Figure 7.1 is used to study the variation of V_{ref} on dynamic backside laser reflectance modulation. The thermal conductivity for the Si substrate depends on the dopants and the doping concentration. For pure Si, the thermal conductivity is 150$Wm^{-1}K^{-1}$. Experimentally, for p-doped substrates, thermal conductivity as low as 66$Wm^{-1}K^{-1}$ has been reported. The impurities act as point defects to increase phonon scattering and limit the thermal conductivity [95].

The thermal time constant of Si is therefore highly dependent on the substrate doping as well as the device geometry. Reported values for SOI power devices

range from 50 to 70 µs [96], corresponding to frequencies between 10 to 20 kHz. It is expected as thermal effects would be significant when V_{ref} is less than or equal to 10 kHz. In Figure 7.7, V_{ref} is set at 7.33 kHz. Two additional reflectance modulation measurements are obtained at V_{ref}= 73.33 kHz and 733 Hz in this comparison study. It is expected the thermal effect would be less significant when V_{ref}= 73.33 kHz and more significant when V_{ref}= 733 Hz as compared to Figure 7.7. The differential reflectance plotted across the channel YY' for the reflectance modulations observed when V_{ref} is 73.33 kHz, as shown in Figure 7.8.

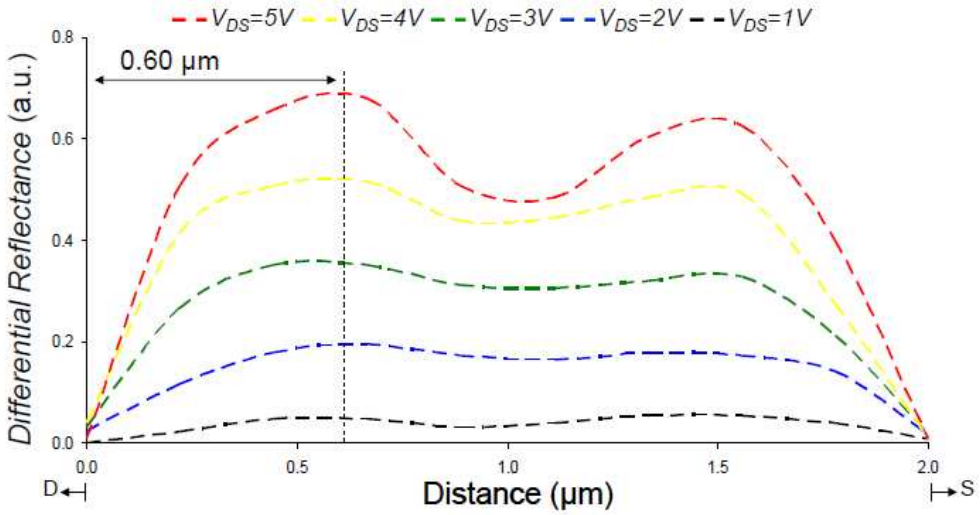

Fig. 7.8. Plot of channel YY' for NMOS transistor with L_{mask}= 2 µm, V_{GS} = 5V and V_{ref} = 73.33 kHz, using the dynamic technique

In Figure 7.8, the observed differential reflectance magnitudes are smaller when compared to Figure 7.7, likely due to the smaller thermal effect of the substrate. When the NMOS is in saturation, a dominant peak is observed as before. ΔL_{peak} is observed to be 0.50 µm when V_{DS}= 3V. As V_{DS} increases, ΔL_{peak} is observed to move towards the source-end, with ΔL_{peak}= 0.60 µm when V_{DS}= 5V. The

secondary peak is more dominant compared to Figure 7.7. With less thermal heat loss to the substrate, the localized heating is likely to be more pronounced, resulting in larger reflectance modulations.

The differential reflectance plotted across the channel YY' when V_{ref} = 733 Hz is shown in Figure 7.9. The differential reflectance is observed to saturate when V_{DS}= 5V. The larger reflectance modulations are likely due to significant substrate thermal effect. The combined temperature and electro-optical effects are observed to cause greater reflectance modulations in the channel. However, the dominant peak is diminished, reducing the effectiveness of the technique to determine the position of ΔL_{peak}. The secondary peak disappears at V_{ref} = 733 Hz. At the reduced frequency, there is more thermal conduction to the substrate, masking the localized heating effect. This reinforces the hypothesis that the secondary peak result from non-uniform localized heating of the channel.

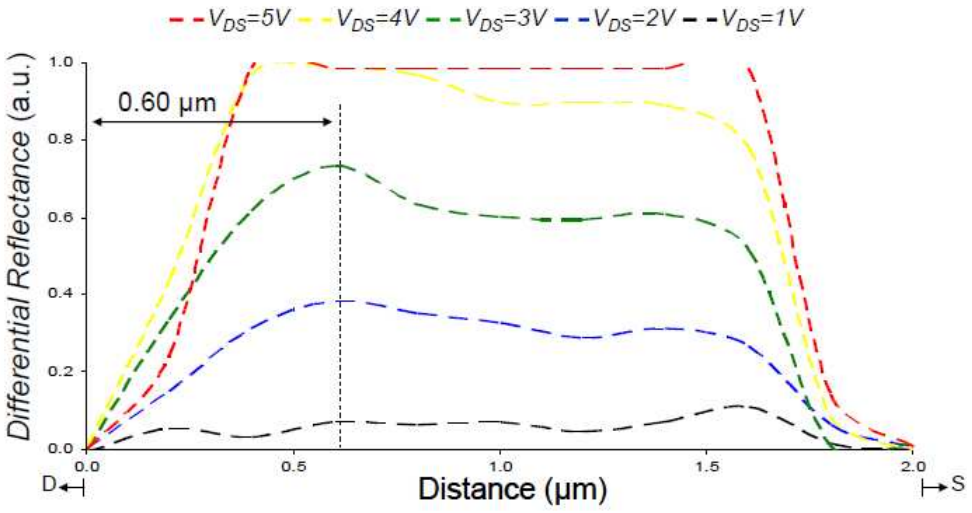

Fig. 7.9. Plot of channel YY' for NMOS transistor with L_{mask}= 2 µm, V_{GS} = 5V and V_{ref} = 733 Hz, using the dynamic technique

The variation in V_{ref} affects the thermal effects due to the substrate. When the NMOS is in saturation, a peak is still observed near the drain-end. The positions of ΔL_{peak} at the three V_{ref} settings are similar with variation in the magnitude of the peaks depending on V_{ref}. The optimal setting for reflectance modulation due to electro-optical and thermal effects are observed when V_{ref}= 7.33 kHz, and is used for the remaining studies.

7.3 Variation of Gate Bias

Another NMOS transistor from 0.18 µm process technology node with channel width W= 10 µm and L_{mask}= 4 µm is backside prepared at a substrate thickness of 350 µm as shown in Figure 7.10 to study the variation of V_{GS} on dynamic backside reflectance modulation.

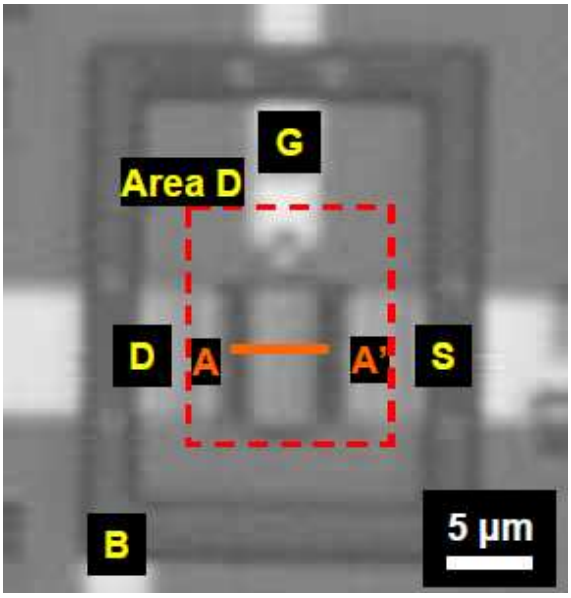

Fig. 7.10. NMOS transistor with *Lmask* = 4µm

Using a parametric analyzer, the measured I_{DS}-V_{DS} characteristics are shown in Figure 7.11. Compared to Figure 7.2, the I_{DSAT} current is significantly smaller due to the longer channel length. The V_{DSAT} values for the two devices are similar.

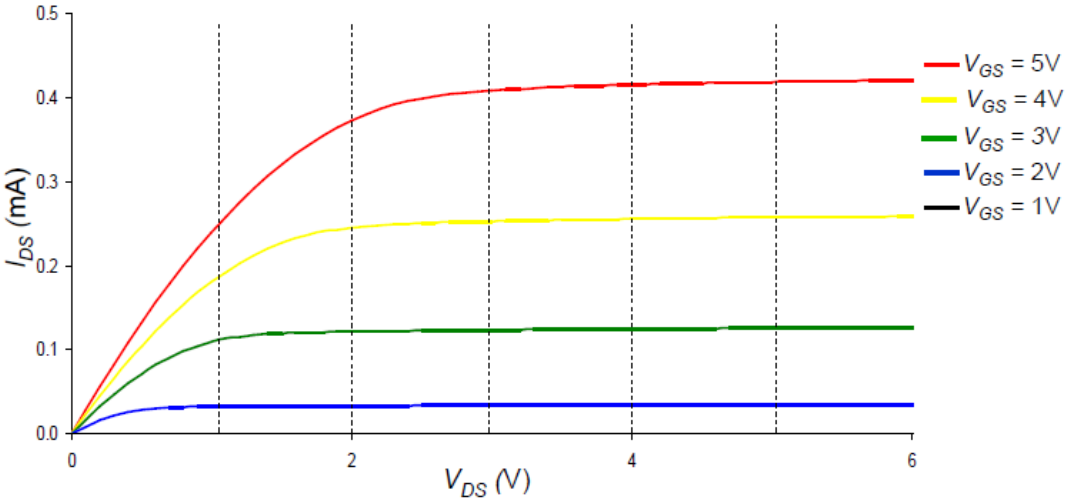

Fig. 7.11. The I_{DS}-V_{DS} characteristics of NMOS transistor with L_{mask}= 4 µm

The differential reflectance of Area D when V_{GS}= 5V and at each V_{DS} bias is transformed in pseudo-color as shown in Figure 7.12. Negligible reflectance modulation is observed when the NMOS device is unbiased or in linear mode. At pinch-off, a faint reflectance modulation is detected near the drain-end. In saturation modes, a strong reflectance modulation of the channel near the drain-end is clearly observed, increasing in intensity with V_{DS}.

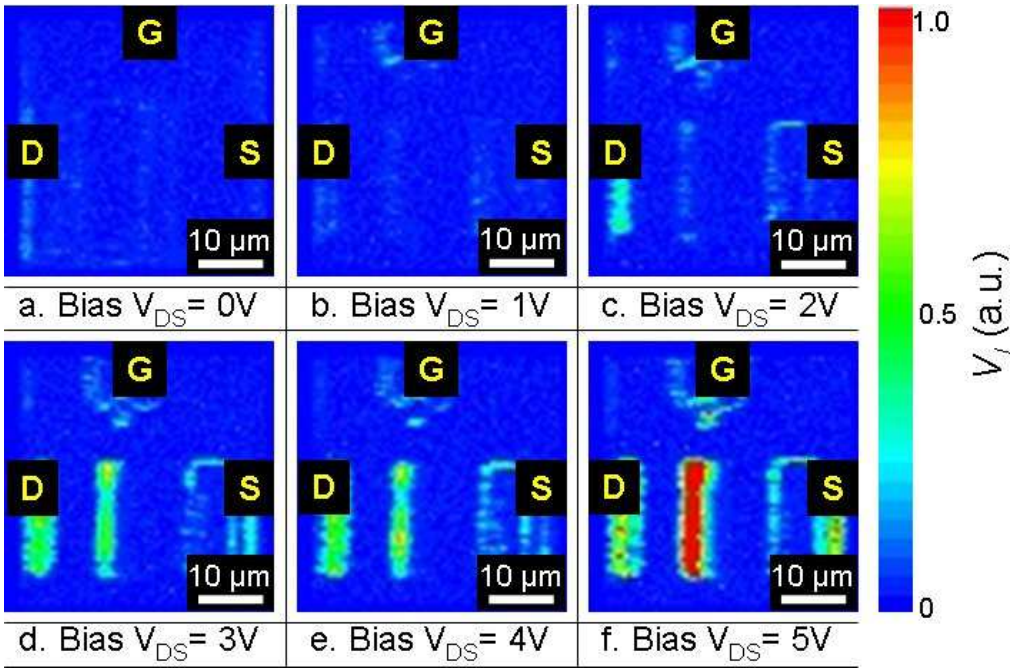

Fig. 7.12. Pseudo-color image of area D for NMOS with L_{mask}=4 µm and V_{GS}=5V

The observations are similar to the trend observed in Figure 7.6. For the larger channel length, the reflectance modulation is barely visible at pinch-off and only partial channel is observed to have significant reflectance modulation when the NMOS transistor is in saturation.

Figure 7.13 shows the differential reflectance plotted across the channel YY' for the reflectance modulations observed in Figure 7.12. Similar to Figure 7.7, a distinct peak is observed near the drain end when the NMOS transistor is in saturation. At V_{DS}=3V, ΔL_{peak} is 0.94 µm. With increased V_{DS}, the peak gradually moves toward the source-end. At V_{DS}=5V, ΔL_{peak} is 1.05 µm.

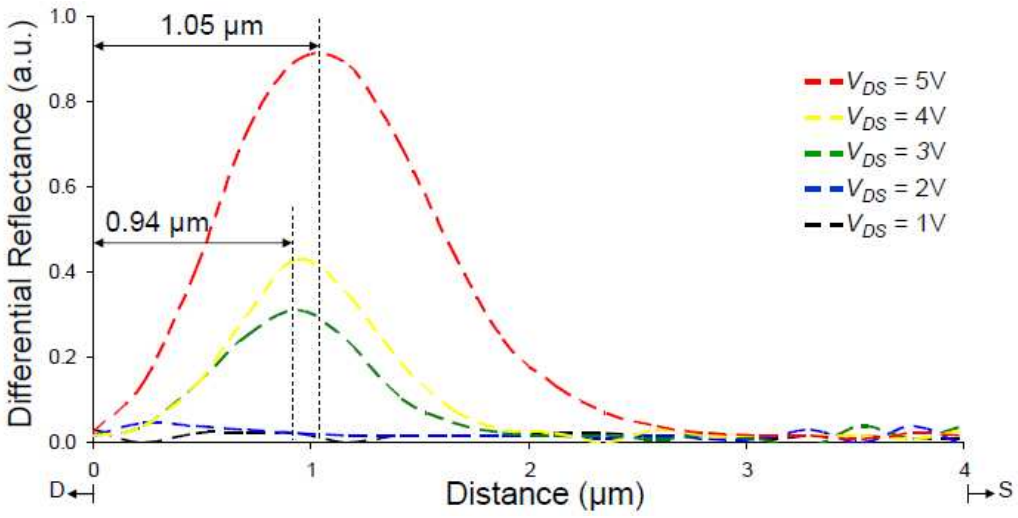

Fig. 7.13. Plot of channel YY' for NMOS transistor with L_{mask}=4 µm and V_{GS}=5V

It is expected when V_{GS} is reduced and the same set of V_{DS} bias is applied, the voltage drop across the *VSR* would be higher and the *VSR* would be wider due to a smaller V_{DSAT} value, resulting in larger reflectance modulations. Figure 7.14 shows the differential reflectance plot when V_{GS} is reduced to 3V at the same set of V_{DS} bias as in Figure 7.13.

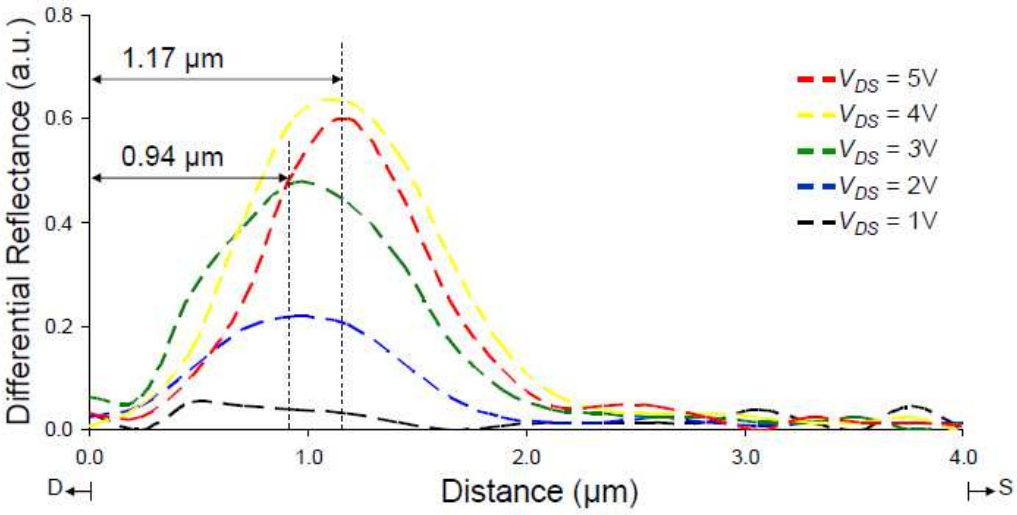

Fig. 7.14. Plot of channel YY' for NMOS transistor with L_{mask}=4 µm and V_{GS}=3V

A distinct peak is again observed when the NMOS transistor is in saturation mode at V_{DS} from 2V to 5V. ΔL_{peak} values at V_{DS}= 2V and 3V in Figure 7.14 are similar to those obtained in Figure 7.13 for V_{DS}= 3V and 4V. ΔL_{peak} at V_{DS}= 5V in Figure 7.14 is visibly larger than in Figure 7.13. This may be attributed to a wider *VSR* at V_{DS}= 5V when V_{GS}= 3V compared to V_{GS}= 5V. In Figure 7.14, V_{DS}= 4V is seen to have slightly larger differential reflectance than V_{DS}= 5V. This is unexpected and may be due to the saturation of E_m at these two bias points, with the anomalous differential reflectance due to experimental errors.

7.4 Variation of Channel Length

The reflectance modulations of NMOS transistors with L_{mask} = 2 µm and 4 µm at V_{GS}= 5V have been shown in Figures 7.7 and 7.13. In addition, an NMOS transistor from 0.18 µm process technology node with channel width *W*= 10 µm

and L_{mask}= 1.4 µm is backside prepared at a substrate thickness of 350 µm as shown in Figure 7.15.

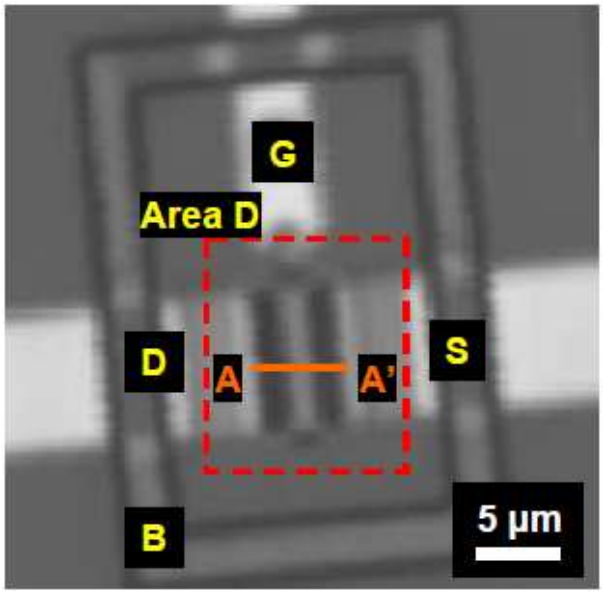

Fig. 7.15. NMOS transistor with L_{mask} = 1.4µm

The measured I_{DS}-V_{DS} characteristic of the NMOS transistor is shown in Figure 7.16. Since the channel length is the shortest among the three NMOS transistors, the I_{DS} saturation currents are largest compared to Figures 7.2 and 7.11. The V_{DSAT} values for the three transistors are similar. This allows meaningful comparison to be made for the dynamic laser reflectance modulation results at different channel lengths.

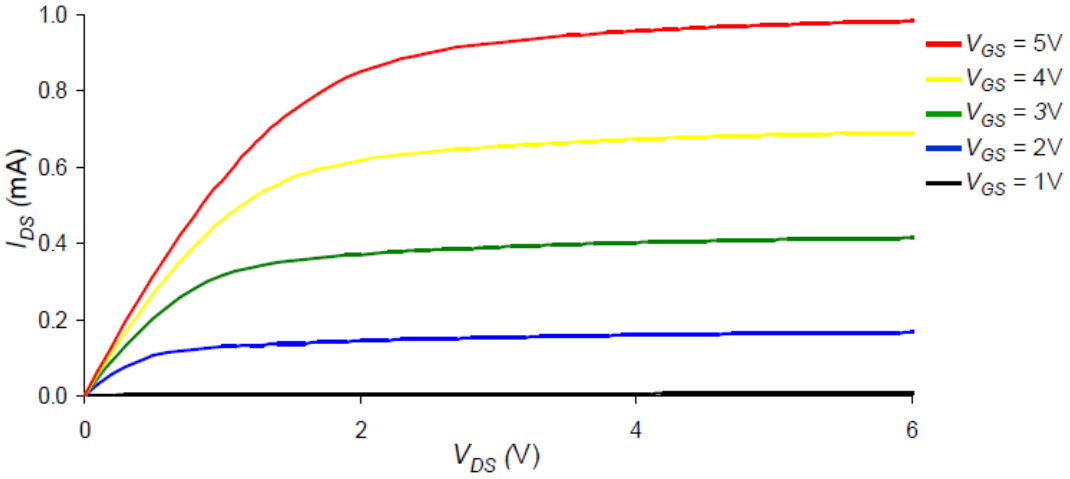

Fig. 7.16. The I_{DS}-V_{DS} characteristics of NMOS transistor with L_{mask}= 1.4 µm

Figure 7.17 shows the differential reflectance of the channel YY' at V_{GS}=5V and V_{DSAT}=2.4V for NMOS with L_{mask}=1.4 µm. A primary peak is similarly observed when the NMOS is in saturation mode. When V_{DS}= 3V, ΔL_{peak} is 0.22 µm. With increased V_{DS}, ΔL_{peak} moves towards the source. When V_{DS}= 5V, ΔL_{peak} is 0.38 µm. Compared to the NMOS transistor with L_{mask}= 2 µm in Figure 7.7, the secondary peak appears earlier when V_{DS} = 3V. This may be attributed to increased I_{DS} current at the shorter channel length which enables localized heating to be detected earlier.

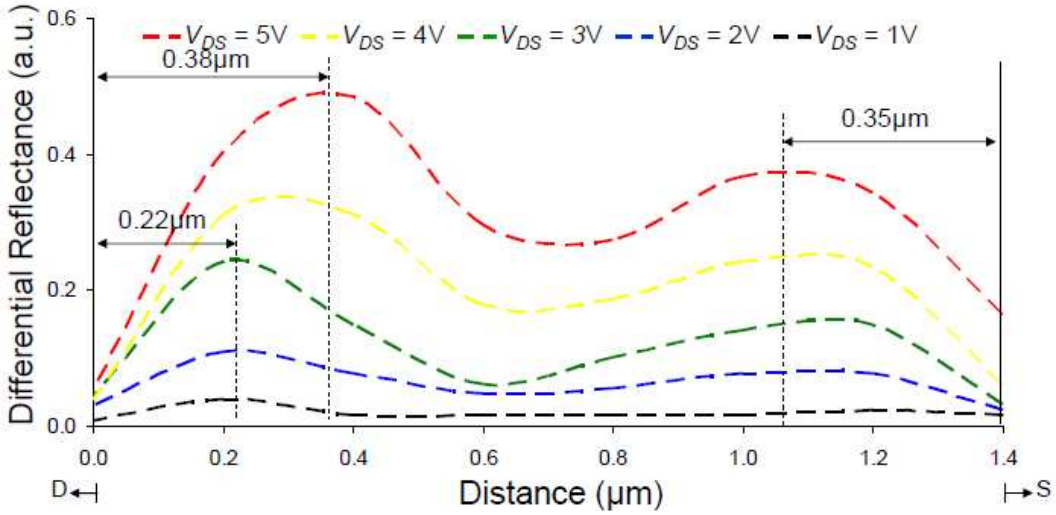

Fig. 7.17. Plot of channel YY' for NMOS transistor with L_{mask}=1.4 µm and V_{GS}=5V

7.5 Variation of MOS Types

A PMOS device with L_{mask}=1.4µm is studied and compared to NMOS device with similar L_{mask} dimension to determine the effect of the MOS type on dynamic reflectance modulation. Figure 7.18 shows the I_{DS}-V_{DS} characteristic of the PMOS transistor.

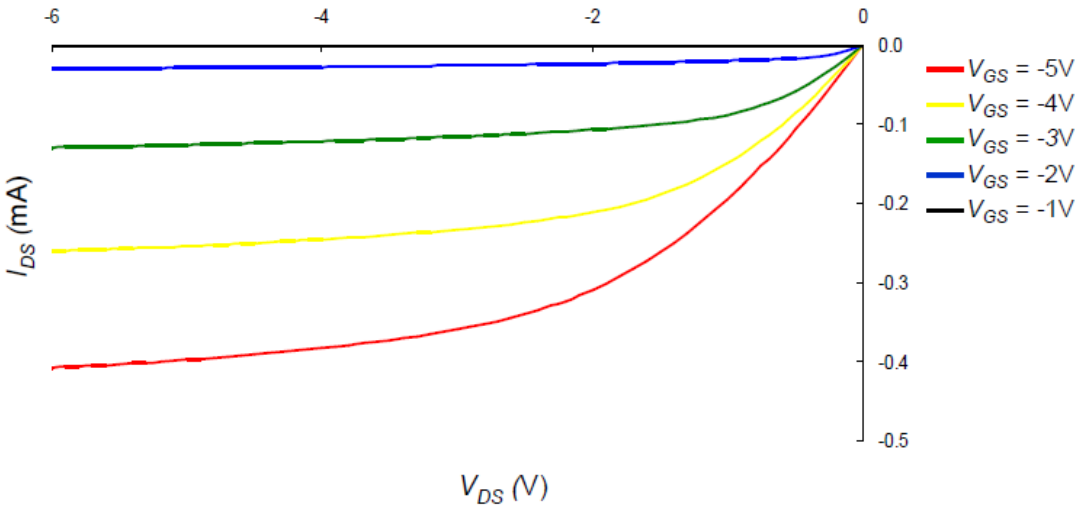

Fig. 7.18. The I_{DS}-V_{DS} characteristics of PMOS transistor with L_{mask}= 1.4 µm

The dynamic reflectance across the channel at V_{GS}= -3V and V_{DSAT}= -0.8V for the PMOS transistor is shown in Figure 7.19. A slight shift of the primary peak away from the drain-end is observed when V_{DS}≤ -2V. The PMOS transistor is in saturation when V_{DS}= -1.0V and -1.5V, but the primary peak was clearly absent. This may be due to weaker optical reflectivity changes at these bias points for PMOS transistors.

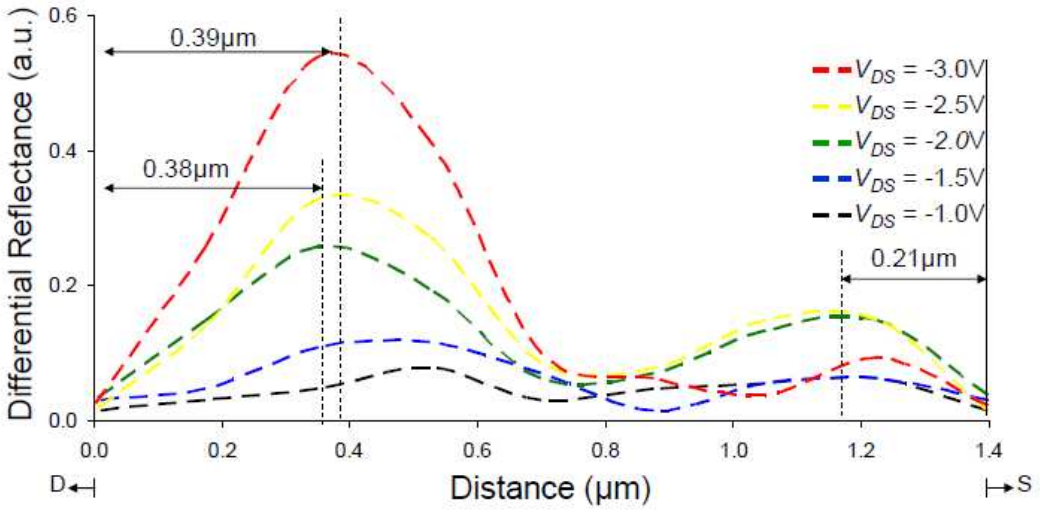

Fig. 7.19. Plot of channel YY' for PMOS transistor with L_{mask}=1.4 µm and V_{GS}= -3V

A secondary peak is also observed when V_{DS} ≤ -2V. Comparatively, the secondary peak in Figure 7.19 is significantly weaker. The I_{DS} current for the PMOS device is a fraction of those observed in Figures 7.7 and 7.17, and thus results in less severe localized heating.

7.6 Mask Channel Length Correction Factor

To compare the experimental results with the analytical model, it is necessary to make a distinction between L_{mask} and L_{eff} [97]. L_{mask} depends on the mask alignment and is optically measured using the SOM. L_{eff} is an electrical parameter that determines the electrical characteristics of the MOS transistor. It cannot be optically measured and is used in the analytical model as given by [58] which is used for the comparison. The relation between L_{mask} and L_{eff} is shown in Figure 7.20.

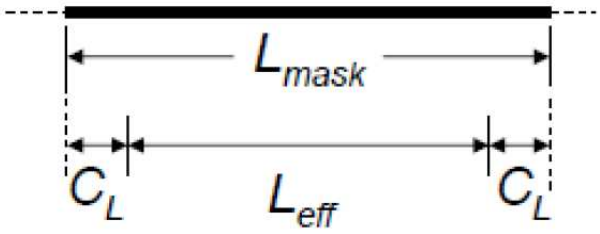

Fig. 7.20. Relation between L_{mask} and L_{eff} [97]

The correction factor is C_L. A proposed method to determine C_L is to plot the resistance of the channel against the mask channel length for each (V_{GS}–V_T). The resistance of the channel is approximately equal to $\frac{V_{DS}}{I_{DS}}$ and (V_{GS}–V_T) may be approximated by V_{GS} for simplicity. The intersection of the abscissa is twice the value of the correction factor, as shown in Figure 7.21 [56, 97].

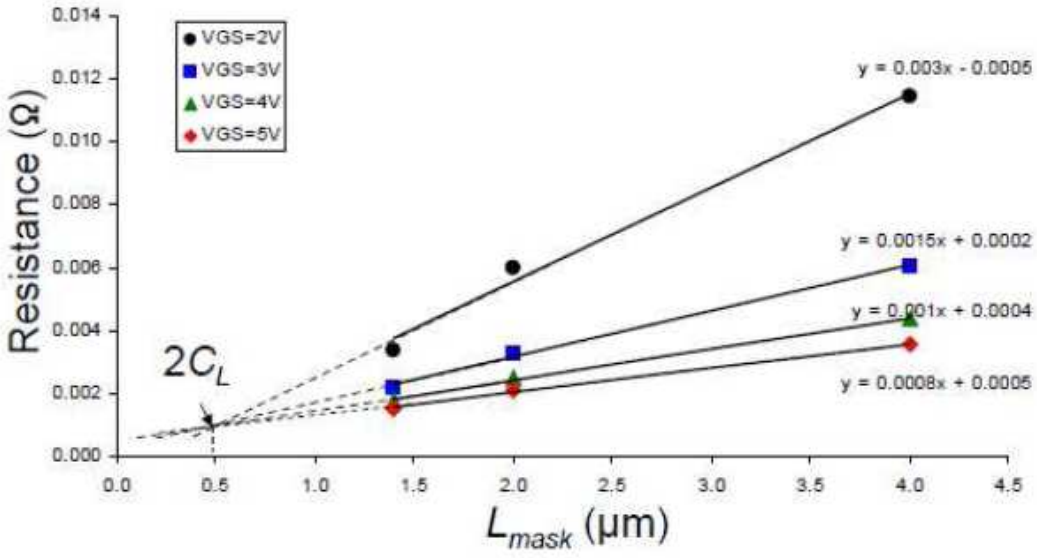

Fig. 7.21. Plot of resistance against L_{mask} for the determination of the correction factor

From the graph, the value of C_L is 0.25 µm and is constant for different mask channel lengths. The method suggests L_{mask} of 1 µm and 4 µm have L_{eff} values of 0.5 µm and 3.5 µm respectively. Figure 7.22 shows a plot of L_{eff} against L_{mask} using extracted empirical data from a table presented by Ko [58] where the correction factor varies with mask channel length.

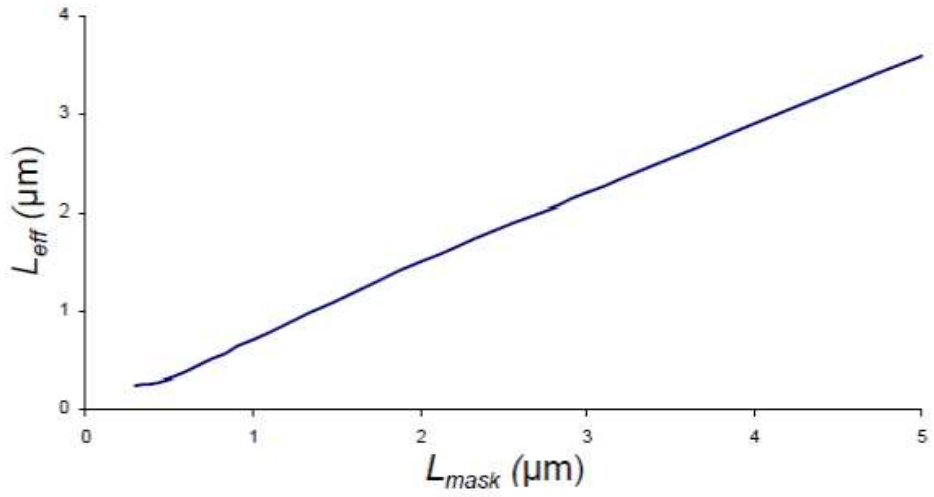

Fig. 7.22. Plot of L_{eff} against L_{mask}

From the graph, the slope of the graph is approximately 0.8, so that the value of C_L is 0.1 µm and 0.5 µm when L_{mask} is 1 µm and 5 µm respectively. The values for C_L suggested by Figure 7.22 are used in the correction of L_{mask} to L_{eff}, so that the analyses with the analytical model may be carried out.

7.7 Analyses

7.7.1 Same Channel Length, Different Gate Bias

For the NMOS transistor with L_{mask} value of 4 µm, the primary peak position at different V_{GS} bias is compared. The experimental ΔL_{eff} values are corrected from ΔL_{peak} values in Figures 7.13 and 7.14 using C_L obtained from Figure 7.22, and plotted in the same graph with values from the analytical model using Eq. 2.9, as shown in Figure 7.23. The value of the saturation electric field E_S for L_{mask}= 4 µm is assumed to be 10^3 Vcm^{-1}.

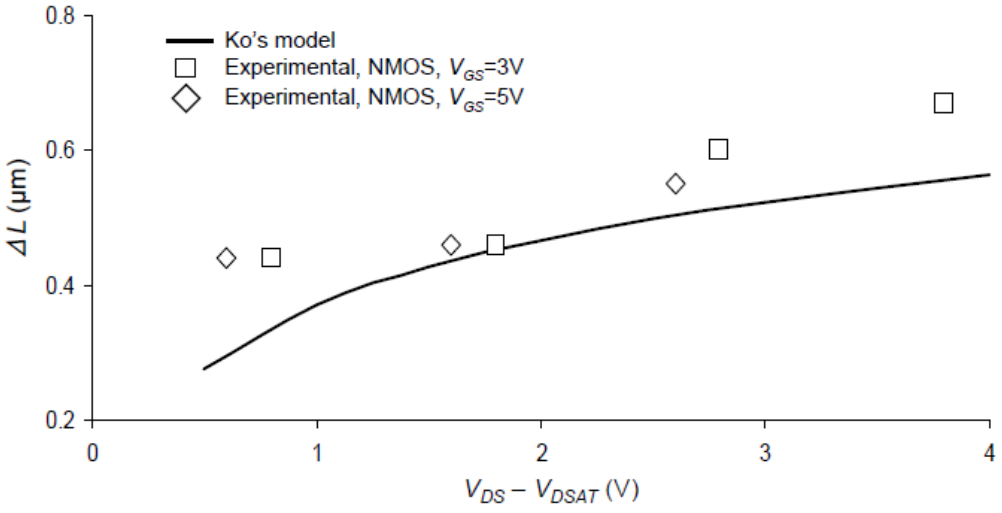

Fig. 7.23. Comparison of experimental peaks with analytical pinch-off point for NMOS transistor with L_{mask}= 4 µm and different V_{GS}

V_{DS}-V_{DSAT} is the voltage drop across the pinch-off region, with the V_{DSAT} values empirically determined from the I_{DS}-V_{DS} measurements. It accounts for the difference in V_{GS} which results in different V_{DSAT}, and allows a better comparison to be made between the experimental and analytical data. Within experimental

limits, the experimental data and analytical values agree well. Simulated values of ΔL_{Ko} increase with V_{DS}-V_{DSAT} as a result of *VSR* expansion. A similar trend is also observed for the experimental values of ΔL_{eff}. The consistency in trend is observed for ΔL_{eff} values at different V_{GS}. ΔL_{eff} correlates well with ΔL_{Ko}, suggesting the observed peak to be the pinch-off point.

7.7.2 Different Channel Length, Same Gate Bias

The primary peak position for NMOS transistors with L_{mask} values of 1.5 µm, 2.0 µm and 4.0 µm are compared for the same applied V_{GS} bias of 5V. ΔL_{eff} derived from the primary peaks in Figures 7.7, 7.13 and 7.17 are compared to analytical values in Figure 7.24.

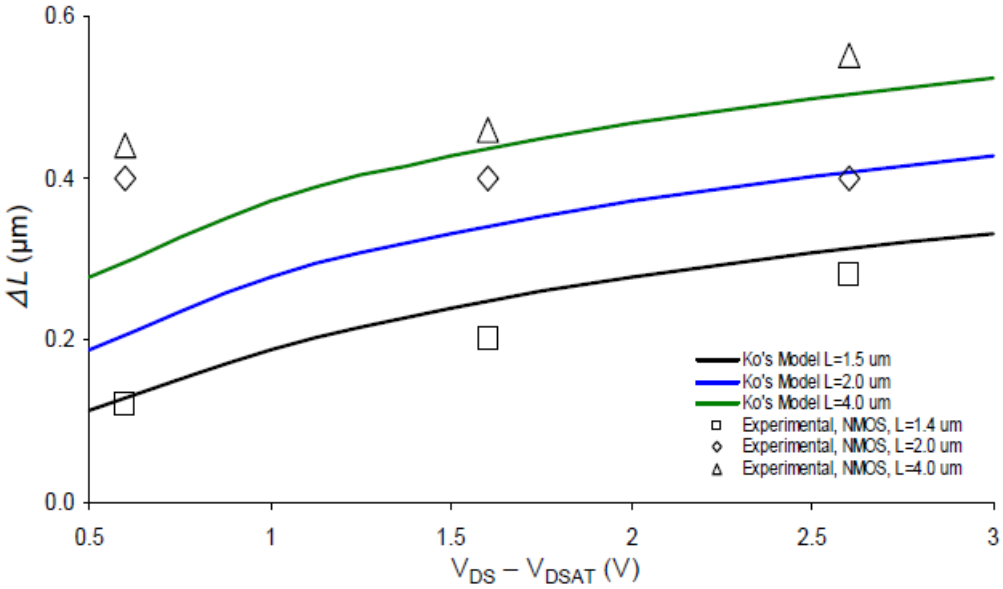

Fig. 7.24. Comparison of experimental peaks with analytical pinch-off point for NMOS transistors when V_{GS}=5V and different channel lengths

The analytical model shows ΔL increases with larger channel length as E_S is smaller due to a larger source section and the pinch-off point remaining at V_{DSAT}. The experimental values for different channel lengths follow the same trend and are in good agreement with the analytical model. As V_{DS}-V_{DSAT} increases, ΔL_{eff} increases, with the exception of the experimental data at L_{mask}= 2.0 µm where ΔL_{eff} remains as a constant at 0.4µm. This exception is reasonable within the experimental limits, although a smaller error delta is desired. In general, the same trend as shown in Figure 7.23 is observed. This study further supports the hypothesis that the observed primary peak is the pinch-off point.

7.7.3 Different MOS Types

ΔL_{eff} derived from NMOS and PMOS devices at L_{mask} =1.4 µm are plotted in the same graph with analytical values obtained using Ko's model, as shown in Figure 7.25. It is noted the analytical model makes no distinction between NMOS and PMOS transistors.

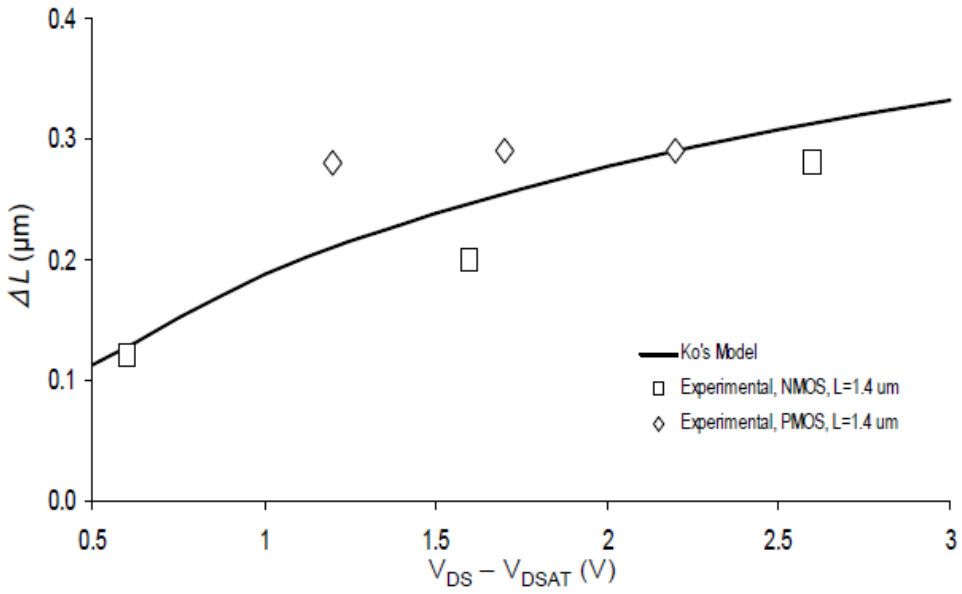

Fig. 7.25. Comparison of experimental peaks with analytical pinch-off point for NMOS and PMOS transistors at L_{mask} = 1.4 μm

The experimental data and simulation values agree well. The primary peak positions for different MOS types do not appear to differ significantly, further supporting the analytical model, and confirming the hypothesis that the primary peak is the pinch-off point.

7.8 Summary

Initial backside reflectance modulation studies based on static techniques are carried out to characterize the MOS channel. It is found that static techniques lack sensitivity. The dynamic technique employs lock-in amplification to enhance the sensitivity of the response, and is used for the characterization studies of the MOS channel.

Characterization of the MOS channel at different modes of operation is successfully carried out using dynamic backside laser reflectance modulation technique for variations in gate bias, channel length and MOS device type. The reflectance modulations are distinct at different operating modes, with a primary peak observed near the drain-end of the channel when the MOS devices are in saturation mode.

The Pseudo-Two-Dimensional Model is used to compare the length of the velocity saturation region with the experimental data based on the hypothesis that the primary peak is the pinch-off point. The experimental and analytical values are in good agreement and support the hypothesis that the primary peaks observed in dynamic reflectance modulation experiments is the pinch-off point.

Chapter 8 Failure Analysis Applications

Backside reflectance modulation techniques may be used to identify electrically-biased devices and defective metal lines to complement existing fault localization techniques. A high resolution and high sensitivity thermal probe may be realized to detect temperature variations. The techniques may also be used to characterize the operating modes of an MOS transistor to provide useful information about the functionality of the probed device.

8.1 Localization of Biased Device

As noted in Section 1.4, fault localization is a great challenge in FA [2] and is the most critical step since it sharply reduces the area for subsequent analyses [3]. The main passive technique is PEM and the main active techniques are based on SOM. When a device is electrically biased, reflectance modulations result from temperature and/or electro-optical effects. In Figure 6.5, sample #R2 is electrically biased, resulting in reflectance modulations due to temperature effect. The biased device can be easily identified from the rest in the differential reflectance modulation images.

In another illustration, an Intersil CA3083 general purpose, high current, bipolar junction transistor (BJT) array is backside prepared at a substrate thickness of 300 μm, and the reflected image at 20X is shown in Figure 8.1. Electrical bias is applied to the circled BJT transistor such that it is in the forward biased mode.

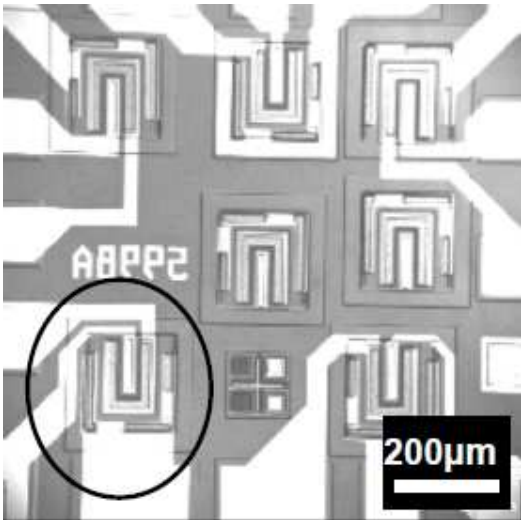

Fig. 8.1: Backside reflected image of BJT array

The backside reflectance modulations are measured using the static technique with CW light source at an electrical bias of 36, 79 and 120mW respectively. In this comparison, the reflectance modulations are measured with objective lens at 20X and 50X magnifications, and the differential reflectance modulation images are shown respectively in the left and right columns of Figure 8.2.

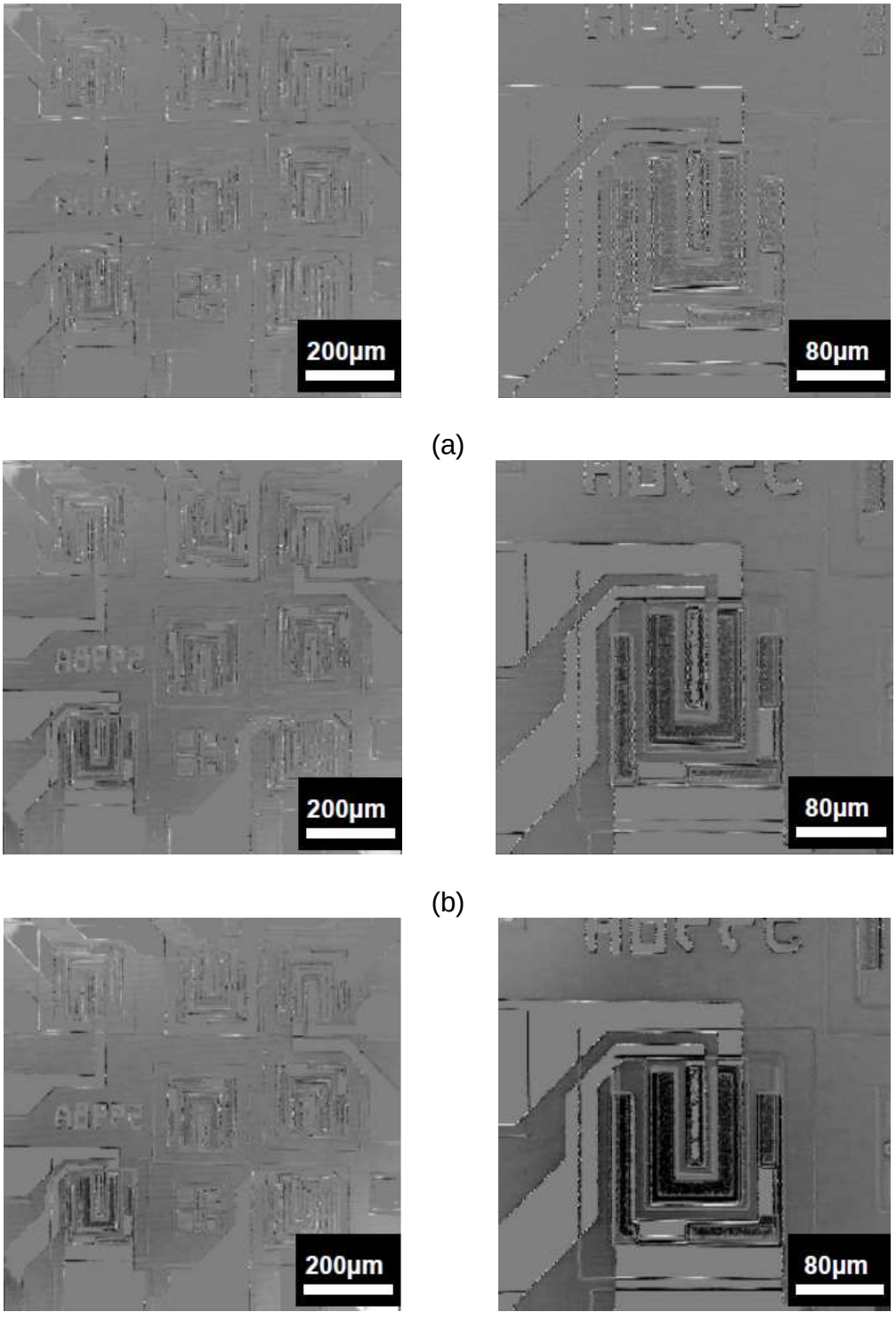

Fig. 8.2: Differential reflectance modulation images of BJT transistor at an electrical bias of (a) 36 mW, (b) 79 mW and (c) 120 mW

As the electrical bias increases, the biased BJT transistor becomes significantly darker compared to the rest of the unbiased BJT transistor, and may be identified. The reflectance modulations result from electro-optical and temperature effects.

Hence, the reflectance modulation techniques may be applied to the localization of electrically biased devices and used to complement the existing fault localization techniques on the SOM system.

8.2 Identification of Defective Metal Lines on Solar Modules

A prototype monocrystalline solar module, as shown in Figure 8.3a, is used. Electrical bias is applied across V_{b+} and V_{b-}. One metallic finger is cut at both ends as seen in Figure 8.3b for the topview drawing of the device, and is termed "Bad" since it is not electrically connected.

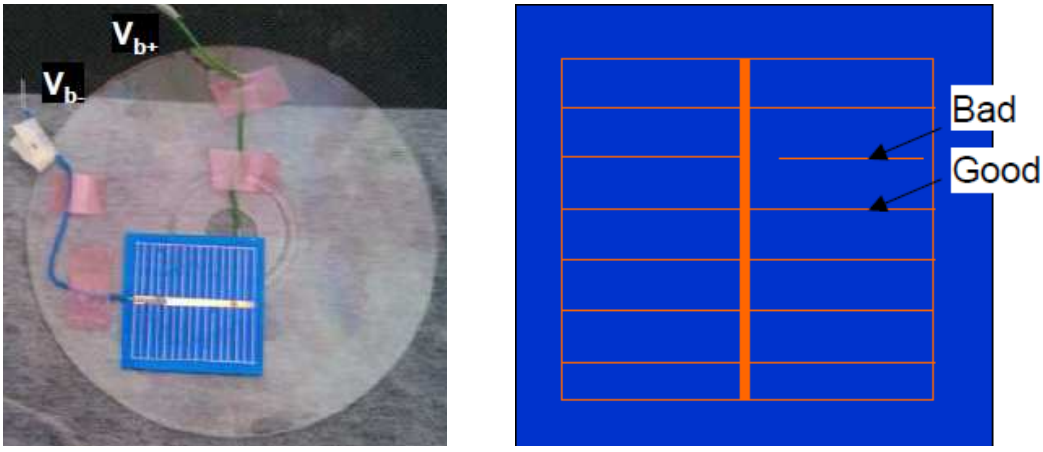

(a) (b)

Fig. 8.3: (a) Image of prototype solar module, and (b) topview drawing

The frontside reflectance modulations of good and bad metallic fingers at the forward and reverse bias are measured using the static technique. The differential reflectance modulations are transformed in pseudo-rainbow colors where the red areas represent significant reflectance modulation and the blue areas represent negligible reflectance modulation. The left column of Figure 8.4 is for the good metallic finger and the right column is for the bad metallic finger. In Figure 8.4a, the solar module is forward biased at 0.6 V and draws 89 mA. In Figure 8.4b, the solar module is reversed biased at -6 V and draws -13 mA.

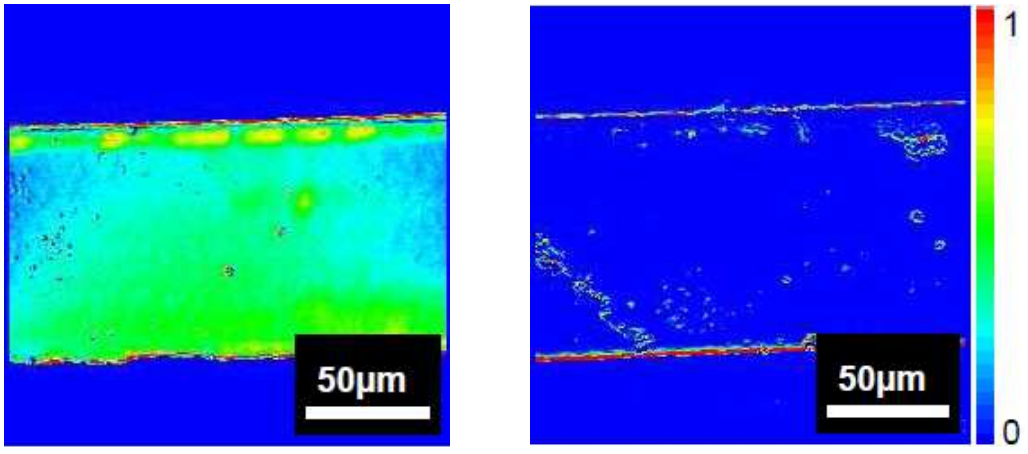

(a)

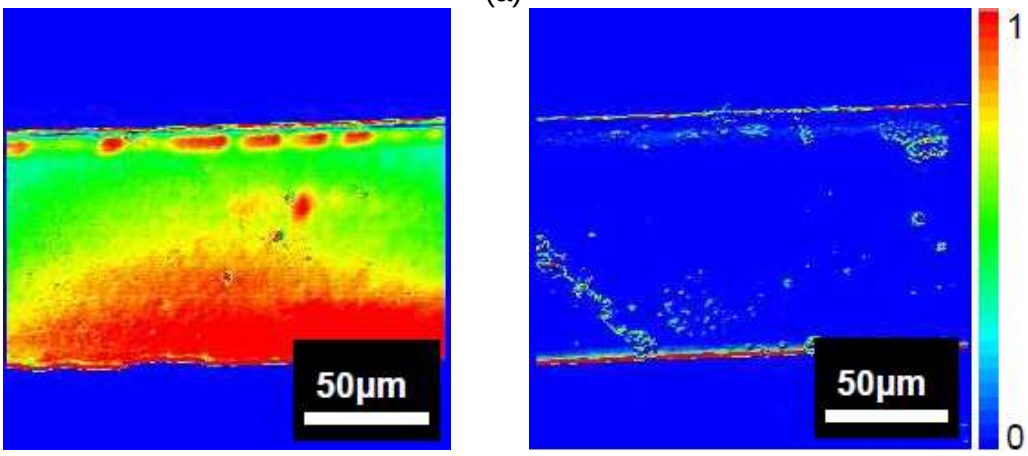

(b)

Fig. 8.4: Frontside reflectance modulations at (a) forward and (b) reversed bias for good and bad metallic fingers transformed in pseudo-color images

The reflectance modulations at the forward and reverse bias for the good metallic finger are significantly different from the results for the bad metallic finger. For the bad metallic finger, there is negligible reflectance modulation for both the forward and reverse bias, except at the edges which are due to false edge effects. Without calibrations and further quantifications of the reflectance modulation results, this example highlights a simple technique to detect defective metal lines, and may be extended to identify defective microscale metal lines using either frontside or backside reflectance modulation techniques.

8.3 Non-Invasive, High Resolution and High Sensitivity Backside Thermal Probe

Backside reflectance modulation maps correlating to the thermal maps of interested areas in a microelectronic device may be generated as shown in Figure 6.5. Similarly, the temperature variation on microscale metal thin films may be measured as shown in Figures 6.6 and 6.8. Thus, the backside laser reflectance modulation techniques can be used to implement a high resolution and high sensitivity thermal probe which is non-invasive.

For illustration, a thermal sensor chip is backside prepared at a substrate thickness of 100 µm. It is essentially a resistor that heats up by an electrical bias, and an adjacent diode to sense the temperature variation. The backside reflected image is shown in Figure 8.5.

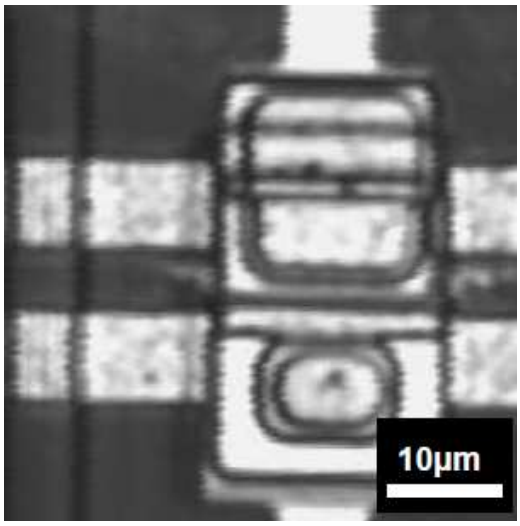

Fig. 8.5: Backside reflected image of a thermal sensor chip

The backside reflectance modulations using the static technique of the thermal sensor chip are transformed in pseudo-rainbow colors and shown in Figure 8.6. At the electrical bias of 30, 90 and 120 mA, the temperature change is measured to be 2.4, 32.4 and 53.3 K respectively. The red areas represent significant temperature change and the blue areas represent little temperature change.

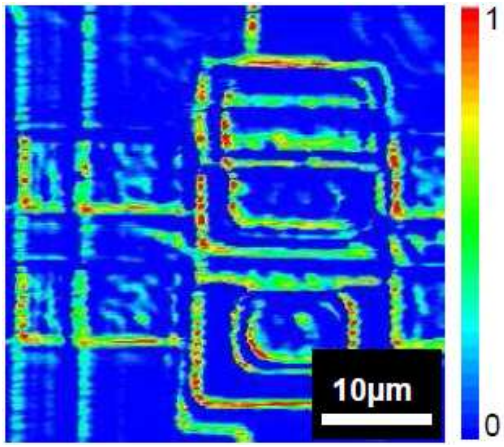

(a)

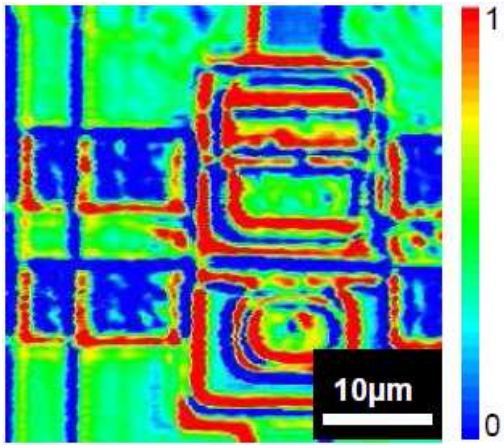

(b)

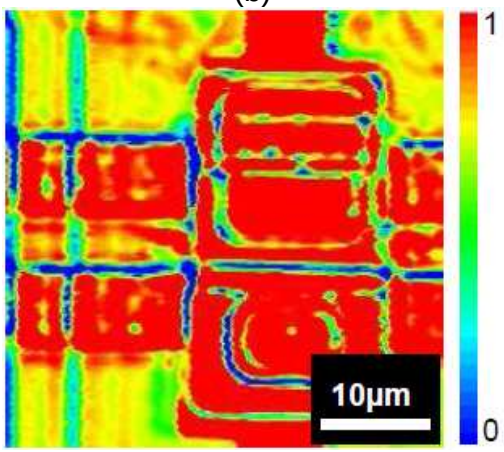

(c)

Fig. 8.6: Backside reflectance modulation transformed in the pseudo-color images of thermal sensor chip at a temperature change of (a) 2.4, (b) 32.4 and (c) 53.3 K

As the electrical bias increases, the reflectance modulation on the thermal sensor chip becomes significantly larger than the rest. The substrate is observed to heat up at an increased electrical bias. In this example, significant false edge effects are observed which may be mitigated with the dynamic technique.

For another illustration, a backside prepared microelectronic device with a known power-short condition is used to compare static backside thermoreflectance modulation technique with TIVA. The substrate thickness is also 100 µm. The sample is electrically biased at 40 mW, with most of the heat dissipation at the defective site. Figure 8.7a shows the defective location overlayed on the reflected image using TIVA. Figure 8.7b shows the defective location overlayed on the reflected image using the static backside thermoreflectance modulation technique.

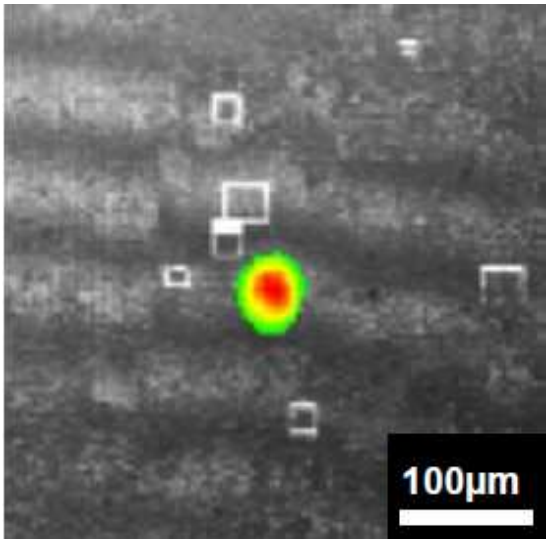

(a)

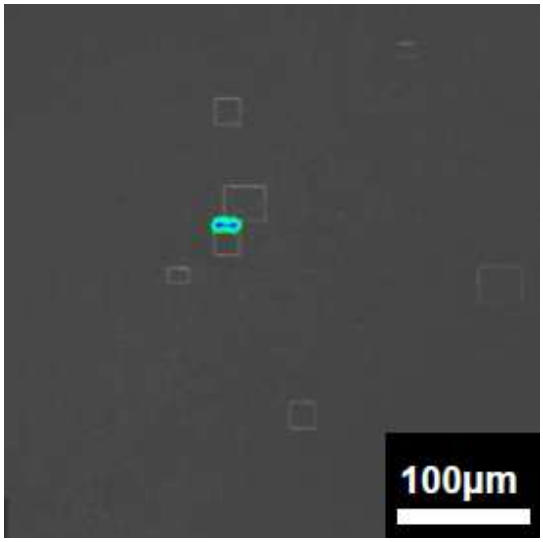

(b)

Fig. 8.7: Identified defective location of power short overlayed on reflected image using (a) TIVA, and (b) static backside thermoreflectance technique

The application of TIVA in locating power shorts has been commonly used in the FA industry [98, 99]. As seen in Figure 8.7, the identified defective location using the static backside thermoreflectance technique differs by less than 30 µm from the identified defective location using TIVA. The precise defective location is not confirmed.

This section highlights the possibility of applying backside reflectance modulation techniques to realize a high resolution and high sensitivity thermal probe that is non-invasive. The system has a spatial resolution of 1 µm and thermal sensitivity better than 100 mK. With the use of a SIL lens, the spatial resolution may be improved to 200-250 nm.

8.4 Non-Invasive, High Resolution and High Sensitivity Backside Probe for Characterizing MOS Devices

As seen in Chapter 7, the channel of an MOS transistor may be characterized with the dynamic backside reflectance modulation technique. The dominant peak location of the differential reflectance image in the MOS channel is observed to correspond to the pinch-off point. This presents a novel and powerful technique to characterize the functionality of an MOS device.

For minimal sized transistors based on the cutting edge technologies of 22, 32 and 45 nm processes, the dominant peak location may not be discerned due to the lack of spatial resolution, even with the use of a SIL lens. However, at a spatial resolution of 200-250 nm, it is possible to isolate a single transistor, and to determine the reflectance modulations of the transistor. Since the reflectance modulations of the linear, pinch-off and saturation modes differ, the reflectance modulations would provide similar characterizations. The use of the backside reflectance modulation techniques to characterize the operating modes of MOS transistors is promising in its application as a new complementary FA technique to the existing LVP, PDP and LTP techniques.

8.5 Summary

This chapter presents four novel applications of backside laser reflectance modulation techniques. The localization of defects is a key step in FA. It is possible to use reflectance modulations to identify electrically biased devices. It

is also possible to use reflectance modulations to identify defective metal lines based on its reflectance modulations. These two applications complement existing fault localization techniques. It is very easy to incorporate these two new applications into the existing SOM systems without significant system modifications.

With power management becoming an important topic in IC design, backside reflectance modulation techniques may be applied as a high resolution and high sensitivity thermal probe which is non-invasive to address these concerns. Thermal maps may be generated and temperature variation of microscale metal lines can be measured. Since the laser beam has no physical contacts to the probed devices, its invasiveness is mitigated.

The operating modes for MOS transistors may also be characterized with the backside reflectance modulation techniques. This provides useful information to understand the functionality of the probed MOS devices, and may be used as complementary tool to the existing LVP, PDP and LTP techniques.

Chapter 9 Conclusions and Future Works

This chapter concludes the dissertation with a summary and suggestions for future work in this area.

9.1 Conclusions

This research aims to understand the physics governing reflectance modulation and to develop novel backside characterization techniques based on these parameters. An in-depth understanding of the interaction between the probe laser beam with the probed device is important for the development of new applications. Literature review and theoretical modeling have identified temperature and electro-optical effects as key parameters in reflectance physics.

The first of this thesis focuses on understanding the physics of backside reflectance modulation due to temperature effect. Backside reflectance modulation is found to have better sensitivity compared to frontside reflectance modulation as the silicon substrate of commercial devices are lightly to moderately doped and results in additional reflectance modulation due to the absorption of the substrate.

Preliminary investigations were carried out using large resistive structures that have been backside prepared. Experimental studies were carried out on coherent versus non-coherent light source, probe beam power and sample tilt.

Other studies have been less fruitful. The results allow the experimental setup and experimentation technique to be fine-tuned.

A series of backside reflectance modulation results were obtained for microscale metal interconnects with variation in applied electrical bias, dimension, and substrate thickness. The reflectance intensities are observed to modulate negatively with electrical bias for the case when the absorption coefficient of the backside Si substrate varies significantly with temperature compared to the reflectance. In this case, the reflectance and thermoreflectance coefficients are one to two orders of magnitude larger than the values for frontside measurements or when the Si substrate is undoped.

A backside reflectance model is developed and is found to agree well with experimental data. The reflected intensity modulation with electrical bias depends on the reflectance, absorption coefficient and substrate thickness. Positive or negative reflected intensity modulation depends on whether the modulation is due primarily to the temperature variation of the absorption coefficient or the reflectance.

Temperature variation of the probed metal line at different electrical biases can be determined from its reflectance modulations. Likewise, two-dimensional thermal maps can be generated. This makes it possible to apply the backside

laser reflectance modulation technique as a high resolution and high sensitivity thermal probe.

The second part of the thesis attempts to understand the reflectance modulations of active devices. A set of NMOS and PMOS transistors from the 0.18 µm process technology node are backside prepared at a substrate thickness of 350 µm. Sensitivity studies of static and dynamic backside reflectance modulations indicated the static technique do not have enough sensitivity. Characterization of the MOS channel at different operating modes has been successfully carried out using dynamic backside reflectance modulation technique for variations in gate bias, channel lengths and MOS device types.

The reflectance modulations are distinct at different operating modes, with a primary peak observed near the drain-end of the channel when the MOS devices are in saturation mode. The Pseudo-Two-Dimensional Model is used to compare the length of the velocity saturation region with the experimental data based on the hypothesis that the primary peak is the pinch-off point. The experimental and analytical values are in good agreement and supports the hypothesis that the primary peaks observed in dynamic reflectance modulation experiments is the pinch-off point.

The backside reflectance modulation technique is able to characterize the MOS device operations. The results present a novel and powerful technique to

characterize the functionality of MOS devices, in addition to the determination of its timing information, and may be used as a new complementary FA technique to existing LVP, PDP and LTP techniques.

Two additional applications of backside reflectance modulation techniques in locating electrically biased devices and identifying defective metal lines have been proposed in Chapter 8.

9.2 Recommendations for Future Work

Some recommendations for future research efforts in the area of reflectance modulation physics are suggested in this section.

9.2.1 Reflectance Modulations of Operating Modes for Minimal-sized Transistors

Even with the use of a SIL lens, the dominant peak locations of minimal-sized transistors may not be discerned due to the lack of spatial resolution. However, at a spatial resolution of 200-250 nm, it is possible to isolate a single transistor, and to determine the reflectance modulations of that transistor only. Since the reflectance modulations of the linear, pinch-off and saturation modes have distinct signatures as noted in Chapter 7, the reflectance modulations would enable similar characterizations to be made. In addition to obtaining reflectance

modulation results for NMOS and PMOS, the reflectance modulations of CMOS devices are of great interests to key players in the FA industry.

9.2.2 Temperature Effect of Reflectance Modulation at Different Substrate Doping

The impurity doping concentration of the substrate affects the absorption of the substrate, as discussed in Section 2.1.2. Most empirical studies to determine the absorption coefficient and refractive index for free carrier concentrations are carried out at a constant temperature, as seen in Chapter 2. The empirical data on the temperature dependence of reflectance modulations at different substrate doping may provide new insights into the physical mechanisms, in addition to the simple thermal response model proposed by PJ Chernek and JA Orson.

9.2.3 Dynamic Reflectance Modulation using Pulsed Light Source

The proposed dynamic technique in this dissertation and the experimentations carried out has been limited to using CW light source. With pulsing, the probe beam power may be further reduced to mitigate its invasiveness. It may be varied with the duty cycle of the pulse width. Proper design of the experimentation should have improved thermal sensitivity with no significant signal degradation.

9.2.4 Reflectance Modulations at different incident wavelengths

The investigation and characterization of reflectance modulations due to temperature and electro-optical effects in silicon integrated circuits for this dissertation has been confined to an incident wavelength of 1.34 µm. As discussed in Section 2.1.1, the physical mechanisms varied with different incident photon energy. Repeating the experiments at an incident laser wavelength of 1.064 µm would further substantiate the works presented in this dissertation.

List of Publications

The research presented in this dissertation has resulted in two journal papers and two conference papers as follows:

1. Teo JKJ, Chua CM, Koh LS, Phang JCH, “Optical Characterization of MOS Transistors using Dynamic Backside Reflectance Modulation Technique”, Intl. Symp. Test & FA (ISTFA), No. 6.5, pp. 170-175, 2011.

2. Teo JKJ, Chua CM, Koh LS, Phang JCH, “NMOS Characterization with Static and Dynamic Backside Laser Reflectance Modulation Techniques”, Appl. Phys. Lett. Vol. 99, No. 9, 2011.

3. Teo JKJ, Chua CM, Koh LS, Phang JCH, “Negative Backside Thermoreflectance Modulation of Microscale Metal Interconnects”, Electron. Lett. Vol. 47, No. 14, pp. 821-822, 2011.

4. Teo JKJ, Chua CM, Koh LS, Phang JCH, “Backside Reflectance Modulation of Microscale Metal Interconnects”, International Reliability Physics Symposium (IRPS), FA-4, pp. 780-785, 2011.

References

1. Kudva SM, Clark R, Vallet DP, Ross D, Hasegawa T, Gilfeather G, Thayer M, Pabbisetty S, Shreeve R, Ash B, Serpiello J, Huffman K, Wagner L, and Kazmi S, "The SEMATECH Failure Analysis Roadmap," *Intl. Symp. Test & FA (ISTFA 1995)*, pp. 1-5, 1995.
2. Vallet DP, "Why Waste Time on Roadmaps When We Don't Have Cars," *IEEE Trans. Dev. Matl. Reliab.*, Vol. 7, No. 1, pp. 5-10, 2007.
3. Vallet DP, "Probing the Future of Failure Analysis," *Electron. Dev. FA (EDFA 2002)*, Vol. 4, No. 4, pp. 5-9, 2002.
4. Phang JCH, Chan DSH, Tan SL, Len WB, Yim KH, Koh LS, Chua CM, and Balk LJ, "A Review of Near Infrared Photon Emission Microscopy and Spectroscopy," *IEEE Intl. Symp. Phys. & FA (IPFA 2005)*, pp. 275-281, 2005.
5. Bruce MR and Bruce VJ, "ABC's of Photon Emission Microscopy," *Electron. Dev. FA (EDFA 2003)*, Vol. 5, No. 3, pp. 13-20, 2003.
6. Phang JCH, Chan DSH, Palaniappan M, Chin JM, Davis B, Bruce M, Wilcox J, Gilfeather G, Chua CM, Koh LS, Ng HY, and Tan SH, "A Review of Laser Induced Techniques for Microelectronic Failure Analysis," *IEEE Intl. Symp. Phys. & FA (IPFA 2004)*, pp. 255-261, 2004.
7. Phang JCH, "Passive Localization Techniques: Physics, Instrumentation, and Other Issues," *Electron. Dev. FA (EDFA 2004)*, Vol. 5, No. 4, pp. 52, 2004.
8. Beaudoin F, Imbert G, Perdu P, and Trocque C, "Current Leakage Fault Localization Using Backside OBIRCH," *IEEE Intl. Symp. Phys. & FA (IPFA 2001)*, pp. 121-125, 2001.
9. Cole EI, Tangyunyong P, Benson DA, and Barton DL, "TIVA and SEI Developments for Enhanced Front and Backside Interconnection Failure Analysis," *Proc. Eur. Symp. Rel. Electron. Devices, Failure Phys. & Analysis (ESREF 1999)*, pp. 991-996, 1999.
10. Palaniappan M, Chin JM, Davis B, Bruce M, Wilcox J, Chua CM, Koh LS, Ng HY, Tan SH, Phang JCH, and Gilfeather G, "New Signal Detection Methods for Thermal Beam Induced Phenomenon," *Proc. Intl. Symp. Testing & FA (ISTFA 2001)*, pp. 171-177, 2001.
11. Quah ACT, Koh LS, Chua CM, Palaniappan M, Chin JM, and Phang JCH, "DC-Coupled Laser Induced Detection System for Fault Localization in Microelectronic Failure Analysis," *Proc. Intl. Symp. Phys. & FA (IPFA 2006)*, pp. 327-332, 2006.
12. Kohno Y, Shimizu M, Kitamura K, Nishikawa A, Odani C, and Miura N, "Laser beam carrier injection technique for CMOS LSI failure analysis using an OBIC: light-induced state transition (LIST) method"," *Proc. IEEE Intl. Symp. Semicon. Manufacturing*, pp. E57-E60, 1997.
13. Chin JM, Phang JCH, Chan DSH, Soh CE, and Gilfeather G, "Single Contact Optical Beam Induced Currents (SCOBIC) - A New Failure Analysis Technique," *Proc. Intl. Rel. Phys. Symp. (IRPS 2000)*, pp. 420-424, 2000.
14. Cole EI, Soden JM, Rife JL, Barton DL, and Henderson CL, "Novel Failure Analysis Techniques using Photon Probing with a Scanning Optical Microscope," *Proc. Intl. Rel. Phys. Symp. (IRPS 1994)*, pp. 388-398, 1994.

15. Bruce MR, Bruce VJ, Prejean S, and Huynh J, "Failure Analysis Turned Upside Down: A Review of Backside Analysis Techniques," *Electron. Dev. FA (EDFA 2003),* Vol. 5, No. 4, pp. 13-24, 2003.
16. Hechtl M, Steckert G, and Keller C, "Localization of Electrical Shorts in Dies and Packages using Magnetic Microscopy and Lock-in-IR Thermography," *Proc. Intl. Symp. Phys. & FA (IPFA 2006),* pp. 252-255, 2001.
17. Aw SE, Tan HS, and Ong CK, "Optical absorption measurements of band-gap shrinkage in moderately and heavily doped silicon," *J. Phys.Cond. Matt.,* Vol. 3, No. 42, pp. 8213-8223, 1991.
18. (ITRS) International Technology Roadmap for Semiconductors, "Roadmap - System Drivers," 2009.
19. Goh SH, Quah ACT, Sheppard CJR, Chua CM, Koh LS, and Phang JCH, "Effect of Refractive Solid Immersion Lens Parameters on the Enhancement of Laser Induced Fault Localization Techniques," *IEEE Proc. FA Symp. (IPFA 2008),* pp. 20, 2008.
20. Boit C, "Can failure analysis keep pace with IC technology development," *Proc. Intl. Symp. Phys. & FA (IPFA 1999),* pp. 9-14, 1999.
21. Moore GE, "Cramming more components onto integrated circuits," *Electronics,* Vol. 38, No. 8, 1965.
22. Yao LB, "NUS EE5518 VLSI Digital Circuit Design Lecture Notes," 2007.
23. Heinrich HK, "A noninvasive optical probe for detecting electrical signals in silicon integrated circuits," PhD Dissertation, Stanford University, California, USA, 1987.
24. Wagner LC, *Failure Analysis of Integrated Circuits - Tools and Techniques.* Boston, Kluwer Academic Publishers, 1999.
25. Vallet DP, "Picosecond Imaging Circuit Analysis - PICA," *Microelectron. FA: Desk Ref Fifth Ed,* pp. 369-377, **2004**.
26. Tsang JC and Kash JA, "Picosecond hot electron light emission from submicron complementary metal-oxide-semiconductor circuits," *Appl. Phys. Lett.,* pp. 889, 1997.
27. Tsang JC, Kash JA, and Vallet DP, "Time-resolved Optical Characterization of Electrical Activity in Integrated Circuits," *Proc. IEEE,* Vol. 88, No. 9, pp. 1440-1459, 2000.
28. Eiles TM, Woods GL, and Rao V, "Optical Probing of VLSI IC's from the Silicon Backside," *Proc. Intl. Symp. Testing & FA (ISTFA 1999),* pp. 27, 1999.
29. Rabaey JM, Chandrakasan A, and Nikolic B, *Digital Integrated Circuits - A Design Perspective,* 2nd ed. New Jersey, Prentice Hall, 2003.
30. Lian Y, "NUS EE5518 VLSI Digital Circuit Design Lecture Notes," 2007.
31. Martin G, "A Power and Energy Perspective on MultiProcessors," in *Designing Embedded Processors,* J. Henkel and S. Parameswaran, Eds., Springer, 2007.
32. . *XenIC InSb Camera Datasheet*. Available: http:/www.adept.net.au/cameras/XenICs/XMID-640.shtml
33. Claeys W, Dilhaire S, Jorez Sebestien, and Patino-Lopez L, "Laser probes for the thermal and thermomechanical characterisation of microelectronic devices," *Microelectronics J.,* Vol. 32, pp. 891-898, 2001.

34. Ju YS and Goodson KE, "Short-Time-Scale Thermal Mapping of Microdevices Using a Scanning Thermoreflectance Technique," *Trans. ASME,* Vol. 120, pp. 306-313, 1998.
35. Tessier G, Polignano M-L, Pavageau S, Filloy C, Fournier D, Cerutti F, and Mica I, "Thermoreflectance Temperature Imaging of Integrated Circuits: Calibration Technique and Quantitative Comparison with Integrated Sensors and Simulations," *J. Phys. D: Appl. Phys.,* Vol. 39, pp. 4159-4166, 2006.
36. Hecht E, *Optics 4th ed.,* Addison Wesley, pp. 407-408, 2002.
37. Freeman MH and Hull CC, *Optics*, 11th ed., Elsevier, 2003.
38. Schroder DK, Thomas RN, and Swartz JC, "Free Carrier Absorption In Silicon," *IEEE Trans. Electron Dev.,* Vol. ED-25, No. 2, pp. 254-261, 1978.
39. Archer RJ, Koyama RY, Loebner EE, and Lucas RC, "Optical Absorption, Electroluminescence, and the Band Gap of BP," *Phys. Rev. Lett,* Vol. 12, No. 19, pp. 538-540, 1964.
40. Kittel C, *Introduction to Solid State Physics*, 8th ed., Wiley, pp. 100, 2005.
41. Falk RA, "Near IR Absorption in Heavily Doped Si -- An Empirical Approach," *Proc. Intl. Symp. Testing & FA (ISTFA 2000),* pp. 121-127, 2000.
42. Spitzer W and Fan HY, "InfraRed Absorption in n-type Si," *Phy. Rev.,* Vol. 108, No. 2, pp. 268-271, 1957.
43. Barta E, "Optical Constants of Heavily Doped p- and n-type Si," *Infrared Phys,* Vol. 17, pp. 319, 1977.
44. Soref RA and Bennett BR, "Electro-optical Effects in Silicon," *IEEE J. Quantum Elec.,* Vol. QE-23, No. 1, pp. 123-129, 1987.
45. Chernek PJ and Orson JA, "A Simple Thermal Response Model for a p-doped Silicon Substrate Irradiated by 1.06 and 1.32 Micron Lasers," *Proc. SPIE,* Vol. 4679, pp. 186-197, 2002.
46. Denk W, Strickler JH, and Webb WW, "Two-photon laser scanning fluorescence microscopy," *Science,* Vol. 248, No. 4951, pp. 73-76, 1990.
47. Franz W, "Einfluss eines elektrischen Feldes auf eine optische Absorptions-kante," *Z. Naturforschung,* Vol. 13a, pp. 484-489, 1958.
48. Keldysh LV, "The effect of a strong electric field on the optical properties of insulating crystals," *Soviet Phys. JETP*, Vol. 7, pp. 788-790, 1958.
49. Wendland PH and Chester M, "Electric Field Effects on Indirect Optical Transitions in Silicon," *Phy. Rev.,* Vol. 140, No. 4A, pp. A1384-A1390, 1965.
50. Frova A and Handler P, "Direct Observation of Phonons in Silicon by Electric Field Modulated Optical Absorption," *Phy. Rev. Lett.,* Vol. 14, No. 6, pp. 178-180, 1965.
51. Jellison GE Jr and Modine FA, "Optical functions of silicon at elevated temperature," *J. Appl. Phys.,* Vol. 76, pp. 3758, 1994.
52. Pierret RF, *Semiconductor Device Fundamentals,* Addison Wesley, 1996.
53. Sze SM, *Physics of Semiconductor Devices*, 2nd ed. New York, Wiley, pp. 431-480, 1986.
54. Vasileska D, "EE 531 Lecture Notes," Arizona State University.
55. Reddi VGK and Sah CT, "Source to Drain Resistance beyond Pinch-off in MOS Transistor," *IEEE Trans. Electron Dev.,* Vol. ED-12, pp. 139-141, 1965.

56. Muller RS and Kamins TI, *Device Electronics for Integrated Circuits*, 2nd ed. New York, Wiley, pp. 491, 1986.
57. Ostermeir R, Brunner K, Abstreiter G, and Weber W, "Temperature Distribution in Si-MOSFET's studied by Micro Raman Spectroscopy," *IEEE Trans. Electron Dev.*, Vol. 39, No. 4, pp. 858, 1992.
58. Ko PK, "Approaches to Scaling," in *Advanced MOS Device Physics*, N. Einspruch and G. Gildenblat, Eds., New York, Academic, pp. 25-30, 1989.
59. Wong H and Poon MC, "Approximation of the Length of Velocity Saturation Region in MOSFET," *IEEE Trans. Electron Dev.*, Vol. 44, No. 11, pp. 2033-2036, 1997.
60. El Mansy YA and Boothroyd AR, "A Simple Two-Dimensional Model for IGFET Operation in the Saturation Region," *IEEE Trans. Electron Dev.*, Vol. ED-24, No. 3, pp. 254-262, 1977.
61. Olympus, "CX21 Upright Imaging Microscope Brochure," 2011.
62. Tessier G, Hole S, and Fournier D, "Quantitative Thermal Imaging by Synchronous Thermoreflectance with Optimized Illumination Wavelengths," *Appl. Phys. Lett.*, Vol. 78, No. 16, pp. 2267-2269, 2001.
63. Christofferson J, Vashaee D, Shakouri A, Melese P, Xiaofeng F, Gehong Z, Labounty C, Bower JE, and Croke ET III, "Thermoreflectance Imaging of Superlattice Micro Refrigerators," *17th IEEE Semicon. Therm. Meas. & Manage. Symp.*, pp. 58-62, 2001.
64. Tessier G, Bardoux M, Boue C, Filloy C, and Fournier D, "Back Side Thermal Imaging of Integrated Circuits at High Spatial Resolution," *Appl. Phys. Lett.*, Vol. 90, No. 171112, 2007.
65. Paniccia M, Rao RM, and Yee WM, "Optical Probing of Flip-Chip Packaged Microprocessor," *J. Vac. Sci. Technol. B.*, Vol. 16, No. 6, pp. 3625-3630, 1998.
66. Pawley JB, *Handbook of Biological Confocal Microscopy 3rd ed.*, Springer, pp. 4-5, 2006.
67. Minsky M, "Microscopy Apparatus," Patent No. US 3,013,467, 1961.
68. Kino GS, "Fundamentals of Scanning Systems," in *Scanned Image Microscopy*, E. Ash, Ed., New York, Academic Press, pp. 1-22, 1980.
69. Wilsher K, Lo W, Eiles TM, and Xiao G, "Integrated Circuit Waveform Probing Using Optical Phase Shift Detection," *Proc. Intl. Symp. Testing & FA (ISTFA 2000)*, pp. 479-485, 2000.
70. Claeys W, Dilhaire S, Quintard V, Dom JP, and Danto Y, "Thermoreflectance optical test probe for the measurement of current-induced temperature changes in microelectronic components," *Qual. & Reliab. Eng. Intl.*, Vol. 9, pp. 303-308, 1993.
71. Quintard V, Deboy G, Dilhaire S, Lewis D, Phan T, and Claeys W, "Laser Beam Thermography of Circuits in the Particular Case of Passivated Semiconductors," *Microelec. Eng.*, Vol. 31, pp. 291-298, 1996.
72. Dilhaire S, Grauby S, and Claeys W, "Calibration Procedure for Temperature Measurements by Thermoreflectance Under High Magnification Conditions," *Appl. Phys. Lett.*, Vol. 84, No. 5, pp. 822-824, 2004.

73. Opsal J, Rosencwaig A, and Willenborg DL, "Thermal-wave detection and thin-film thickness measurements with laser beam deflection," *Appl. Optics,* Vol. 22, No. 20, pp. 3169-3176, 1983.
74. Olmstead MA and Amer NM, "A new probe of the optical properties of surfaces," *J. Vac. Sci. Technol. B.*, Vol. 1, No. 3, pp. 751-755, 1983.
75. Kindereit U, Boit C, Kerst U, Kasapi S, Ispasoiu R, Ng R, and Lo W, "Comparison of laser voltage probing and mapping results in oversized and minimum size devices of 120 nm and 65 nm technology," *Microelectron. Reliab.*, Vol. 48, pp. 1322-1326, 2008.
76. Kindereit U, Woods G, Tian J, Kerst U, Leihkauf R, and Boit C, "Quantitative Investigation of Laser Beam Modulation in Electrically Active Devices as used in Laser Voltage Probing," *IEEE Trans. Dev. Matl. Reliab.*, Vol. 7, No. 1, pp. 19-30, 2007.
77. Koh LS, Marks H, Ross LK, Chua CM, and Phang JCH, "Laser Timing Probe with Frequency Mapping for Locating Signal Maxima," *Proc. Intl. Symp. Testing & FA (ISTFA 2009)*, pp. 33-37, 2009.
78. Heinrich HK, Hemenway BR, McGroddy KA, and Bloom DM, "Measurement of Real-time Digital Signals in a Silicon Biploar Junction Transistor using a Noninvasive Optical Probe," *Electron. Lett.*, Vol. 22, No. 12, pp. 650-652, 1986.
79. Heinrich HK, Pakdaman D, Kent DS, and Cropp LM, "Backside Optical Measurements of Picosecond Internal Gate Delays in a Flip-Chip Packaged Silicon VLSI Circuit," *IEEE Photon. Tech. Lett.*, Vol. 3, No. 7, pp. 673-675, 1991.
80. Kasapi S, Tsao CC, Wilsher K, Lo W, and Somani S, "Laser Beam Backside Probing of CMOS Integrated Circuits," *Microelectron. Reliab.*, Vol. 39, pp. 957-961, 1999.
81. Lo W, Nataraj Nagamani, Boiadjieva N, Vedegarbha P, and Wilsher K, "Polarization Difference Probing: A New Phase Detection Scheme for Laser Voltage Probing," *Proc. Intl. Symp. Testing & FA (ISTFA 2004)*, pp. 9-17, 2004.
82. Shimizu Y, Ishii J, and Baba T, "Reflectance Thermometry for Microscale Metal Thin Films," *Jpn. J. Appl. Phys.*, Vol. 46, No. 5A, pp. 3117-3119, 2007.
83. Goh SH, "Development and Characterization of Refractive Solid Immersion Lens Technology for Far-field Integrated Circuit Failure Analysis using Laser Induced Techniques," PhD Dissertation, National University of Singapore, 2009.
84. Sheppard CJR and Choudhury A, "Image Formation in the Scanning Microscope," *Optica Acta*, Vol. 24, No. 10, pp. 1051-1073, 1977.
85. Mitutoyo Corporation, "Microscope Units, Objectives, Eyepieces and Accessories," Catalog No. E4191-378.
86. Opto Engineering. (2011). *Telecentric lenses: Basic Information and working principles*. Available: http://www.opto-engineering.com/telecentric-lenses-tutorial.html
87. Grauby S, Dilhaire S, Jorez S, and Claeys W, "Temperature Variation Mapping of A Microelectromechanical System by Thermoreflectance Imaging," *IEEE Electron Dev. Lett.*, Vol. 26, No. 2, pp. 78-80, 2005.
88. Rakic AD, "Algorithm for the determination of intrinsic optical constants of metal films: application to aluminium," *Appl. Optics*, Vol. 34, pp. 4755-4767, 1995.

89. Gray PR, Hurst PJ, Lewis SH, and Meyer RG, *Analysis and design of analogy integrated circuits*, 4th ed., Wiley, pp. 132-135, 2001.
90. Teo JKJ, Chua CM, Koh LS, and Phang JCH, "Backside Reflectance Modulation of Microscale Metal Interconnects," *IEEE Intl. Reliab. Phys. Symp. (IRPS 2011),* No. FA-4, 2011.
91. El Nokali M and H Miranda, "A Simple Model for the MOS Transistor in Saturation," *Solid-State Electronics,* Vol. 29, pp. 591-596, 1986.
92. Christofferson J and Shakouri A, "Thermal measurements of active semiconductor micro-structures acquired through the substrate using near IR thermoreflectance," *Microelectron. J.,* Vol. 35, pp. 791-796, 2004.
93. Chua CM, "Personal Communication," 2011.
94. Quah ACT, Phang JCH, Koh LS, Tan SH, and Chua CM, "Enhanced Detection Sensitivity with Pulsed Digital Signal Integration Algorith," *Intl. Symp. Test & FA (ISTFA 2006),* pp. 234-238, 2006.
95. Phan T, Dilhaire S, Quintard V, Claeys W, and Batsale JC, "Thermoreflectance measurements of transient temperature upon integrated circuits: application to thermal conductivity identification," *Microelec. J.,* Vol. 29, No. 4-5, pp. 181-190, 1998.
96. Seliger N, Pogany D, Furbock C, Habas P, Gornik E, and Stoisiek M, "A Laser Beam Method for Evaluation of Thermal Time Constant in Smart Power Devices," *Microlectron. Reliab.,* Vol. 37, No. 10/11, pp. 1727-1730, 1997.
97. Taur Y, "MOSFET Channel Length Extraction and Interpretation," *IEEE Trans. Electron Dev.,* Vol. 47, No. 1, pp. 160, 2000.
98. Falk RA, "Advanced LIVA/TIVA Techniques," *Intl. Symp. Test & FA (ISTFA 2001),* pp. 59-65, 2001.
99. Quah ACT, Chua CM, Tan SH, Koh LS, Phang JCH, Tan TL, and Gan CL, "Laser-induced Detection Sensitivity Enhancement with Laser Pulsing," *Electron. Dev. FA (EDFA 2008),* Vol. 3, pp. 18-26, 2008.